Interactions of High Power Ultrashort Pulses with Nonlinear Optical Materials and Systems

by

Carl Michael Liebig

(Under the direction of William M. Dennis)

Abstract

In this dissertation a combination of experimental and computational techniques are used to investigate the interaction of high intensity ultrashort pulses with nonlinear optical materials and devices. In particular, degenerate four-wave mixing in the forward two-pulse geometry was combined with the numerical solution to the optical Bloch equations to extract an electronic dephasing time in the infrared absorbing organic dye IR140. Additionally, finite-difference time-domain simulations were used to investigate the reflective properties of three dielectric structures, a quarter-wave dielectric stack, a continuously varying rugate and a discretely varying rugate for the case of high intensity ultrashort pulses. Finally a combination of linear and nonlinear spectroscopies were used to investigate the optical properties of green fluorescent protein. *Ab initio* and semi-empirical quantum chemistry techniques were used as an aid to interpreting the experimental data.

Index words: Nonlinear spectroscopy, Ultrafast optics, Organic dyes, Fluorescent proteins, Degenerate four-wave mixing, Z-scan

Interactions of High Power Ultrashort Pulses with Nonlinear Optical Materials and Systems

by

Carl Michael Liebig

B.S., University of Redlands, 1998

M.S., The University of Georgia, 2000

A Dissertation Submitted to the Graduate Faculty

of The University of Georgia in Partial Fulfillment

of the

Requirements for the Degree

Doctor of Philosophy

Athens, Georgia

2006

Interactions of High Power Ultrashort Pulses with Nonlinear Optical Materials and Systems

by

Carl Michael Liebig

Approved:

Major Professor: William M. Dennis

Committee: Michael R. Geller
Uwe Happek

Electronic Version Approved:

Maureen Grasso
Dean of the Graduate School
The University of Georgia
December 2006

Acknowledgments

Firstly, I would like to thank my committee Dr. Uwe Happek and Dr. Mike Geller. Both of whom have effected my physics career greatly in their own way and inspired me to continue on the path of the Ph.D.

I would like to thank Dr. Chris Brewer, Dr. Mark Walker and Dr. Sean Kirkpatrick of the Air Force Research Laboratories for samples, many years of funding for both lab equipment and living expenses. Without their generous contributions, this work would have never been completed.

I would like to express my appreciation for to the faculty and staff of the Department of Physics and Astronomy at the University of Georgia for their help and words of encouragement through this process.

I would like to thank my classmates and fellow group members for their help putting all of this together. In particular, I would like to thank Sebastian Winkler who has spent countless hours discussing physics and other subjects with me. Through these insightful discussions, many of the ideas in the following pages came to light.

I would like to express by gratitude to my family, they have stood with me through thick and thin and offered their support and love through it all. My parents have never doubted my ability to finish and have offered more and more support as time has progressed. I would also like to thank my wonderful wife Leslie who has had to deal with me as I have been writing this work while planning a wedding. I love you all dearly and you are forever in my thoughts.

Most of all I would like to thank my advisor, Dr. Bill Dennis. You have been my guide on this path to the Ph.D. Without your endless support I would not have even had the opportunity to start this journey. You have both encouraged and scolded me when I have

needed it, and I am a better person for it. You have made working a pleasure and every morning I looked forward to going to work. I am still not sure what I will do without you, but with what you have taught me I know that I will figure it out. You are a great friend and I will miss you like none other. Thank you for everything.

Table of Contents

Chapter 1

Introduction

1.1 Introduction to Nonlinear Optics

The development of the laser in 1960 stimulated intensive experimental investigations into nonlinear optical properties[1][2]. Franken *et al.*[3] reported the first observation of harmonic generation by frequency doubling a focused ruby laser pulse. Shortly thereafter, the observation of third-order nonlinear effects was reported by Terhune *et al.*[4]. Nonlinear effects cause changes to the optical properties of the materials that can in turn affect the propagation of an optical pulse. For example, an high intensity pulse with a Gaussian spatial profile propagating through a medium containing a nonlinear index of refraction can create a refractive index gradient which causes the beam to focus[5]. In general, the polarization of a medium is a complicated function of the total electric field $\vec{E}(\omega)$ and can be expressed as a power series in term of the electric field. At low intensities the linear term dominates the power series and $\vec{P}(\omega)$ can be expressed

$$\vec{P}(\omega) = \epsilon_0 \chi^{(1)}(\omega) \cdot \vec{E}(\omega), \tag{1.1}$$

where ϵ_0 is the electric permittivity free space and $\chi^{(1)}$ is the first order electric susceptibility and is a complex second rank tensor[6]. The real part of the susceptibility is related directly to the index of refraction, and the imaginary part of the susceptibility is related to the linear absorption coefficient.

Modern ultrashort laser systems are capable of producing intensities on the order of $100\,\mathrm{TW/cm^2}$, which is a regime where nonlinear effects occur in almost every material; in

this case the polarization becomes[7]

$$\vec{P} = \epsilon_0 \left(\chi^{(1)} \cdot \vec{E} + \chi^{(2)} : \vec{E}\vec{E} + \chi^{(3)} \vdots \vec{E}\vec{E}\vec{E} + \cdots \right), \tag{1.2}$$

where $\chi^{(1)}$, $\chi^{(2)}$, and $\chi^{(3)}$ are the linear, second-order and third-order susceptibility respectively. Each of the individual terms in the polarization describes different linear and nonlinear optical properties of the medium. The second order susceptibility governs effects such as sum or difference frequency generation. Sum frequency generation is now used as a standard technique for doubling the frequency of laser pulses.

In materials with inversion symmetry, the second order term vanishes and the polarization can be expressed to leading nonlinear order as

$$\begin{aligned} \vec{P} &= \epsilon_0 (\chi^{(1)} + \chi^{(3)} E^2 + \cdots) \vec{E} \\ &= \epsilon_0 \chi_{\text{eff}}(I) \vec{E}. \end{aligned} \tag{1.3}$$

This expression of the polarization has the same form as the linear case except for an intensity dependent susceptibility. As in the linear case, the real part of the third-order susceptibility is related to an intensity dependent index of refraction which can be expressed as

$$n(I) = n_0 + n_2 I, \tag{1.4}$$

where n_0 is the linear index of refraction and n_2 is the nonlinear index of refraction. The imaginary part is related to the intensity dependent absorption coefficient and can be expressed by

$$\alpha(I) = \alpha_0 + \beta I, \tag{1.5}$$

where α_0 is the linear absorption coefficient and β is the nonlinear absorption coefficient. The nonlinear index of refraction has found applications that range from optical switching to Kerr lens mode-locking, a technique which is routinely used to passively mode-lock commercial Ti:Sapphire laser systems[5].

Nonlinear spectroscopic techniques can be used as probes to investigate many material properties. In addition to measuring the nonlinear properties such as n_2 and β (Z-scan),

techniques such as four-wave mixing can be used to investigate dynamical properties such as excited state lifetimes and electronic dephasing time which provide useful information on the both optical center and its interaction with the environment.

The interaction of high intensity ultrashort optical pulses with materials possessing high optical nonlinearities can also lead to unwanted effects. For example self-focusing can lead to plasma generation and ultimately to optical damage. Since many optical systems are designed using the laws of linear optics, they may not behave as expected for high intensity pulses. For example, dielectric mirrors are routinely used to reflect high intensity ultrashort pulses which are often constructed of materials that possess large third-order susceptibilities. The optical intensities in the dielectric layers may come close to the damage threshold of the material, thus causing unintended perturbations to the phase of the reflected light through the nonlinear refractive index. The changes to the phase of the light will have an effect on the constructive interference, which is required for the reflective nature of the mirror[8].

Of growing importance in the field of nonlinear optics is the use of computer simulations to model nonlinear effects. Several methods have been used to simulate high intensity light interactions with matter; an early approach was the adaption by Macleod *et al.*[9] of the characteristic matrix method. The nonlinear characteristic matrix was used to investigate optical bistability in Fabry-Perot etalons at high optical intensities. Characteristic matrix calculations are formulated assuming continuous working sources, and fail to predict the effects of ultrashort pulses on optical structures. A methods which accounts for the effects of ultrashort pulses is the numerical solution of the nonlinear Schrödinger equation; an equation of motion for the pulse envelope function in the presence of a third-order nonlinearity. Since the nonlinear Schrödinger describes the evolution of the pulse envelope, investigations of the interaction of the pulse with optical structures that have spatial variations on the order of the optical wavelength requires a different methods. An alternative approach, finite-difference time-domain (FDTD) method, uses the numerical integration of Maxwell's curl equations to obtain both the electric and magnetic fields[10] and not only allows calculation of the

changes to the optical properties of dielectric structures, but accounts for the perturbations to the optical pulse caused by its interaction with the structure. This dissertation uses a combination of experimental and simulational techniques as tools for investigating the interaction of high intensity optical pulses with materials and structures. The outline of this dissertation is given in the next section.

1.2 Dissertation Outline

In chapter 2, the nonlinear spectroscopic technique, degenerate four-wave mixing (DFWM), was used to measure the electronic dephasing time of the $S_0 \leftrightarrow S_1$ transition in the organic mode-locking dye IR140. The dephasing time was extracted from the experimental DFWM signals, by fitting the solution of the optical Bloch equation to the experimental data.

In chapter 3, the use of the FDTD method to simulate the linear and nonlinear optical properties of dielectric filters is described. The reflective properties of these structures were calculated from the simulations and the results at low intensity were compared to characteristic matrix calculations. The FDTD method allows the optical fields to be simulated inside of the dielectric structures permitting location of the structures responsible for the nonlinear effects to be located. These simulations and their results will be discussed in detail in chapter 3.

In chapter 4, a combination of linear and nonlinear spectroscopic techniques will be used to probe the properties of the green fluorescent protein (GFP). Linear techniques were used to determine the excited state lifetime and to investigate the effect of hydrostatic pressure on the emission spectrum of GFP. The nonlinear optical technique, Z-scan, was then used to directly measure the two-photon absorption cross-section of GFP. Finally an attempt was made to use degenerate four-wave mixing to investigate dephasing in GFP.

The conclusions reached in this study are summarized in chapter 5.

1.3 References

[1] A. L. Schawlow, C. H. Towns, "Infrared and optical masers," Phys. Rev. **112**, 1940-1949 (1958).

[2] T. H. Maiman, "Stimulated optical radiation in ruby," Nature **187**, (493-494) (1960).

[3] P. A. Franken, A. E. Hill, C. W. Peters, G. Weinreich, "Generation of Optical Harmonics," Phys Rev. Lett. **7**, 118-120 (1961).

[4] R. W. Terhune, P. D Maker, C. M. Savage, "Optical harmonic generation in calcite," Phys Rev. Lett. **8**, 404-406 (1962).

[5] C. Hirlimann, "Pulsed optics," in *Femtosecond Laser Pulses Principles and Experiments*, 2nd Ed., edited by C. Rullière, (Springer-Verlag, Berlin, 2005).

[6] J. D. Jackson, *Classical Electrodynamics*, John Wiley and Sons, 3rd ed. (1999).

[7] See for example: R. W. Boyd, *Nonlinear Optics*, Academic Press Amsterdam, 2nd ed. (2003).

[8] H. A. Macleod, *Thin-Film Optical Filters*, Institute of Physics Publishing, 3rd ed. (2001).

[9] B. G. Bovard, H. A. Macleod, "Nonlinear behavior of optical coatings subjected to intense laser irradiation," J. Mod. Opt. **35**, 1151-1168 (1988).

[10] A. Taflove, S. C. Hagness *Computational Electrodynamics the Finite-Difference Time-Domain Method*, Artech House London, 3rd ed. (2006).

Chapter 2

Dephasing Measurements in IR140

2.1 Introduction

To gain a greater understanding of the dynamical processes that occur in systems of several thousand atoms such as proteins or other biological molecular systems, it is often necessary to measure the properties of systems that contain significantly fewer atoms. Organic dye molecules possess many of the same optical properties as their more complicated biological counterparts but are generally easier to obtain, handle and analyze. Once the linear and nonlinear properties of simpler systems have been characterized, it is hoped that the knowledge gained can be applied to understanding more complicated molecular systems.

Organic dyes have attracted considerable attention as efficient tunable laser materials. They have also been used as saturable absorbers for mode-locking in both pulsed and continuous wave laser sources and hence have been essential to the development of ultrashort laser systems. Due to their high third-order optical nonlinearities they have been exploited for optical switching[1], optical logic[2], and bottleneck optical limiting[3]. Over the last decade combinations of linear and nonlinear optical techniques have been applied to determine the amplitude of the third-order susceptibility for various organic dyes[4]; these measurements have led to a greater insight of the dynamical processes that occur within the organic dye and have stimulated the development of new optical chromophores[5].

IR140 is a saturable absorbing organic dye has been used to passively mode-lock Ti:Sapphire laser systems, and has recently attracted attention as a possible near-infared organic laser source[6][7]. Fig. 2.1 shows the structure of IR140 which is a meso-diphenylamine

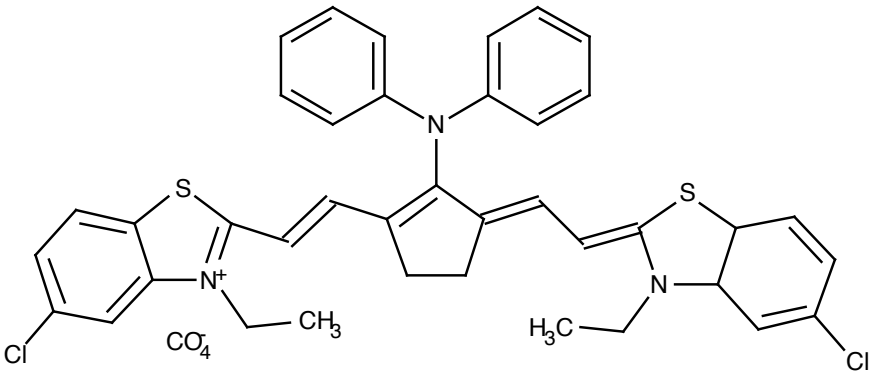

Figure 2.1: The molecular structure of the meso-diphenylamine substituted heptamethine dye IR140 as reported in reference [9].

substituted heptamethine dye[8]. IR140 is soluble in many common solvents and will survive for several days before denaturation. The spectral properties of IR140 have been well studied and the excited state lifetime has been documented[9]. Measurements have also been carried out to characterize stimulated emission and to determine the strength of the third-order susceptibility of IR140[10]. The ease of handling, the information available, and a strong absorption peak at 800 nm makes IR140 ideal for the degenerate four-wave mixing measurements using the ultrashort optical pulses generated by a Ti:Sapphire laser.

Degenerate four-wave mixing (DFWM) experiments have been used for a number of years to measure a variety of material characteristics that include the third-order nonlinear optical susceptibility, $\chi^{(3)}$, the excited state lifetime T_1, and the electronic dephasing time, T_2, in a wide range of optical systems ranging from semi-conductors to organic molecules. In the forward geometry, DFWM can be implemented in a three-pulse configuration to extract

information about both T_1 and T_2, or if the value of T_1 is already known, DFWM can be implemented in the simpler two-pulse geometry to yield information about T_2[11]. In this chapter, DFWM experiments in the forward two-pulse geometry were performed on IR140. The resulting DFWM signals were fitted using the solution to the optical Bloch equation and a value of the dephasing time was extracted. The resulting T_2 is compared to experimentally measured values of the dephasing time for other organic dye/solvent combinations.

2.2 Experimental

Degenerate four-wave mixing in the two-pulse forward geometry was performed using the output of a Spectra-Physics Tsunami, mode-locked Ti:Sapphire laser. The laser emission was a pulse train of near Fourier transform limited 70 fs pulse as determined by autocorrelation assuming a hyperbolic secant squared envelope. Fig. 2.2(a) shows a typical autocorrelation signal measured from the Ti:Sapphire laser system used in this study. The spectral bandwidth was determined to be 13 nm centered at 788 nm. Fig. 2.2(b) shows a typical spectral bandwidth of the laser system used in this measurement. The single pulse energy was determined to be 8.5 nJ. When focused to a 100 μm beam waist the peak intensity was 3.8 GW/cm^2.

Fig. 2.3 shows a schematic of the experimental setup. Each pulse from the laser system was split by division of amplitude into two equal intensity pulses using a 50/50 beam splitter. Each pulse was propagated along two independent, adjustable length beam paths. The beam paths were adjusted using retro-reflectors mounted Newport UMT100PP.1 translation stages controlled using an Newport MM3000 motion controller. The translation stages have a step resolution of 100 nm. The two beams were focused into the sample (with directions $\vec{k}_1$ and $\vec{k}_2$) using a single 70 mm focal length lens. At high repetition rates photobleaching and thermal damage due to multiple pulses interacting with the sample have an effect on the strength of the DFWM signal. To eliminate these effects and those caused by scattering from multiple interfaces, the sample, a 1.71×10^{-4} M solution of IR140 in a 3:1 mixture of ethylene glycol and dimethylsulfoxide (DMSO), was contained in a high speed dye jet. The

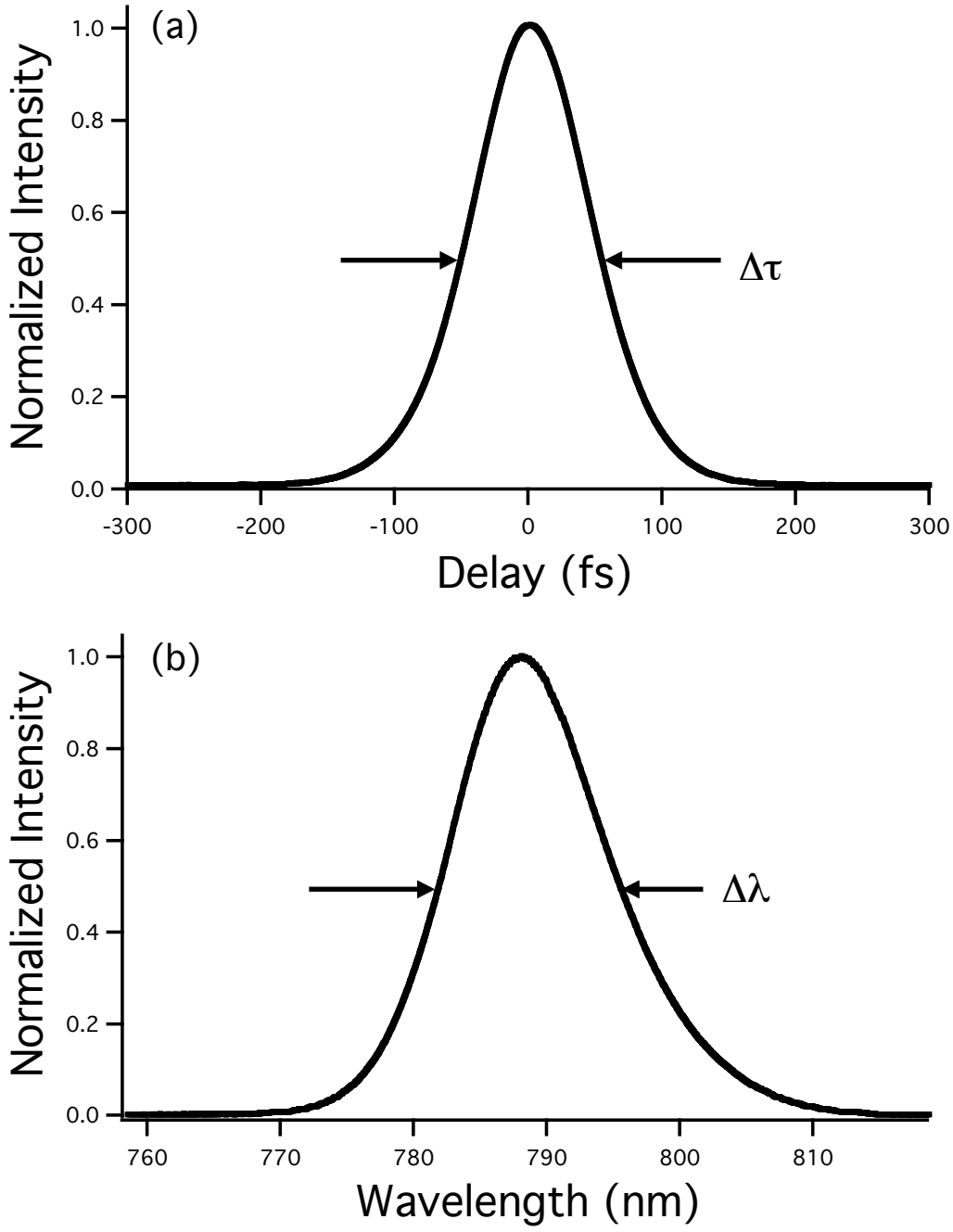

Figure 2.2: (a) A typical autocorrelation measurement from Ti:Sapphire laser system used in this study. (b) A typical spectral measurement of the near (Fourier) transform limited pulse produced by the Ti:Sapphire laser system used in this study.

dye jet was from a Spectra-Physics Model 375B dye laser system and was secured using a home-made mount. To keep the dye at a constant temperature, the dye circulator (Spectra-Physics model 376B dye circulator) was modified so that its heat exchanger was cooled by a refrigeration system (HAAKE A80 heater/refrigerator). Fig. 2.4(a) shows a close up schematic of the DFWM experiment. The DFWM signal pulse trains in both the $2\vec{k}_1 - \vec{k}_2$ and the $2\vec{k}_2 - \vec{k}_1$ directions were detected using a photomulitplier tube (Oriel 77341). A phase sensitive detector (Stanford Research Systems, Model SR830 PSP, Lock-in Amplifier) was used to amplify and measure the DFWM signals. A computer system was used to both control the optical delay and for data acquisition.

In DFWM measurements the polarization of both the excitation pulses and the DFWM signals can be used as a tool to verify the authenticity of the DFWM signals. Selecting the polarization of the DFWM signal eliminates the effect of thermal changes to the sample, such as thermal gratings cause by absorption of the interference patterns formed by the excitation pulses. The third-order susceptibility, a fourth-rank tensor, can have up to 81 nonzero terms. Since the IR140/solvent system is an isotropic medium, the symmetries of the system allow only 21 nonzero terms. Furthermore, of the remaining nonzero terms only three of them are independent.

$$\begin{gathered}
\chi^{(3)}_{1111} = \chi^{(3)}_{2222} = \chi^{(3)}_{3333} \\
\chi^{(3)}_{1122} = \chi^{(3)}_{2211} = \chi^{(3)}_{2233} = \chi^{(3)}_{3322} = \chi^{(3)}_{3311} = \chi^{(3)}_{1133} \\
\chi^{(3)}_{1122} = \chi^{(3)}_{2211} = \chi^{(3)}_{2323} = \chi^{(3)}_{3232} = \chi^{(3)}_{3131} = \chi^{(3)}_{1313} \\
\chi^{(3)}_{1221} = \chi^{(3)}_{2112} = \chi^{(3)}_{2332} = \chi^{(3)}_{3223} = \chi^{(3)}_{3113} = \chi^{(3)}_{1331} \\
\chi^{(3)}_{1111} = \chi^{(3)}_{1122} + \chi^{(3)}_{1212} + \chi^{(3)}_{1221}
\end{gathered} \tag{2.1}$$

Where 1 corresponds to the x direction, 2 the y direction and 3 the z direction. It can also be noted that under the experimental conditions the signal propagating in the $2\vec{k}_1 - \vec{k}_2$ direction is generated by the $\chi^{(3)}_{1221}$ component, which has one third of the magnitude of the $\chi^{(3)}_{1111}$ component[12]. To further simplify our experiment and analysis, the polarization of the

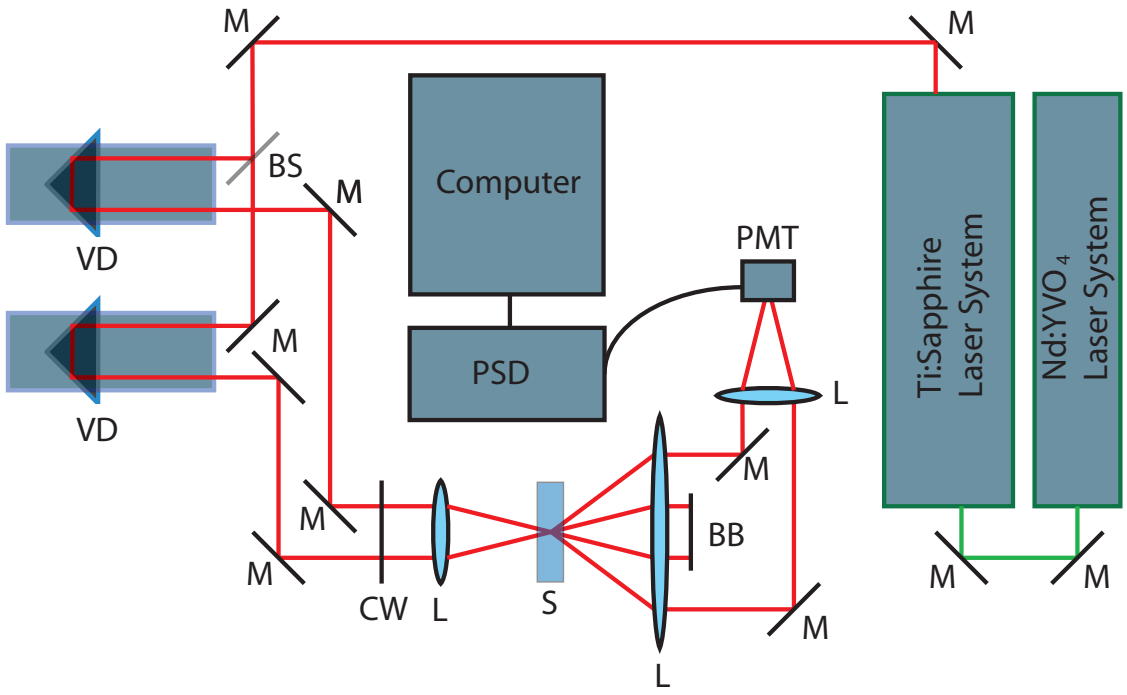

Figure 2.3: A schematic showing the experimental setup for the forward degenerate four-wave mixing experiment in the two pulse geometry. In this schematic M corresponds to mirrors, BS a 50/50 beamsplitter, VD variable beam delays, CW optical chopper wheel, L to lenses, S sample, BB a beam block, PMT a photomultiplier tube, PSD to a phase sensitive detector (Lock-in amplifier).

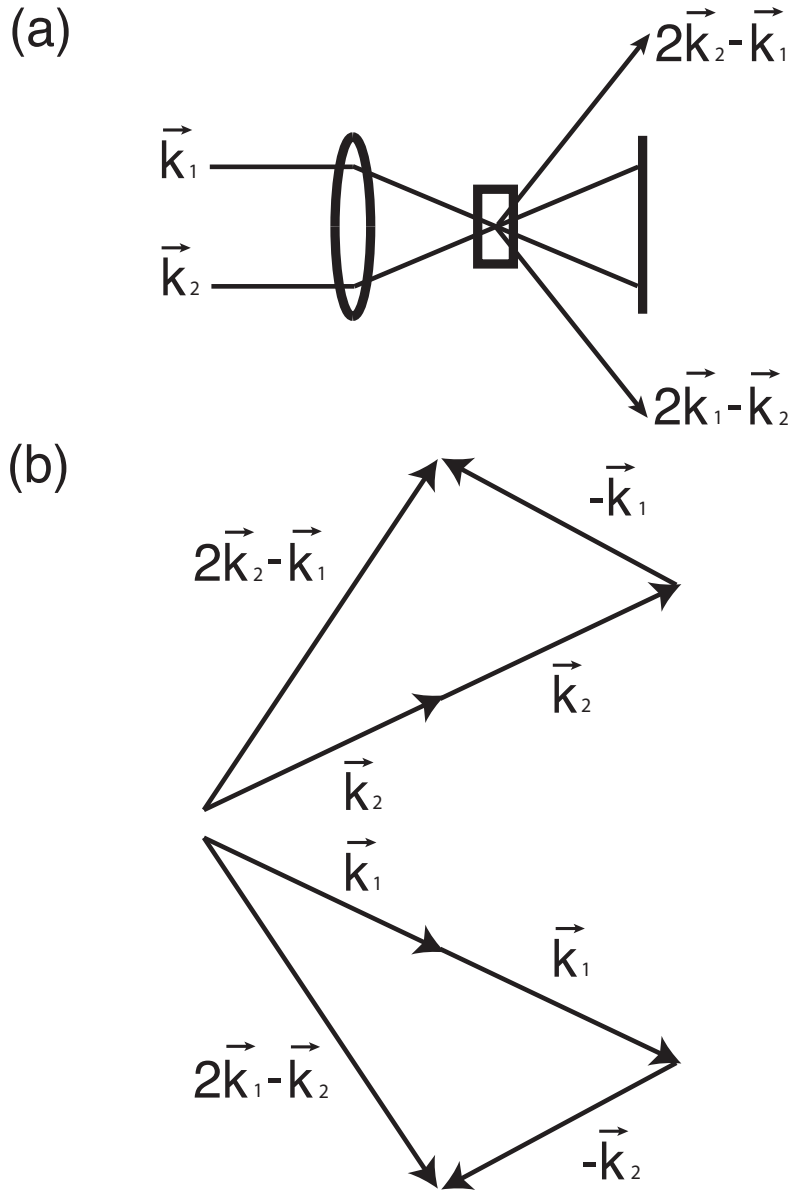

Figure 2.4: (a) A close up view of a standard DFWM experiment. The DFWM signals are detected in the $2\vec{k}_1 - \vec{k}_2$ and $2\vec{k}_2 - \vec{k}_1$ directions. (b) A vector diagram showing the mixing of three wave vectors to form a fourth wave vector in either the $2\vec{k}_1 - \vec{k}_2$ direction or the $2\vec{k}_2 - \vec{k}_1$ direction.

excitation pulses in DFWM are limited to the z-plane; therefore the only components which contribute to the DFWM signals are $\chi^{(3)}_{1111}, \chi^{(3)}_{1122}, \chi^{(3)}_{1212}$, and $\chi^{(3)}_{1221}$, which must satisfy the relation $\chi^{(3)}_{1111} = \chi^{(3)}_{1122} + \chi^{(3)}_{1212} + \chi^{(3)}_{1221}$. To select the intended polarization of the DFWM signal, first the polarization of the $\vec{k}_1$ pulse was rotated from vertical to horizontal polarization using an achromatic half-wave plate. The polarization of the pulses was confirmed using Glan-Taylor polarizers.

Measuring the intensity of both the $2\vec{k}_1 - \vec{k}_2$ and the $2\vec{k}_2 - \vec{k}_1$ signal pulses as a function of the delay time between the two excitation pulses reveals two peaks that are shifted with respect to zero delay. To check the contribution of the neat solvent to the four-wave mixing signal, a background measurement was performed. No measurable signal was observed from the neat solvent. Using the excited state lifetime ($T_1 = 1.20 \pm 0.02\,\text{ns}$) reported by Imhof *et al.*[13], the methods detailed below were used to simulate a DFWM signal that could be fitted to the experimental data. A value of $T_2 = 50 \pm 5\,\text{fs}$ was extracted.

2.3 Model

The analysis of the degenerate four-wave signals using a two-beam geometry follows the formalism used by Brito Cruz *et al.*[14] and Mukamel[15]. The relevant electronic two-level system can be described by the reduced density operator, ρ, the solution of the optical Bloch equation which includes a phenomenological relaxation term that accounts for the coupling to a thermal bath[16]. In the Bloch equation,

$$i\hbar \frac{d\rho}{dt} = [H_0, \rho] + [W(t), \rho] + i\hbar \left.\frac{\partial \rho}{\partial t}\right|_{\text{relax}}, \tag{2.2}$$

H_0 is the reduced unperturbed Hamiltonian, with eigenstates given by

$$H_0|n\rangle = E_n|n\rangle, \tag{2.3}$$

where the E_n ($n = 1, 2$) are the eigenstate energies of the electronic two level system. The second term in equation 2.2 describes the dipolar interaction with the total electric field, with $W(t) = \mu E(t)$, μ is the electric dipole operator with components $\mu_{11} = \mu_{22} = 0$ and

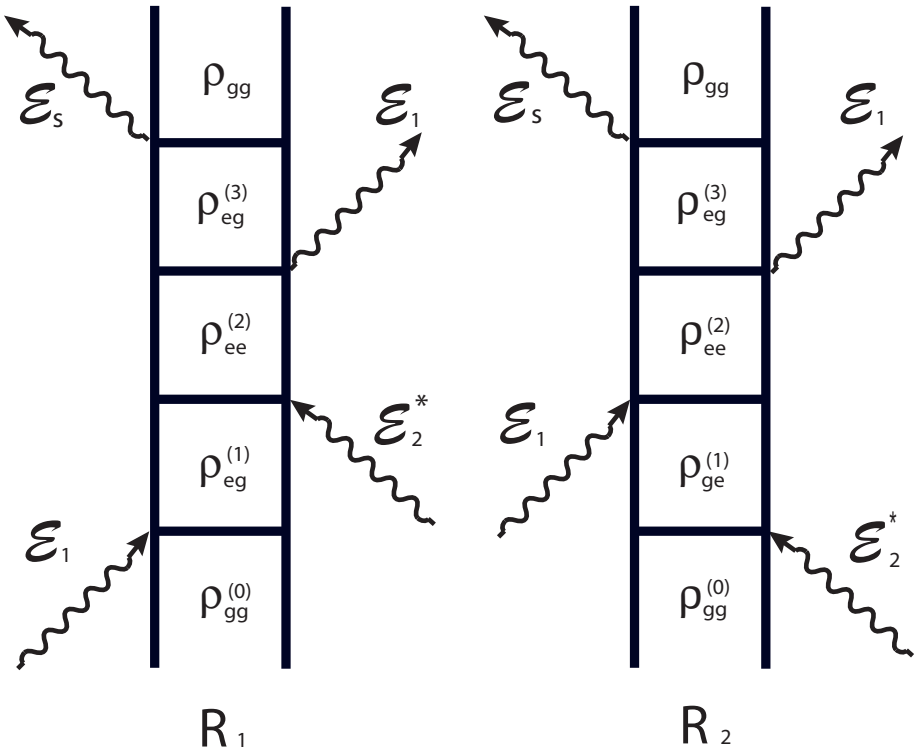

Figure 2.5: Double-sided Feynman diagrams that represent the terms in the third-order of the density operator that contribute to the DFWM signal measured in the two-beam forward geometry[16].

$\mu_{12} = \mu_{21} = 1\ \mathrm{C}\cdot\mathrm{m}$. The third term describes the coupling of the electronic system with a thermal bath; it empirically accounts for the bath degrees of freedom and is of the form

$$\left.\frac{\partial \rho_{nm}}{\partial t}\right|_{\text{relax}} = -\Gamma_{nm}\left(\rho_{nm} - \rho_{nm}^{(0)}\right). \tag{2.4}$$

Γ_{nm} is equal to the electronic population relaxation rate $(1/T_1)$ when $n = m$ and the dephasing rate $(1/T_2)$ when $n \neq m$. $\rho_{nm}^{(0)}$ is the density operator at thermal equilibrium. It is assumed that kT is sufficiently small in comparison to the electronic transition energy so that the only non-zero component of the density operator at thermal equilibrium is $\rho_{11}^{(0)}$. An approximate solution to equation 2.4 is obtained using perturbation theory to third-order in the electric field. Applying the rotating wave approximation and only keeping terms that describe wave propagation in the directions $2\vec{k}_1 - \vec{k}_2$ and $2\vec{k}_2 - \vec{k}_1$. The density operator for the DFWM signals reduces to four terms which are labeled R_i, $i = 1, 2, 3, 4$. Due to the inherent symmetry of the two-pulse DFWM geometry, R_3 is equivalent to R_2 and R_4 is equivalent to R_1 leaving only two terms contributing to the density operator. These are represented by the double-sided Feynman diagrams shown in Fig. 2.5. The first Feynman diagram (R_1) only contributes to the ρ_{nm} when the excitation pulses are temporally overlapped. The overall contribution of R_1 to the two-pulse DFWM signal was calculated to be less than one percent and was neglected in the remaining simulations. The second term (R_2) is thus responsible for the photon echo, and the third-order correction to density operator then reduces to

$$\rho_{eg}^{(3)} = -\frac{|\mu_{eg}|^2 \mu_{eg}}{4} G_{eg}(t) \otimes \Big[\mathcal{E}_3(t)\Big\{G_{ee}(t) \otimes \Big(\mathcal{E}_2(t)\left[G_{eg}^{*}(t) \otimes \mathcal{E}_1^{*}(t)\right]\Big)\Big\}\Big]. \tag{2.5}$$

The complex electric field, $\mathcal{E}(t)$, in equation 2.5 describes the laser pulses, and has the form $\mathrm{sech}(\mathrm{t}/\tau_{\mathrm{p}})$, where τ_p is the excitation pulsewidth. The response of the material is described by the zeroth-order Green function, $G_{nm}(t)$, which is the solution of the Bloch equation with an instantaneous excitation. The Green function is given by

$$G_{nm}(t) = \frac{i}{\hbar}\Theta(t)\exp(-i\omega_{nm} - \Gamma_{nm}t), \tag{2.6}$$

where $\omega_{nm} = \omega_n - \omega_m$ and $\Theta(t)$ is the Heaviside step function. Using the results of equation 2.5, the polarization can be calculated using

$$P(t) = N\langle\mu\rangle = N \ \mathrm{Tr}\,\mu\rho(t) = N\sum_{nm}\mu_{mn}\rho_{nm}, \tag{2.7}$$

where N is the number of particles per unit volume. Inhomogeneous broadening was accounted for by calculating the contribution to the nonlinear polarization of a weighted series of 500 individual simulations detuned from resonance. Observation of the resulting polarization yielded a photon echo at the expected delay time. Finally the resulting inhomogeneously broadened polarization was used to simulate the DFWM signal, $|\mathrm{Re}(P)|^2$, as a function of delay between the $\vec{k}_1$ and $\vec{k}_2$ laser pulses.

2.4 Results and Discussion

By simulating the DFWM signal it could be seen that in general both T_1 and T_2 have an effect on the two-pulse DFWM signals. When T_1 is the same order of magnitude as the excitation pulse width, increasing T_1 causes the peak of the DFWM signal to shift to longer delays. Fig. 2.6 shows the effects that changing T_1 has on the DFWM signals. It can be seen that once T_1 is significantly longer than the excitation pulse width, changes in T_1 produce no noticeable effect on DFWM signal which enables T_1 to be set to a value of 1 ps. For 70 fs laser pulses at 800 nm, DFWM signals have been calculated with T_2 values of 10, 50 and 800 fs. Fig. 2.7 shows the resulting DFWM signals. It is apparent that small changes in T_2 have a significant effect on the DFWM signal, shifting both the peak intensity with respect to zero delay and increasing the decay time of the DFWM signal tail. For large values of T_1, fitting the data to extract a value of T_2 provides a sensitive probe of the dephasing time that is significantly more robust than reading off a value from the peak shift when T_2 is of the order of the pulse width.

Fig. 2.8 shows the experimental DFWM signal intensities, in both the $2\vec{k}_1 - \vec{k}_2$ and the $2\vec{k}_2 - \vec{k}_1$ directions as a function of the delay time between the $\vec{k}_1$ and $\vec{k}_2$ pulses. It is necessary

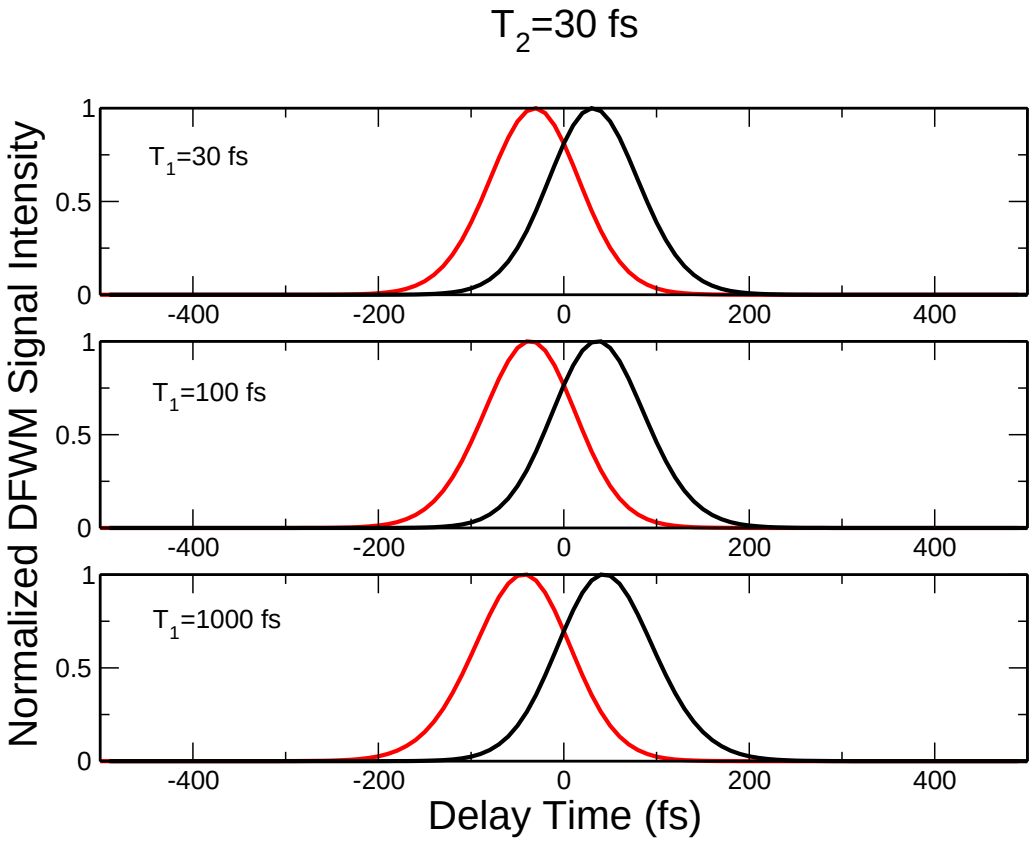

Figure 2.6: Simulated DFWM signals in both the $2\vec{k}_1 - \vec{k}_2$ (black line) and the $2\vec{k}_2 - \vec{k}_1$ (red line) directions for T_1 values of 30, 100, and 1000 fs.

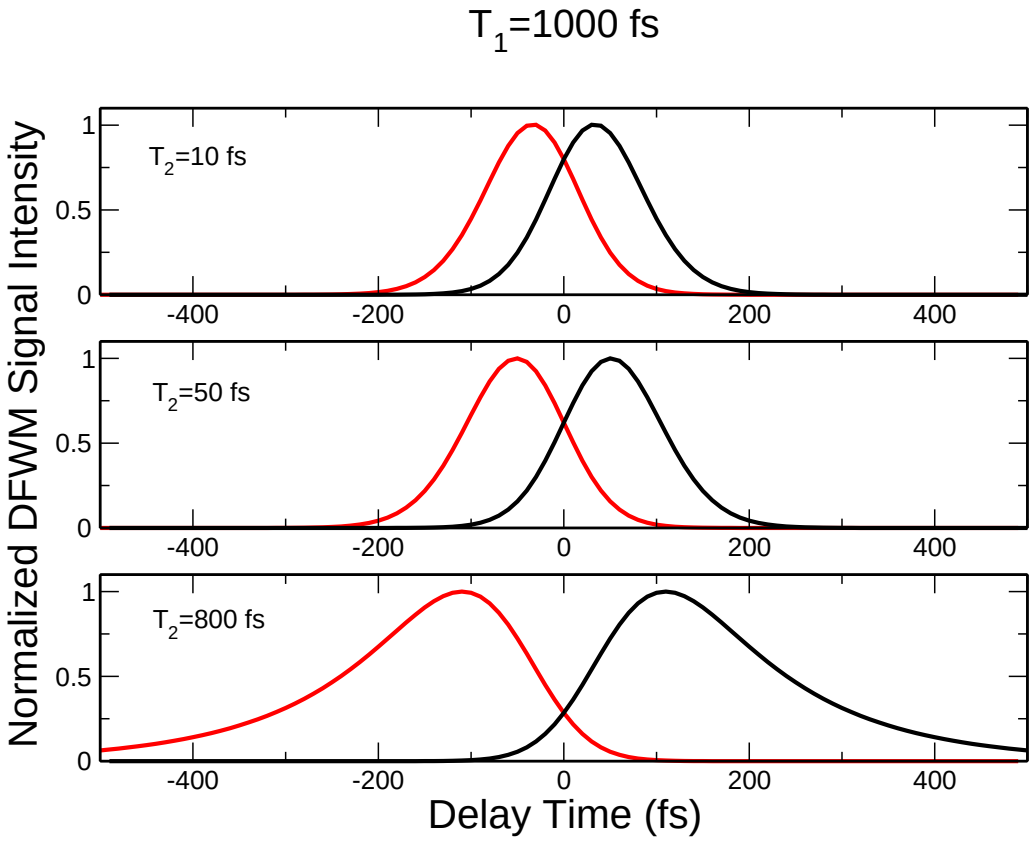

Figure 2.7: Simulated DFWM signals in both the $2\vec{k}_1 - \vec{k}_2$ (solid line) and the $2\vec{k}_2 - \vec{k}_1$ (dashed line) directions for T_2 values of 10, 50, and 800 fs.

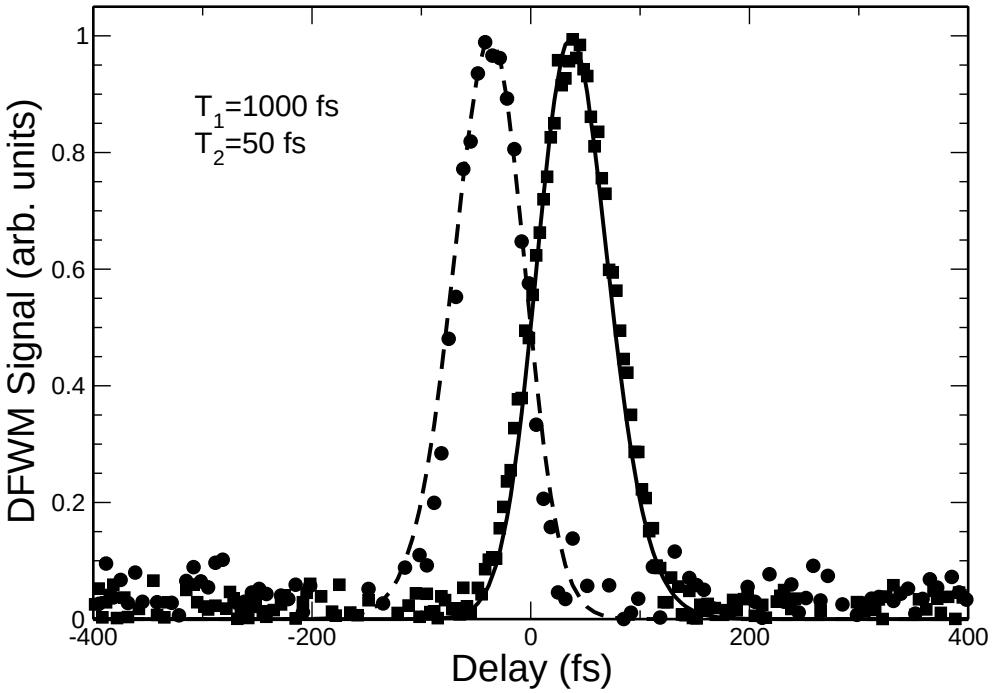

Figure 2.8: DFWM signals in both the $2\vec{k}_1 - \vec{k}_2$ and the $2\vec{k}_2 - \vec{k}_1$ directions obtained both experimentally and by solving the optical Bloch equations. A value of 50 ± 5 fs was extracted for the dephasing time.

to measure the signal in both the $2\vec{k}_1 - \vec{k}_2$ and the $2\vec{k}_2 - \vec{k}_1$ directions to determine the zero delay time. The dephasing time was extracted by a simultaneous χ^2 fit of the full functional form of both the $2\vec{k}_1 - \vec{k}_2$ and the $2\vec{k}_2 - \vec{k}_1$ simulated signals to the respective experimental data. The resulting reduced χ^2 was on the order of unity and yielded a value of 50 ± 5 fs for T_2. Fig. 2.8 shows the resulting fit to the data.

Table 2.1 compares several organic dyes and measured values of their dephasing times from the literature. It can be seen that the dephasing times of other organic dyes in polar solvents are similar to the value reported in this paper. It is also of interest to note that the

Table 2.1: A comparison of the electronic dephasing times for several organic dyes in both polar and non-polar solvents.

Sample	Solvent	Method	T_2
IR140	Ethylene Glycol, DMSO	DFWM	50 ± 5 fs (this work)
DODCI	Ethylene Glycol	DFWM	50±10 fs [21]
HITCI	Ethylene Glycol	Forced Light Scattering	30 fs [24]
Malachite Green	Ethylene Glycol	Photon Echo	60 fs [22]
Nile Blue	Ethylene Glycol	Photon Echo	65 fs [22]
Photoactive Yellow Protein	Phosphate Buffer	Hole Burning	15 fs [23]

dephasing time of photoactive yellow protein in considerably shorter than those measured in the organic dye molecules. Many factors have been cited as contributing to the rapid relaxation times that are observed in organic dyes. It has been reported that solvation dynamics can play an important role in the dephasing of organic dyes[17]. In particular an investigation of the solvation dynamics of IR140 using transient grating experiments has been reported by Vauthey *et al.*[18], who found that the time-scale of the solvation dynamics was on the order of 1–10 ps depending on the viscosity of the solution. Clearly solvation dynamics alone is insufficient to explain the observed dephasing time of 50 ± 5 fs in IR140 indicating that intramolecular processes dominate the phase relaxation in this molecule.

2.5 Conclusions

In this chapter degenerate four-wave mixing in the forward two-pulse geometry was used to measure the DFWM signals from a jet of the saturable absorber IR140 in a solution of

ethylene glycol and dimethylsulfoxide using 70 fs near transform limited pulses. Following the semiclassical formalism described both by Brito Cruz and Mukamel, the nonlinear polarization was calculated and used to simulate DFWM signals including the effects of inhomogeneous broadening. The full functional form of the simulated DFWM signal was fit to the experimental data by using T_2 as a fitting parameter, yielding a dephasing time of 50 ± 5 fs. The dephasing time of IR140 was then compared to other values of T_2 that have been collected using comparable methods[18][25]–[31]. This formalism enables the measurement of the dephasing time of materials that have an excited state lifetime which is considerably longer than the excitation pulsewidth and has the advantage that it can be used to extract dephasing times that are shorter than the excitation pulse width.

2.6 References

[1] P. Tran,"Optical limiting and switching of short pulses by use of a nonlinear photonic bandgap structure with a defect," J. Opt. Soc. Am. B **14**, 2589-2595 (1997).

[2] M. Samoc, P. N. Prasad, "Dynamics of resonant third-order optical nonlinearity in perylene tetracarboxylic dianhydride studied by monitoring first- and second-order diffraction in subpicosecond degenerate four-wave mixing," J. Chem. Phys. **91**, 6643-6649 (1989).

[3] P. A. Miles "Bottleneck optical limiters: the optimal use of excited-state absorbers," Appl. Opt., **33**, 6965-6979 (1994).

[4] Q. Xu, Y. Ma, I. V. Stiopkin, G. R. Fleming, "Wavelength-dependent resonant homodyne and hetrodyne transient grating spectroscopy with a diffractive optics method: Solvent effect of the third-order-signal," J. Chem. Phys **116**, 9333-9340 (2002).

[5] G. S. He, L. Yuan, J. D. Bhawalkar, P. N. Prasad, L. L. Brott, S. J. Clarson, B. A. Reindardt, "Nonlinear Optical Properties of a new chromophore," J. Opt. Soc. Am. B **14**, 1079-1087 (1997).

[6] C. Pan, N. Pu and J. Shieh, "Dynamic pulse buildup in continuous-wave passively mode-locked picosecond Ti:sapphire/DDI and Ti:sapphire/IR140 lasers," Chin. J. Phys. **37**, 361-379 (1999).

[7] J. Thompson, M. Anni, S. Lattante, D. Pisigano, R. I. R. Blyth, G. Gigli, R. Cingolani,"Amplified spontaneous emission from dye-doped polymer thin film," Synthetic Metals **143**, 305-307 (2004).

[8] R. Gray, D. Walton, J. Bickerton, P. Richards, J. Hepenstall, "Hydrolytic breakdown of meso-diphenylanime dye IR140, and isomerism of merocyanine breakdown product," Dyes and Pigments **38**, 97-105 (1998).

[9] U. Brachmann, *Lambdachrome Laser Dyes*, (Lambda Physik GmbH, Göttingen, 1986).

[10] Z. Dai, X. Yue, B. Peng, Q. Yang, X. Liu, P. Ye, "Third order optical nonlinearities of near infrared dyes," Chem. Phys. Lett **317**, 9-12 (2000).

[11] L. V. Dao, C. Lincon, M. Lowe, P. Hannaford, "Spectrally Resolved Two-Colour Femtosecond Photon Echos," in *Femtosecond Laser Spectroscopy* edited by Peter Hannaford, (Springer-Verlag, Berlin, 2005).

[12] M. D. Levenson, S. S. Kano, *Introduction to Nonlinear Laser Spectroscopy* (Revised Edition, Academic Press, Inc., London, 1982).

[13] D. J. S. Birch, G. Hungerford, R. E. Imhof, "Near-infrared spark source excitation for fluorescence lifetime measurements," Rev. Sci. Instrum. **62**, 2405-2408 (1991).

[14] C. H. Brito Cruz, J. P. Gordon, P. C. Becker, R. L. Fork, C. V. Shank, "Dynamics of spectral hole burning," IEEE J. Quant. Electron. **24**, 261-266 (1988).

[15] S. Mukamel, *Introduction to Nonlinear Spectroscopy*, (Oxford University Press, London, 1996).

[16] M. Joffre, "Coherent effects in femtosecond spectroscopy: A simple picture using the Bloch equation," in *Femtosecond Laser Pulses Principles and Experiments*, 2nd Ed., edited by C. Rullière, (Springer-Verlag, Berlin 2005).

[17] Q. Xu, G. D. Scholes, M. Yang, G. R. Fleming, "Probing Solvation and reaction coordinates of ultrafast photoinduced electron-transfer reactions using nonlinear spectroscopies: rhodamine 6G in electron-donating solvents," J. Phys. Chem. A, **103** 10348-10358, (1999).

[18] J.C. Gumy, O. Nicolet, E. Vauthey, "Investigation of the solvation dynamics of an organic dye in polar solvents using the femtosecond transient grating technique," J. Phys. Chem. A **103**, 10737-10743 (1999).

[19] M. Samoc, A. Samoc, B. Luther-Davies, Z. Boa, L. Yu, B. Hsieh, U. Scherf, "Femtosecond Z-scan and degenerate four-wave mixing measurements of real and imaginary parts of the third-order nonlinearity of soluble conjugated polymers," J. Opt. Soc. Am. B. **15**, 817-824 (1998).

[20] P. N. Prasad, D. J. Williams, *Introduction to Nonlinear Optical Effects in Molecules and Polymers*, (John Wiley & Son, Inc., New York, 1991).

[21] J. Diels, I. C. McMichael, "Degenerate four-wave mixing of femtosecond pulses in an absorbing dye jet," J. Opt. Soc. Am. B **3**, 535-543 (1986).

[22] P. C. Becker, H. L. Fragnito, J. Y. Bigot, C. H. Brito Cruz, R. L. Fork, C. V. Shank, "Femtosecond photon echos from molecules in solution," Phys. Rev. Lett. **63**, 505-507 (1989).

[23] T. Masciangioli and S. Devanathan and M. A. Cusanovich, G. Tollin, M. A. El-Sayed, "Probing the Primary Event in the Photocycle of Photoactive Yellow," Photochem. Photobiol. **72**, 639-644 (2000).

[24] A. Kummrow, A. Lau, K. Lenz, "Time resolved study of ultrafast dephasing processes in solution," Phys. Rev. A **55**, 2310-2320 (1997).

[25] A. M. Weiner, S. De Silvestri, E. P. Ippen, "Three pulse scattering femtosecond dephasing studies: theory and experiment," J. Opt. Soc. Am. B **2**, 654-661 (1985).

[26] P. Cong, J. D. Simon, Y. Yan, "Probing the molecular dynamics of liquids and solutions," in *Ultrafast Processes in Chemistry and Photobiology*, Edited by M. A. El-Sayed, I. Tanaka, Y. Molin, (Blackwell Science Ltd, Oxford, 1995).

[27] T. Kobayashi, A. Terasaki, T. Hattori, K. Kurokawa, "The application of incoherent light for the study of femtosecond-picosecond relaxation in condensed phase," Appl. Phys. B. **47**, 107-125 (1988).

[28] K. Misawa, T. Hattori, T. Kobayashi, "Measurement of dephasing time using incoherent light in the Kerr shutter configuration," Opt. Lett. **14**, 453-455 (1989).

[29] T. Hattori, A. Terasaki, T. Kobayashi, "Coherent Stokes Raman scattering with incoherent light for vibrational-dephasing-time measurement," Phys. Rev. A. **35**, 715-724 (1987).

[30] W. P. de Boeij, M. S. Pshenichnikov, D. A. Wiersma, "Ultrafast solvation dynamics explored by femtosecond photon echo spectroscopies," Annu. Rev. Phys. Chem. **49**, 99-123 (1998).

[31] K. Misawa, T. Kobayashi, "Utrafast dephasing measurement by transient four-wave mixing," Mol. Cryst. Liq. Cryst. **182A**, 125-137 (1990).

Chapter 3

High Intensity Pulse Propagation in Dielectric Interference Filters

3.1 Introduction

Multi-layer dielectric structures have traditionally found application in both high-reflecting and anti-reflection coatings and in the construction of optical interference filters[1]. More recently there has been considerable interest in the development of new methods for thin-film deposition of dielectric materials that also exhibit large optical nonlinearities for optical switching applications[2][3][4][5]. Advances in the development of new dielectric materials that include nanoscale structures to finely control the refractive index profile, now enable the construction of gradient indexed structures that find application as antireflection coatings and narrow-band filters capable of reflecting multiple wavelengths[6][7][8]. In addition to the development of new deposition technologies, new techniques to characterize the optical and mechanical properties of these novel thin-film structures are becoming increasingly important[9][10].

The simplest quarter-wavelength dielectric stack structures consist of a repeated sequence of $\lambda/4$ layers of two materials with different indices of refraction. These high-reflecting filters have been studied for over a century and yet still find extensive use in modern optics laboratories. To both optimize the reflected bandwidth and to eliminate the reflectance of higher-order harmonics, there have been several variations on the design of optical filters. These include gradient-index structures which previously had found application as antireflection coatings[7] and rugate structures where the index of refraction is engineered to vary continuously in a sinusoidal manner along the direction of propagation[11][12]. Alternatively,

rugate like structures can be constructed from a series of very thin discrete layers which produce the effect of a sinusoidal refractive index modulation over distances comparable with the wavelength of light[13]. This type of structure is now finding commercial application as narrow-band high-reflecting optical filters.

Over the past decade it has become possible to purchase commercial laser systems that are capable of generating ultrashort optical pulses with sufficiently high intensity to induce nonlinear optical effects in many of the materials that are used in the construction of optical components. Dielectric structures that are well characterized as high reflectors at low intensities are expected to change their reflective properties when interacting with high-intensity ultrashort pulses. The investigation and optimization of the optical properties of interference filters in the presence of nonlinear effects has been of interest for some time[14]. Bovard *et al.* have adapted the characteristic matrix method to account for both thermal and intensity dependent refractive index (n_2) effects on the transmittance, reflectance and absorptance of these structures; however, this method only explores how the nonlinear optical effects modify the optical properties of the filter and not how these changes affect the electric and magnetic fields of the reflected ultrafast optical pulse[15][16].

The finite difference time domain (FDTD) method was used to numerically integrate the Maxwell curl equations to obtain both the electric and magnetic fields[17]. While FDTD techniques were originally developed for isotropic media[18], rapid advancements in the speed, memory and storage of electronic computers enable FDTD methods to be applied to a wide range of problems including optical pulse-material interactions on the femtosecond timescale. In this chapter the FDTD method was used to investigate both the reflection of high intensity ultrashort optical pulses from dielectric thin-film structures and the associated frequency modification and distortion of the reflected pulses.

3.2 Multilayer Dielectric Structures

The computer simulations described in this chapter were performed using three types of multilayer thin-film structures. The first structure is a simple quarter-wavelength dielectric stack consists of a repeated sequence of $\lambda/4$ layers of two materials with different indices of refraction[19]. The quarter-wave stack modeled in these simulations was designed to have high reflectance at a central wavelength of 800 nm and was comprised of 14 cycles of Ta_2O_5 and SiO_2 on a SiO_2 substrate. Table 3.1 shows the linear, nonlinear optical properties and damage thresholds of Ta_2O_5 and SiO_2. Fig. 3.1(a) shows the index of refraction profile of the quarter-wave dielectric stack. An analytical calculation of the reflectance spectrum for this structure reveals high reflectance at the design wavelength of 800 nm as well as high reflectance at higher-order odd harmonics as shown in fig. 3.1(b).

Rugate structures are dielectric filters where the index of refraction varies sinusoidally on the order of the wavelength of the incident light. Fig. 3.1(c) shows 14 cycles of a rugate filter and (d) its reflectance spectra. It can be seen from the reflectance spectra that rugate structures have the advantage over quarter-wave dielectric stacks in that they do not reflect higher order odd harmonics. Although gradient-index rugate structures have been produced using varying concentrations of Nb_2O_5 and SiO_2, they are generally quite difficult to manufacture on a large scale[13][20].

An alternative approach to rugate production is to use two separate materials and to vary the optical distance the light propagates sinusoidally within the optical filter rather than a variation of the index of refraction. This approach to the rugate design has proven successful because rugate structures appear to be quite robust with respect to variations from a purely sinusoidal index profile and although not a true rugate structures these discrete rugate filters have similar properties to a the continuous rugate[13]. Fig. 3.1(e) shows the index of refraction profile of four cycles of a 22 layer discrete rugate structure, constructed of two dielectric media, also Ta_2O_5 and SiO_2, on a SiO_2 substrate. This rugate structure was designed to have a maximum reflectance at a wavelength of 800 nm. Fig. 3.1(f) shows the

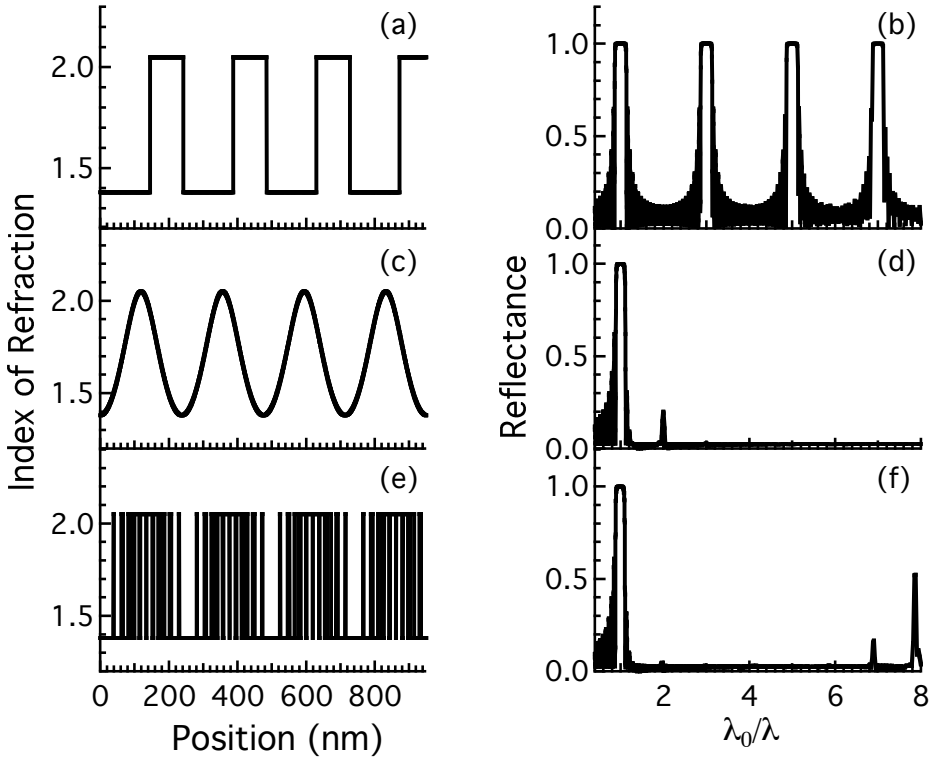

Figure 3.1: Refractive index profiles for (a) four cycles of a quarter-wave dielectric stack interference filter, (c) four cycles of a continuously varying rugate filter and (e) four cycles of a 22 layer discretely varying rugate filter constructed from Ta_2O_5 and SiO_2 layers. Panes (b),(d) and (f) show the corresponding reflectance spectra. The reflectivity of the rugate structures is suppressed at $n\lambda_0/\lambda$ as compared with the quarter-wave stack.

reflectance spectra calculated for the discrete rugate using characteristic matrix techniques. The discrete rugate indeed exhibits a narrow-band high reflectance feature at the design wavelength and a suppression of the reflectivity at the higher-order odd harmonics similar to the true rugate structure.

To calculate the reflectance spectra of the dielectric structures, the characteristic matrix method was used[19]. Appendix A has a detailed discussion of the characteristic matrix calculations. The characteristic matrix calculations were performed using a program written using Fortran 95 and were performed on the structures discussed in section 3.2. Characteristic matrix calculations were performed on filters on resolution of 8 nm to 80 pm. Fig. 3.1 shows the reflectance spectra for the three optical filters discussed in section 3.2, the resolution of the calculations was 80 pm and it can be seen that characteristic matrix calculations at high resolution can yield accurate results for over a significant part of the spectrum. The results from the characteristic will be used for a comparison with FDTD simulations.

Table 3.1: Linear optical, nonlinear optical and damage threshold parameters for Ta_2O_5 and SiO_2.

Material	n_0	$\chi^{(3)}$	Threshold Intensity	Threshold Fluence
Ta_2O_5	2.06 [3]	1.07×10^{-20} m^2/V^2 [21]	6.1 TW/cm^2 [22]	0.7 J/cm^2 [23]
SiO_2	1.38 [24]	1.48×10^{-22} m^2/V^2 [21]	78 TW/cm^2 [25]	2.5 J/cm^2 [23]

3.3 Finite Difference Time Domain Simulations

To simulate the reflection of high intensity ultrafast pulses from the structures described in section 3.2, an in-house 1-D finite difference time domain (FDTD) code was implemented in Fortran 95. The FDTD algorithm are obtained by numerically integrating Maxwell's curl equations. The following derivation of the FDTD algorithms follows the treatment used in the seminal text on the subject by Taflove *et al.*[17]. The FDTD method[17] uses an algorithm developed by Yee[18] to numerically integrate the Maxwell curl equations for the electric and magnetic fields. A detailed discussion of Yee algorithm can be found in appendix B. The

simulations performed in this chapter were performed using only one dimension. Assuming the optical pulse is propagating in the z direction and the electric is polarized in the x direction, the magnetic field must be in the y direction. The 1-D FDTD algorithm is then limited to a system of two equations. This FDTD model will use the following convention. The electric fields will be calculated on the spatial grid while the magnetic fields will be calculated between each grid step. Fig. B.2 shows a schematic of both the temporal and spatial "leap-frog" convention that will be used. The FDTD equations can then expressed

$$E_x|_k^{n+1} = C_a|_k E_x|_k^n + C_b|_k \left(H_y|_{k+1/2}^{n+1/2} - H_y|_{k-1/2}^{n+1/2} \right) \tag{3.1}$$

$$H_y|_{k-1/2}^{n+1/2} = D_a|_k H_y|_{k-1/2}^{n-1/2} + D_b|_k \left(E_x|_k^n - E_x|_{k-1}^n \right). \tag{3.2}$$

These equations can be used to calculate the electric and magnetic fields in one dimension. The material parameters C_a, C_b, D_a, and D_b can be read directly from parameter files containing material information. The Yee algorithm/grid combination can be shown to be divergence-free in the absence of electric and magnetic sources.

To validate the FDTD simulations as the electromagnetic wave propagated through a dielectric media dispersion the FDTD simulations can be adapted to account for the dispersive properties of the material. Linear dispersion can be taken into account using several dispersion models including the Debye model or Lorentz models[26]. To modify the FDTD algorithms to account for the dispersive properties of the dielectric material the auxiliary differential equation method was employed. The auxiliary differential method uses the simi-implicit approximation to express an additional differential equation that can be solved simultaneously with Maxwell's curl equations in term of the Yee algorithm. Appendix C shows a detailed application of the auxiliary differential equations method for a Lorentz dispersive model. In the presence of a Lorentz dispersive media, the calculations of the electric and magnetic fields then become a three step process. First the electric field $E|^{n+1}$ is

calculated using the stored values of $E|^n$, $E|^{n-1}$,$J_p|^n$,$J_p|^{n-1}$, and $H|^{n+1/2}$ using

$$\begin{aligned} E|^{n+1} &= C_1 E|^{n-1} + C_2 E^n \\ &\quad + C_3 \left(\nabla \times \vec{H} - 1/2 \sum_{p=1}^{P} \left[(1+\alpha_p) J_p|^n + \xi_p J_p^{n-1} \right] \right) \end{aligned} \tag{3.3}$$

where

$$\begin{aligned} C_1 &= \frac{1/2 \sum_{p=1}^{P} \gamma_p}{2\epsilon_0 \epsilon_\infty + 1/2 \sum_{p=1}^{P} \gamma_p + \sigma \Delta t} \\ C_2 &= \frac{2\epsilon_0 \epsilon_\infty - \sigma \Delta t}{2\epsilon_0 \epsilon_\infty + 1/2 \sum_{p=1}^{P} \gamma_p + \sigma \Delta t} \\ C_3 &= \frac{2\Delta t}{2\epsilon_0 \epsilon_\infty + 1/2 \sum_{p=1}^{P} \gamma_p + \sigma \Delta t}. \end{aligned} \tag{3.4}$$

The curl of the magnetic field is accounted for using the simi-impicit approximation. Next an updated value of the current density of associated with the p^{th} Lorentz pole pair ($J_p|^{n+1/2}$) is calculated using the updated value of the electric fields using

$$\begin{aligned} J_p|^{n+1/2} &= \frac{1}{2} \left(J_p|^n + J_p|^{n+1} \right) \\ &= \frac{1}{2} \left[(1+\alpha_p) J_p|^n + \xi_p J_p|^{n-1} + \frac{\gamma_p}{2\Delta t} (E|^{n+1} - E|^{n-1}) \right]. \end{aligned} \tag{3.5}$$

Finally an updated value of the magnetic field is calculated using equation 3.2.

Similarly, the FDTD algorithm can be adapted to take into account nonlinear optical effects. Third-order nonlinear optical behavior can be introduced as either instantaneous Kerr or delayed Raman processes[27]. The auxiliary differential equation method was used to account for an instantaneous Kerr nonlinearity. Appendix D shows a detailed application of the auxiliary differential method for the nonlinear susceptibility. As with the application of linear dispersion the FDTD algorithm, which accounts for a nonlinear susceptibility, becomes a three step process. First using the stored values of $E_x|^n$, $J_{\text{nl}}|^n$ and $H_y|^{n+1/2}$, $E_x|^{n+1}$ can be calculated using

$$\begin{aligned} 0 &= \frac{\chi^{(3)}}{4} \left[(E_x|_{i+1}^{n+1})^3 + (E_x|_{i+1}^{n+1})^2 (E_x|_{i+1}^{n}) - (E_x|_{i+1}^{n+1})(E_x|_{i+1}^{n})^2 - (E_x|_{i+1}^{n})^3 \right] \\ &\quad - E_x|_{i+1}^{n+1} + E_x|_{i+1}^{n} + \frac{\Delta t}{\epsilon_0 \Delta x} \left(H_y|_{i+1/2}^{n+1/2} + H_y|_{i-1/2}^{n+1/2} \right) - \frac{\Delta t}{\epsilon_0} J_x|_{i+1}^{n}. \end{aligned} \tag{3.6}$$

It is necessary to solve the cubic equation to obtain a value for $E_x|^{n+1}$. This can be accomplished quite efficiently using Newton's method for solving cubic equations. Once a value of $E_x|^{n+1}$ is obtained it can be used to calculate an updated value of the current density associated with the Kerr optical nonlineariy, $J_x|_{i+1}^{n}$ using

$$J_{\rm nl}|^{n+1} + J_x|^n = \frac{3\epsilon_0\chi^{(3)}}{2\Delta t}\left[\left(E_x|^{n+1}\right)^3 + \left(E_x|^{n+1}\right)^2 (E_x|^n) - \left(E_x|^{n+1}\right)(E_x|^n)^2 - (E_x|^n)^3\right]. \tag{3.7}$$

Once an updated value of $J_x|_{i+1}^{n}$ is obtained, an updated value of the magnetic field $H_y|_{i+1/2}^{n+1/2}$ can be calculated using the standard Yee algorithm.

The FDTD method is particularly appropriate for simulating multilayered structures as it enforces the field boundary conditions between dissimilar media. Furthermore, the fine grid required by the FDTD method is also necessary to accurately describe the rapidly spatially varying refractive index profile associated with the multilayer structures. Due to the small thickness (< 5 μm) of both the quarter-wave and the rugate structures, the effect of linear dispersion was neglected for both SiO_2 and Ta_2O_5; linear absorption was neglected for the same reason. A Kerr nonlinearity was included for Ta_2O_5 using an algorithm based upon the work of Goorjian *et al.*[27]; however, since the value of $\chi^{(3)}$ for SiO_2 is nearly two orders of magnitude lower than that of Ta_2O_5 (see table 3.1), nonlinear effects in the SiO_2 layers were neglected.

The FDTD simulations were performed with a spatial resolution $\lambda/200$. Higher resolution simulations ($\lambda/400$ and $\lambda/800$) were also performed to test for convergence. To validate our code, the results from low intensity FDTD simulations was to generate reflectance spectra that could be compared with analytic reflectance spectra calculated using the characteristic matrix method as detailed below. The accuracy of the nonlinear optical effects was tested by studying soliton propagation in a dispersive nonlinear medium and comparing the results to those of Ref. [27]. It should be noted that although some of the pulses in the simulations described below were of sufficient intensity to generate higher-order nonlinear optical effects

to be present, this model has been restricted in this study to purely third-order nonlinear effects.

Unlike the quarter-wavelength dielectric stack, the idealized rugate structure and discrete rugate structure contains individual layers that can be on the order of or even smaller than the spatial resolution used in the simulations. The discretization of these structures therefore effectively changes the layer thickness on the order of the spatial step-size and even excluding the thinnest layers. For comparison of these simulations with analytic calculations the following procedure was used: an idealized rugate structure was designed, the structure at the resolution of the simulation was descretized and the characteristic matrix method was used to calculate the reflectance spectrum of the discretized structure.

To rapidly extract reflectance spectra from the FDTD calculations, the reflection of a low intensity, ultrafast ($\tau_{\mathrm{p}} = 5\,\mathrm{fs}$), broad bandwidth ($\Delta\lambda_{\mathrm{FWHM}} \approx 196\,\mathrm{nm}$) pulse from both the quarter-wave dielectric stack and the rugate structures was simulated. The incident and reflected electric field pulses were Fourier transformed, converted to intensity, and divided to form a ratio. Fig. 3.2 shows the reflectance spectra of both (a) a quarter-wave dielectric stack, (c) a continuous rugate structure and (e) a discrete rugate structure calculated using the characteristic matrix method. The FDTD simulated spectra for each structure, shown in panes (b), (d) and (f), are in good agreement with the analytic results. This figure also shows that the reflectance spectra of the rugate filters and dielectric stack when constructed with the limited spatial resolution of the FDTD simulation still exhibit the optical properties (*e.g.* center wavelength) of the idealized structures, thus indicating the insensitivity of these devices to small imperfections.

3.4 Results and Discussion

The FDTD method was used to simulate the reflection of 50 fs optical pulses from quarter-wave dielectric continuous rugate and discrete rugate interference filters for intensities between $13.2\,\mu\mathrm{W/cm^2}$ and $10\,\mathrm{TW/cm^2}$ at three wavelengths 750, 800 and 850 nm. The

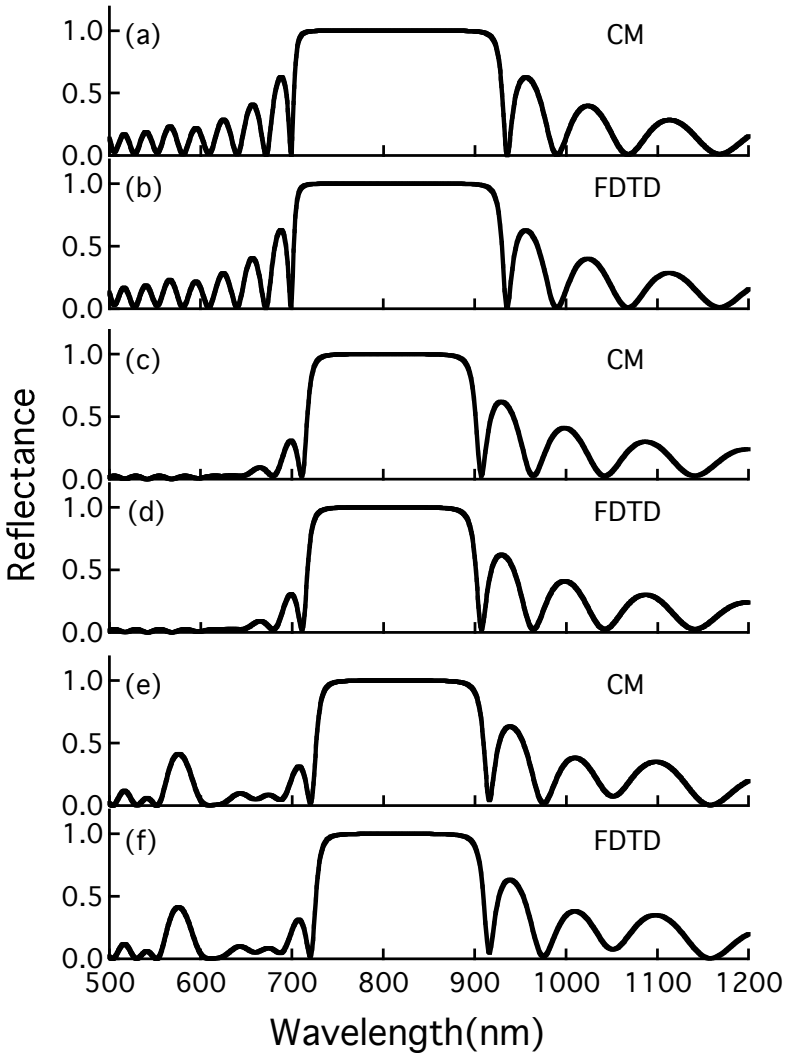

Figure 3.2: Reflectance spectra: panes (a) and (b) show the reflectance spectra of a quarter-wave dielectric stack calculated using the characteristic matrix (CM) method and simulated using the FDTD method, respectively; panes (c) and (d) show the reflectance spectra of a continuous rugate filter calculated using the characteristic matrix method and simulated using the FDTD method, respectively; panes (e) and (f) show the reflectance spectra of a discrete rugate filter calculated using the characteristic matrix method and simulated using the FDTD method, respectively.

lower-bound on the intensity was chosen so that nonlinear effects were negligible. The upper-bound on the intensities can be easily exceeded using modern table-top laser systems; however, it is also above the intensity damage threshold for the Ta_2O_5 layer. Within these bounds, nonlinear optical effects are expected to both adversely effect the performance of the optical filters and modify the reflected optical pulse.

Fig. 3.3 plots reflectance as a function of incident pulse intensity for the quarter-wave stack continuous rugate and discrete rugate structures. Fig. 3.3 illustrates that while high intensity pulses effect the performance of all structures they do so to different extents. For all structures, the incident pulse intensity increases while the reflectance of the structure decreases; this decrease in reflectance is accompanied not only by an increase in the transmittance but also by the development of optical trapping (not shown) within the structure. The error in fig. 3.3 is on the order of the linewidth. The vertical grey bar in this figure indicates the intensity damage threshold of the structures.

At all three wavelengths studied, the reflectance of the quarter-wave dielectric stack changes only slightly as the intensity of the incident pulse increases; furthermore, the reflectance of this device is not significantly reduced, even well above the damage threshold. The continuous rugate structure shows similar results to the quarter-wave dielectric stack. The reflectance of all three wavelengths show little change as the incident intensity is increased. The discrete rugate structure exhibits similar behavior to the continuous rugate structure though the changes in the reflectance are more exaggerated. At both the 800 nm and 850 nm pulse wavelengths, the change in reflectance, while somewhat greater than that observed for the continuous rugate filter, is still negligible. It is important to note that the 750 nm reflectance is noticeably reduced. The sensitivity of the rugate structure to incident pulses at wavelengths shorter than the central wavelength can be understood in terms of the following mechanism. Ta_2O_5 has a positive $\chi^{(3)}$ which causes the index of refraction to increase with increased intensity. The optical thickness of the Ta_2O_5 layers is therefore

increased, effectively tuning the filter to longer wavelengths[28]. Similar effects have been observed in simulations of nonlinear Fabry-Perot cavities[2].

To gain a greater understanding of the behavior of the optical filters at frequencies both above and below the peak reflectance of the filter, the reflectance of the optical filters was calculated as a function of intensity over a broad spectral range. Fig. 3.4 shows the results of reflectance of 50 fs optical pulses reflecting from a quarter-wave dielectric stack with a central wavelength between 500 nm and 1200 nm in 100 steps. The resulting image plot shows that the magnitude of the central reflectance peak changes little at high intensities. It is also apparent that the central reflectance peak broadens at high intensities. This is consistent with the central wavelength shifting to the red as the intensity of the incident pulse is increased. There is also a decrease of the minor reflectance peaks of the off resonance frequencies.

Fig. 3.5 shows the reflectance of a continuously varying rugate structure as a function of the intensity of a central wavelength range between 500 nm and 1200 nm in 100 steps. Similar to the quarter-wave dielectric stack, the ideal rugate filter also shows a red shift of the central wavelength at high intensities. The continuous rugate shows a narrowing of the bandwidth of the high reflectance band which may detune frequencies that lie close to the edge of the reflectance band. As with the quarter-wave dielectric stack, at high intensities the features of the reflectance spectrum become less distinct.

Fig. 3.6 is an image plot showing the reflectance of a discretely varying rugate as a function of the intensity resulting from 50 fs pulse reflections with a central wavelength that varies from 500 nm to 1200 nm in 100 steps. Again the discrete rugate shows the most change in the reflective properties of the three studied filters. It can be seen that the reflectance drops appreciatively at high intensities. The discrete rugate also shows a more dramatic redshift of the central wavelength and narrowing of the reflectance peak. Again at high intensities there is a overall smoothing of the features of the reflectance spectrum.

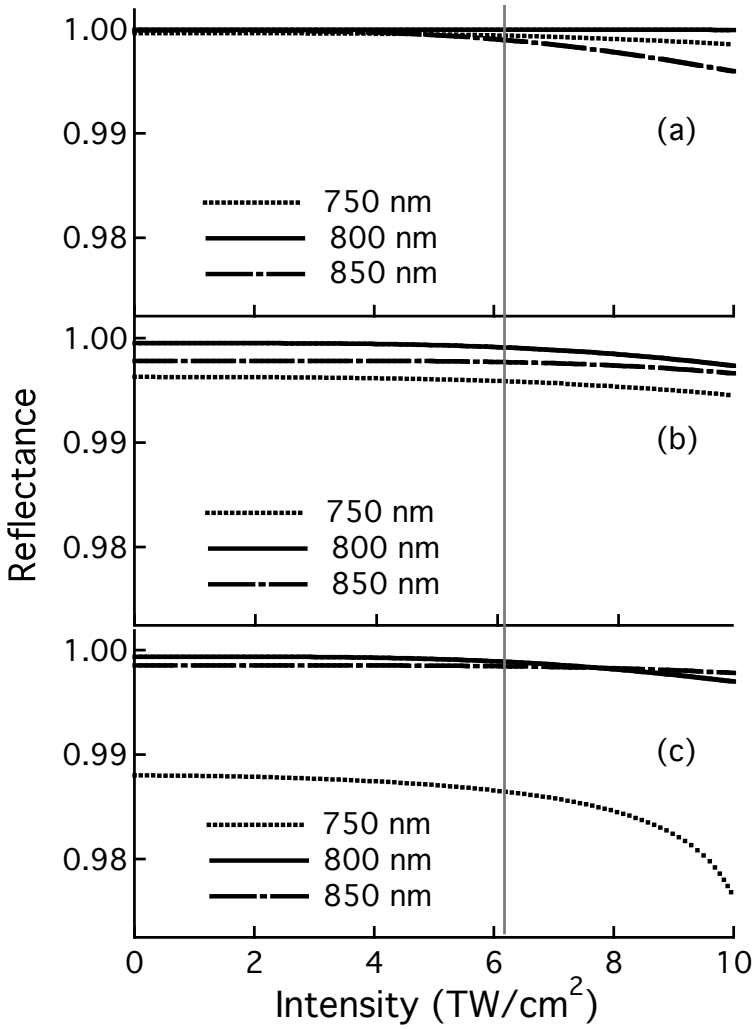

Figure 3.3: Reflectance as a function of intensity for both (a) quarter-wave dielectric stack filters, (b) continuous rugate, and (c) discrete rugate filters at wavelengths 750, 800 and 850 nm. The vertical bar shows the intensity damage threshold for Ta_2O_5 for a 50 fs optical pulse at a wavelength of 800 nm[22].

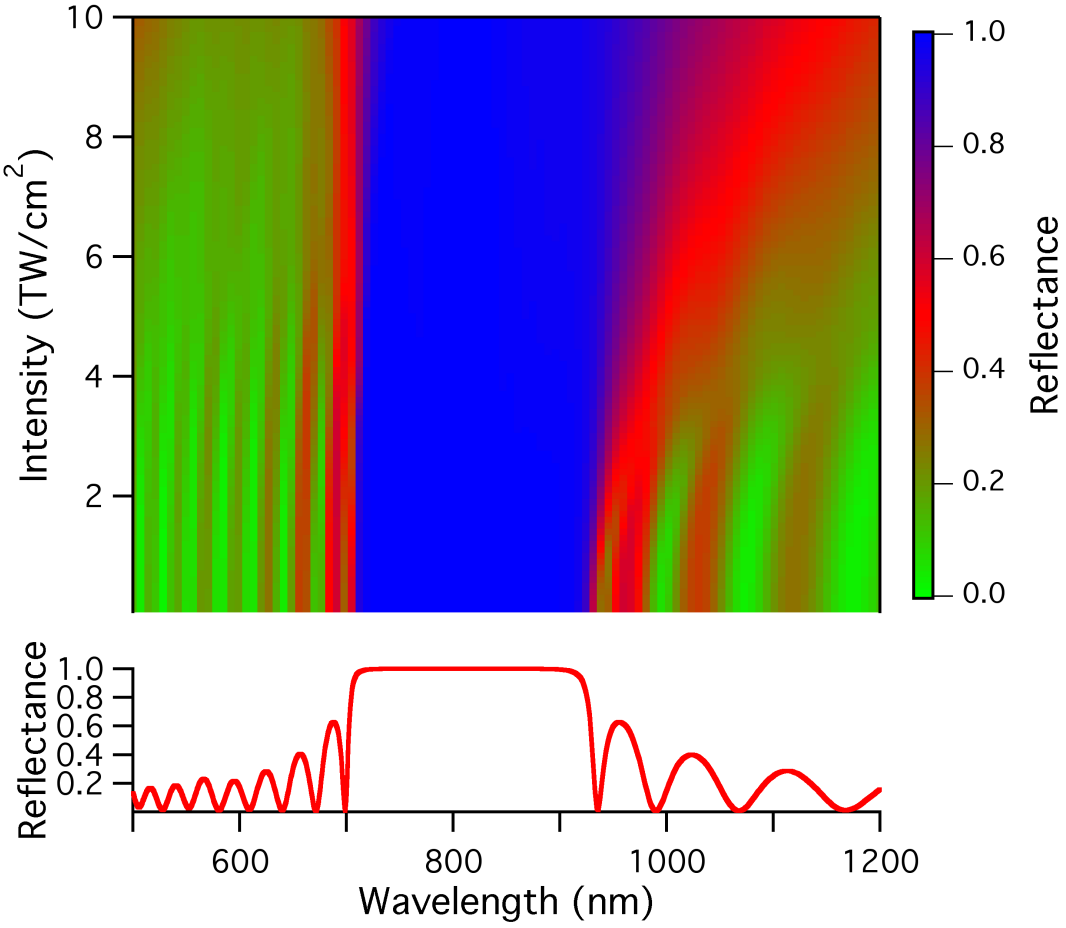

Figure 3.4: Upper pane shows an image plot showing the magnitude of the reflectance as a function of the wavelength and the intensity of the incident pulse for a quarter-wave dielectric stack. Lower pane shows the reflectance for a low intensity pulse (13 μW/cm^2) reflecting from a quarter-wave dielectric stack.

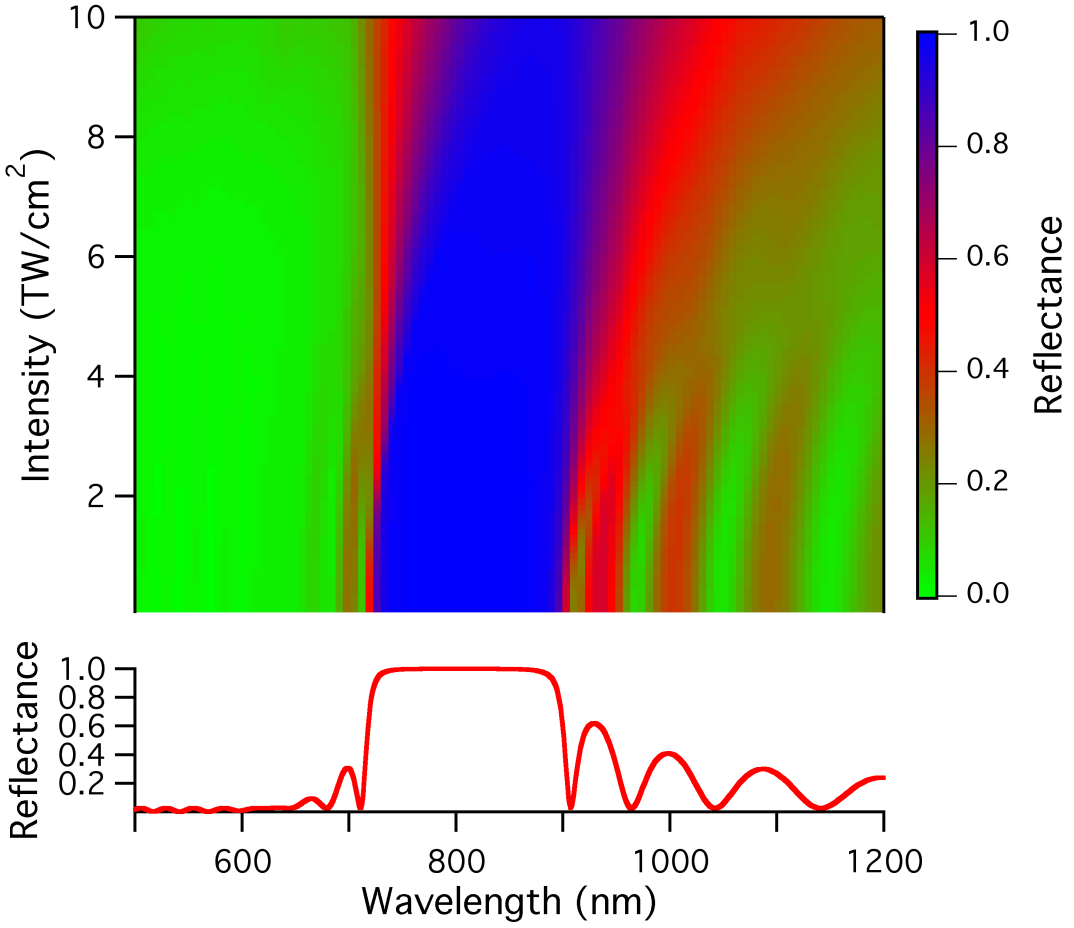

Figure 3.5: Upper pane shows an image plot showing the magnitude of the reflectance as a function of the wavelength and the intensity of the incident pulse for a continuously varying rugate filter. Lower pane shows the reflectance for a low intensity pulse (13 μW/cm^2) reflecting from a continuously varying rugate filter.

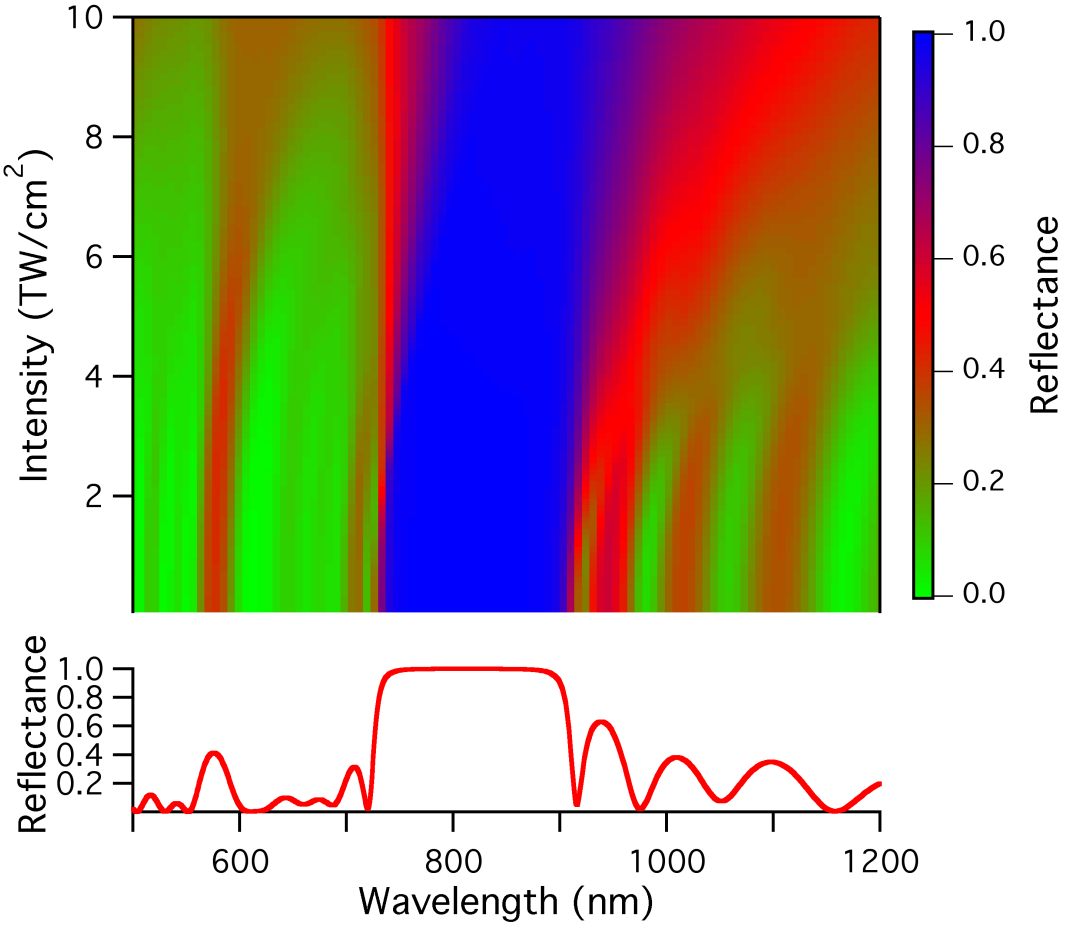

Figure 3.6: Upper pane shows an image plot showing the magnitude of the reflectance as a function of the wavelength and the intensity of the incident pulse for a discrete rugate fitler. Lower pane shows the reflectance for a low intensity pulse (13 μW/cm^2) reflecting from a discrete rugate filter.

To explore the detuning mechanism responsible for changes in the reflectivity at high intensities the field amplitudes were monitored inside the structures. Fig. 3.7 shows the squared magnitude of the electric fields within the discrete vary rugate structure at three wavelengths 750, 800, and 850 nm and three intensities at 13.2 μW/cm^2, 5 TW/cm^2 and 10 TW/cm^2. As the internal intensities increase the nonlinear susceptibility increases the optical distance of the layers adjacent to the surface of the filter. This detuning enables the optical pulse to penetrate into the filter further increasing the effects of $\chi^{(3)}$ on the index of refraction. Fig. 3.7(g) shows the modifications of the electric field with an intensity of 10 TW/cm^2 with an incident wavelength centered at 750 nm. It should be noted that the electric field pattern in fig. 3.7(g) resembles the electric field pattern that is observed in a low intensity off-resonant pulse reflecting from the same structure. Similar results have been observed using the nonlinear characteristic matrix method[15].

In the discussion above investigates how high intensity pulses modify these structures. The modification of the optical properties of the structure distort the reflected pulses. In particular, spectrograms are plotted (fig. 3.8) of the reflection of optical pulses with $\lambda =$ 750, 800 and 850 nm and intensities $I = 13.2\,\mu$W/cm^2, 5 TW/cm^2, and 10.0 TW/cm^2 from the 14 cycle discrete rugate filter. At low intensities it can be seen that the reflected pulse retains the same pulse envelope and spectrum for all incident wavelengths. However, as the intensity is increased, sum frequency generation takes place within the structures and higher order harmonics begin to appear in the spectrograms. At 10 TW/cm^2, the third-harmonic and fifth-harmonic are visible at all incident wavelengths. There are also distortions to the pulse envelope which become more pronounced for 750 nm wavelengths. These distortions are a direct result of the detuning of the rugate filter. Upon closer examination of fig. 3.2 (e) it is shown that 750 nm lies on the edge of the high reflectance band and a slight detuning of the optical filter to the red has a dramatic effect on the frequency range reflected by the rugate filter close to 750 nm reflectance thus distorting the reflected pulse.

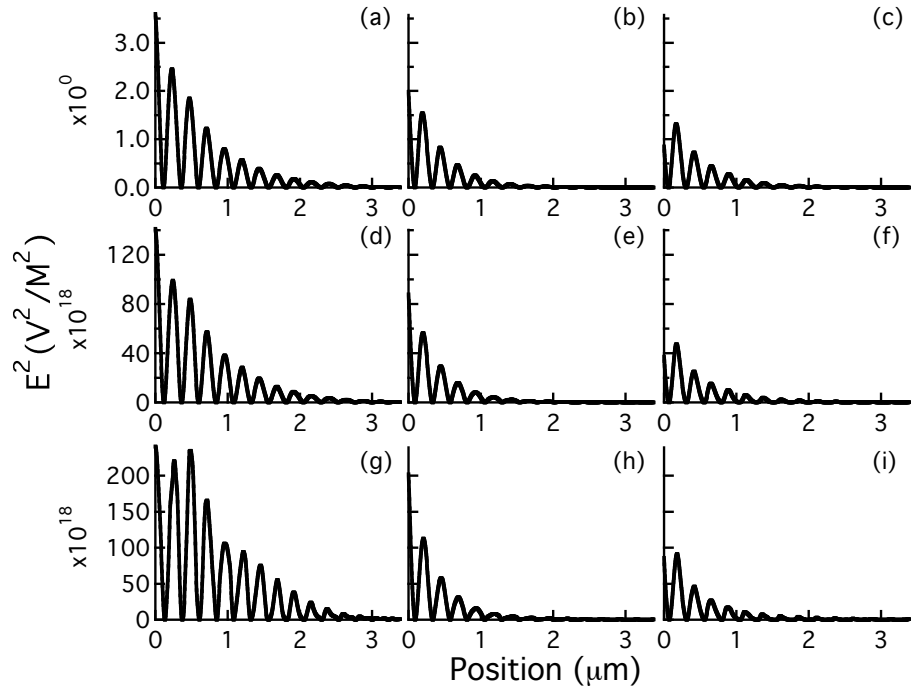

Figure 3.7: Internal electric field magnitudes squared 14 cycle discrete rugate with each cycle of the rugate constructed from 22 layer of alternating layers of Ta_2O_5 and SiO_2 on a substrate of SiO_2 with a central wavelength of 800 nm. Panes (a),(b) and (c) show low intensity (13.2 μW/cm^2) at wavelengths of 750 nm, 800 nm, and 850 nm respectively. Panes (d),(e) and (f) show the internal electric fields at 5 TW/cm^2 and panels (g),(h), and (i) shows 10 TW/cm^2 for 750, 800 and 850 nm respectively.

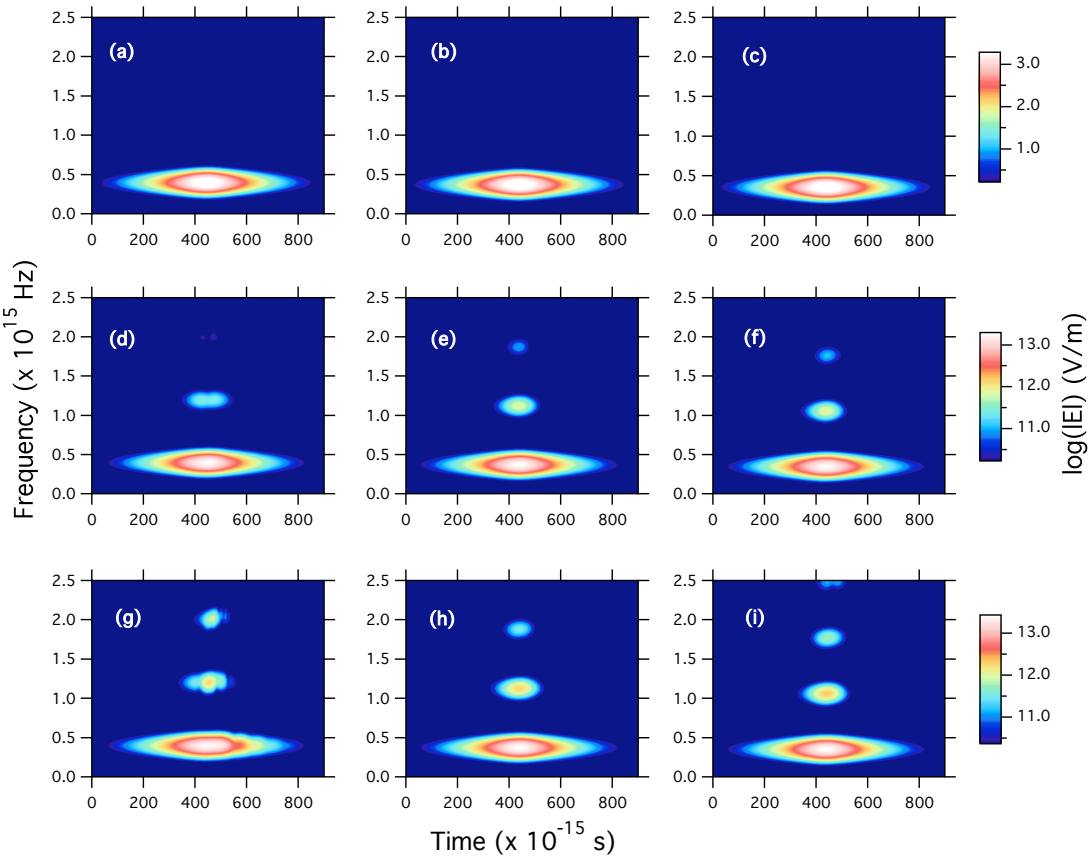

Figure 3.8: Spectrograms and electric-field profiles of 50 fs optical pulses with wavelength 750 nm (a),(d),(g); 800 nm (b),(e),(h); and 850 nm (c),(f),(i); and intensity 13.6 μW/cm^2 (a),(b),(c); 5 TW/cm^2 (d),(e),(f); and 10 TW/cm^2 (g),(h),(i); reflected from a 14 cycle rugate filter with center wavelength 800 nm. Spectrograms: the ordinate labels the frequency (Hz); the abscissa labels time (s); the scale-bar labels the logarithm of the magnitude the electric field (V/m).

While the onset of nonlinear optical effects in the rugate structure occurs quite close to the damage threshold of the Ta_2O_5 layer, some of the more pronounced nonlinear optical effects (such as significant pulse shape distortion) that were only observed at intensities above the damage threshold of the Ta_2O_5/SiO_2 structure will become important in structures with layers of higher $\chi^{(3)}$ materials, *e.g.* Nb_2O_5[3].

3.5 Conclusions

This work used computer simulations based upon the FDTD method to investigate the interaction of high-intensity ultrashort optical pulses with three multilayer dielectric structures: a quarter-wave dielectric stack, continuous rugate filter and a discrete rugate filter. A simulation of the reflection of a low intensity, broad-band pulse was used to determine the reflectance spectra of both structures. The resulting spectra were found to be in good agreement with reflectance spectra calculated using the characteristic matrix method.

For computer simulations using 50 fs pulses, it was observed that as the intensity was increased, nonlinear optical effects caused higher optical harmonics to become evident in the reflected pulse spectra, while intensity dependent refractive index (n_2) effects caused changes in the optical thickness of the Ta_2O_5 layers, effectively detuning the optical properties of the structure. The simulations confirm that the quarter-wave dielectric stack and the continuous rugate maintain their reflective properties up to high intensities. However, the discrete rugate structures, while still quite robust, were more susceptible to nonlinear optical effects at high intensities, especially when used at wavelengths shorter than the center wavelength for which the rugate was designed.

Future work will include exploring the impact of third-order Raman and higher-order optical nonlinearities as well as incorporating models for multi-photon ionization and plasma generation. Potential applications include: the development of both optimized dielectric structures for high intensity operation and novel ultrafast optical switching devices [29].

Simulations that include plasma generation could also provide additional insight into experimental results on optical damage in dielectric materials and structures [30][31]. Ideally the simulations described in this chapter should be compared with experimental data particularly for the rugate filters. However the high cost of the rugate filters ($\approx$ \$6,000) combined with the high probability of optical damage made these experiments impractical.

3.6 References

[1] O. S. Heavens, *Optical Properties of thin Solid Films*, Dover Publishing, Inc., New York, 1991.

[2] S. A. Basinger, D. J. Brady, "Finite-difference time-domain modeling of dispersive nonlinear Fabry-Perot cavities," J. Opt. Soc. Am. B **11**, 1504-1511 (1994).

[3] T. Hashimoto, T. Yoko,"Third-order nonlinear optical properties of sol-gel-derived V_2O_5, Nb_2O_5, and Ta_2O_5 thin films," Appl. Opt. **34**, 2911-2948 (1995).

[4] H. Szymanowski and O. Zabeida and J. E. Klemberg-Sapieha and L. Martinu, "Optical properties and microstructure of plasma deposited Ta_2O_5 and Nb_2O_5 films," J. Vac. Sci. Technol. A **23**, 241-247 (2005).

[5] X. Wang, H. Masumoto, Y. Someno, T. Hirai, "Design and experimental approach of optical reflection filters with graded refractive index profiles," J. Vac. Sci. Technol. A **17**, 206-211 (1999).

[6] M. H. Asghar, M. B. Khan, S. Naseem, "Modeling thin film multilayer broad-band-pass filters in visible spectrum," Czech. J. Phys. **53**, 1209-1217 (2003).

[7] H. Sankur, W. H. Southwell, "Broadband gradient-index antireflection coating for ZnSe," Appl. Opt. **23**, 2770-2773 (1984).

[8] M. G. Berger, R. Arens-Fischer, M. Thönissen, M. Krüger, S. Billat, H. Lüth, S. Hilbrich, W. Theiß, P.Grosse, "Dielectric filters made of PS: advanced performance by oxidation and new layer structures," Thin Film Solids **297**, 237-240 (1997).

[9] C. C. Lee, C. L. Tien, and J. C. Hsu, "Internal stress and optical properties of Nb_2O_5 thin films deposited by ion-beam sputtering," Appl. Opt. **41** 2043-2047 (1997).

[10] F. Richter, H. Kupfer, P. Schlott, T. Gessner, and C. Kaufmannb, "Optical properties and mechanical stress in SiO_2/Nb_2O_5 multilayers," Thin Film Optics **389**, 278-240 (2002).

[11] W. H. Southwell, "Spectral response calculations of rugate filters using coupled-wave theory," J. Opt. Soc. Am. A **5**, 1558-1564 (1988).

[12] B. G. Bovard, "Rugate filter theory: an overview," Appl. Opt. **32**, 5427-5442 (1993).

[13] H. A. Macleod, *Thin-Film Optical Filters*, Institute of Physics Publishing, Philadelphia, 3rd ed. (2001).

[14] B. S. Wherrett, D. Hutchings, and D. Russell, "Optically bistable interference filters: optimization considerations," J. Opt. Soc. Am. B **3**, 351-362 (1986).

[15] B. G. Bovard and H. A. Macleod, "Nonlinear behaviour of optical coatings subjected to intense laser irradiation," J. Mod. Opt. **35**, 351-362 (1988).

[16] B. G. Bovard, "Derivation of a matrix describing a rugate dielectric thin film," Appl. Opt. **27**, 1998-2005 (1998).

[17] A. Taflove and S. C. Hagness, *Computational Electrodynamics the Finite-Difference Time-Domain Method*, Artech House, Boston, London, 3rd ed. (2005).

[18] K. S. Yee, "Numerical solution of boundary value problems involving boundary value problems involving Maxwells equations in isotropic media," IEEE Trans. Antennas and Propagation **14**, 302307 (1966).

[19] See for example: M. Born and E. Wolf, *Principles of Optics*, Pergamon Press, Oxford, 6th ed. (1980).

[20] A. V. Tikhonravov, M. K. Trubetskov, T. V. Amotchkina, M. A. Kokarev, N. Kaiser, O. Stenzel, S. Wilbrandt, and D. Gäbler, "New optimization algorithm for the synthesis of rugate optical coatings," Appl. Opt. **45**, 1515-1524 (2006).

[21] C. Y. Tai, J. S. Wilkinson, N. M. B. Perney, M. C. Netti, F. Cattaneo, C. E. Finlayson, and J. J. Baumberg, "Determination of nonlinear refractive index in a Ta_2O_5 rib waveguide using self-phase modulation," Opt. Exp. **12**, 5110-5116 (2006).

[22] J. Jasapara, A. V. V. Nampoothiri, and W. Rudolph, "Femtosecond laser pulse induced breakdown in dielectric thin films," Phys. Rev. B **63**, 045117 (2001).

[23] M. Mero, J. Liu, and W. Rudolph, "Scaling laws of femtosecond laser pulse induced breakdown in oxide films," Phys. Rev. A. **71**, 115109 (2005).

[24] D. N. Nikogosyan, *Properties of Laser Related Materials, A Handbook*, John Wiley and Sons, New York (1997).

[25] S. W. Winkler, "Anregungskanäle von Elektronen in transparenten Dielektrika durch ultrakurze Laserpulse," Masters thesis, TU-Berlin, Germany (2003).

[26] M. Joseph, S. C. Hagness, and A. Taflove, "Direct time integration of Maxwells equations in linear dispersive media with absorption for scattering and propagation of femtosecond electromagnetic pulses," Opt. Lett. **16**, 1412-1414 (1991).

[27] P. M. Goorjian and A. Taflove, "Direct time integration of Maxwells equations in nonlinear dispersive media for propagation and scattering of femtosecond electromagnetic solitons," Appl. Opt. **17**, 180182 (1992).

[28] See for exmple: R. W. Boyd, *Nonlinear Optics*, Academic Press, Amsterdam, 2nd ed., (2003).

[29] P. Tran, "Optical limiting and switching of short pulses by use of a nonlinear photonic bandgap structure with a defect," J. Opt. Soc. Am. B **14**, 2589-2595 (1997).

[30] M. Mero, J. Zellar, W. Rudolph, "Ultrafast Processes in Highly excited Wide-gap Dielectric Thin Films," in *Femtosecond Laser Spectroscopy* edited by Peter Hannaford, (Springer-Verlag, Berlin, 2005).

[31] S. W. Winkler, I. M. Burakov, R. Stoian, N. M. Bulgakova, A. Husakou, A. Mermillod-Blondin, A. Rosenfeld, D. Ashkenasi, I. V. Hertel, "Transient response of dielectric materials exposed to ultrafast laser radiation," Appl. Phys. A **84**, 413-422 (2006).

Chapter 4

Linear and Nonlinear Spectroscopy of Green Fluorescent Protein

4.1 Introduction: Green Fluorescent Protein

Wild-type green fluorescent protein (GFP) was first isolated from the *Aequorea victoria* jellyfish native to the northwest pacific ocean by Shimomura *et al.*[1] as a companion protein to the chemiluminescent protein *aequorea*[2]. GFP has been propelled from relative obscurity to one of the most widely studied proteins[3] with a variety of applications that include fluorescent labeling in biological systems[4], lasing[5], and as a sensitive probe of pH[6]. Fig. 4.1(a) illustrates the structure of GFP. The protein is formed by 238 amino acids forming 11 β-sheets which in turn form a cylindrical β-barrel with a diameter of 24 Å and height of 42 Å[7]. The chromophore, which lies in the center of the barrel structure, is formed by the autocatalytic, posttranslational cyclization and oxidation of the tripeptide Ser^{65}–Tyr^{66}–Gly^{67} in the primary structure of the expressed protein[8]. Fig. 4.2 shows the excitation and emission spectra of the GFP studied in this study. The chromophore of GFP has two excitation peaks one with a maximum at 396 nm and the other with a maximum at 476 nm, and it has a fluorescence peak at 509 nm[9]. The absorption peaks correspond to two species of GFP which are differentiated by having a neutral and anionic chromophore respectively; it is interesting to note that the emission of both variants overlaps. Since the discovery of GFP a family of fluorescent proteins has been produced with emissions covering the visible spectrum[10]. Each protein has a similar protein backbone as well as slight variation in the structure of the chromophore[3]. In this study GFP was characterized in two hosts. The first was GFP in a solution of DMSO and water, and the second was GFP embedded in a polyacrylamide polymer film.

This chapter will discuss the characterization of several of the linear and nonlinear optical and spectroscopic properties of GFP. In particular, time correlated single photon counting was used to investigate the effects of host materials on the lifetime (T_1) of GFP[11]. To gain a deeper understanding of the influence of the environment on the chromophore, the proteins were placed under high hydrostatic pressure and the resulting spectral shift were compared to the spectral shifts observed in a protein fluorescent proteins with a similar structure and chromophore.

GFP has been shown to have a large two-photon cross-section when excited with 780 nm to 800 nm light; since this spectral range overlaps with the emission of Ti:Sapphire femtosecond laser systems[8][12], GFP makes an ideal fluorescent marker for two-photon imaging applications. Kirkpatrick *et al.*[8] have measured the two-photon absorption cross-sections for GFP on a femtosecond time scale using the Z-scan technique and has observed that the two-photon absorption cross-section saturates as a function of the intensity. The measurements of the two-photon absorption cross-section described in this chapter were performed on the nanosecond time-scale at much lower intensities and augment the earlier results.

4.2 Determination of the Population Lifetime T_1

The fluorescence lifetimes of molecules and systems of molecules that occur on the time-scale of 10 ns or longer can be easily measured using a variety of techniques, for example multiphoton counting or gated boxcar averaging. When fluorescent lifetimes are on the order of 5 ns or less it is necessary to employ more sophisticated techniques to measure the excited state lifetime. Since modern electronics respond on a nanosecond time scale it is necessary to use techniques that do not measure the excited state lifetime directly but rather use an indirect method to obtain the necessary information required to make lifetime measurements. Time correlated single photon counting (TCSPC) uses many excitation pulses to build up a histogram of the interval between the excitation of the sample and the emission of a single photon. The fluorescence lifetime can be extracted from this histogram.

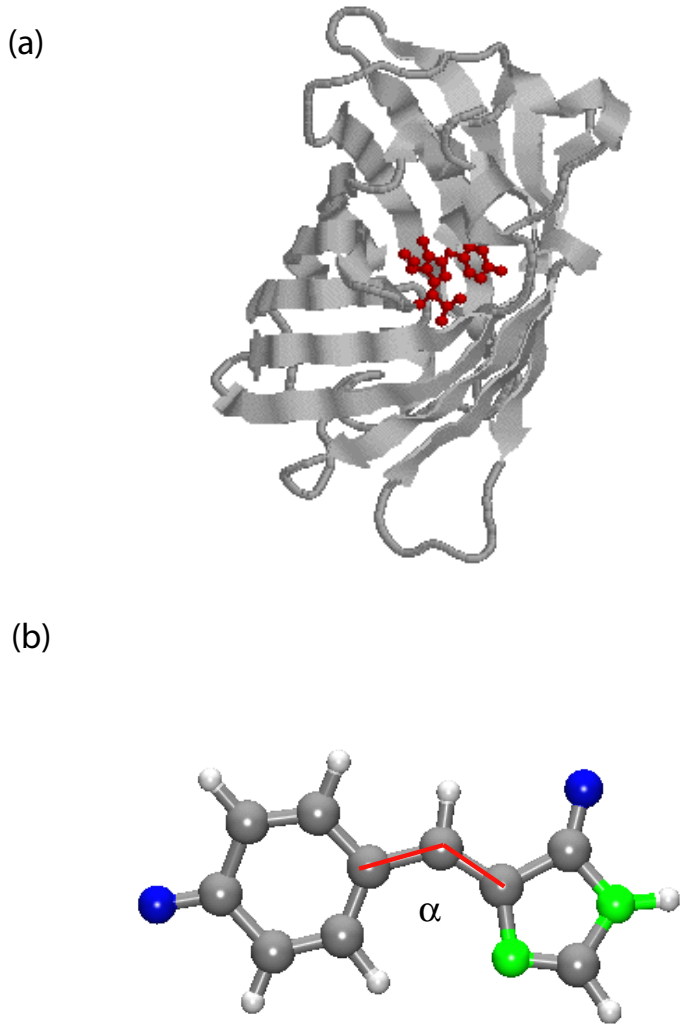

Figure 4.1: (a) The cartoon structure of GFP with the chromophore highlighted in the center of β-barrel structure. (b) A ball and stick model of the hydrogen truncated chromophore. The angle α is denoted for the discussion in section 4.3

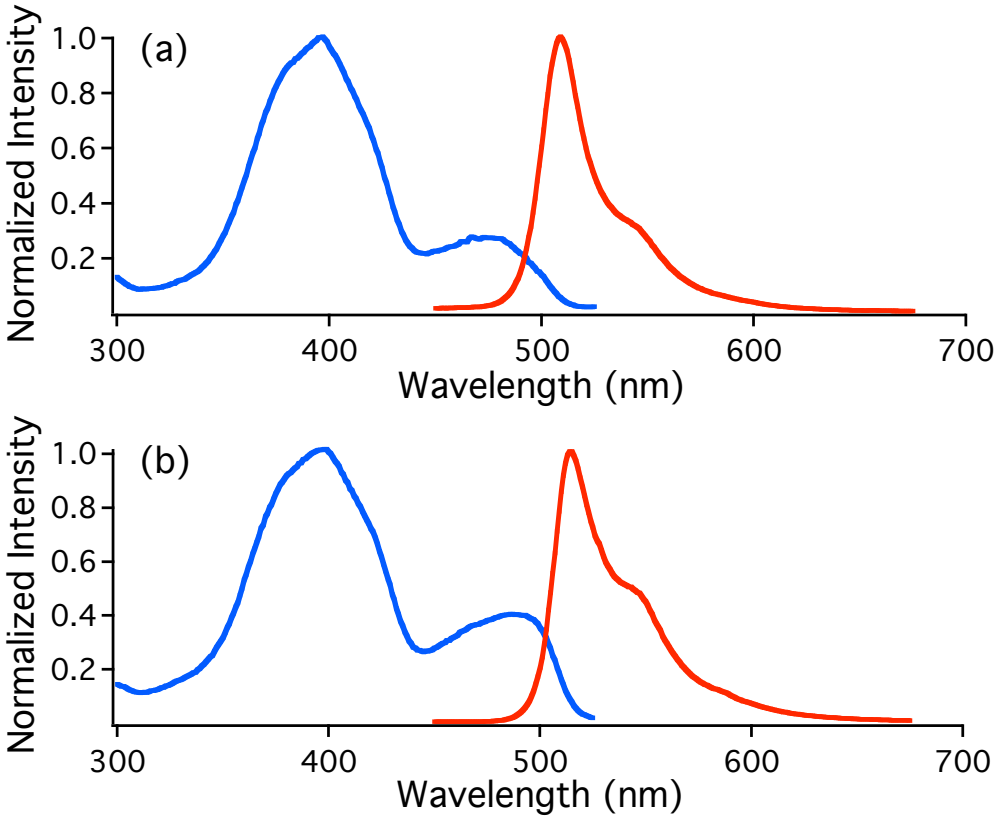

Figure 4.2: (a) Excitation (blue line) and emission (red line) spectra of GFP in an aqueous solution. (b) Excitation (blue line) and emission (red line) spectra of GFP in polyacrylamide film.

4.2.1 EXPERIMENTAL

The time correlated photon counting system used in this work was comprised of both standard optical components and homebuilt equipment. The excitation source, a Spectra-Physics Tsunami, mode-locked Ti:Sapphire laser, was described in detail in section 2.2. In this case, the femtosecond pulses were frequency doubled to a central wavelength of 394 nm. An acousto-optic modulator (AOM) was used to select individual pulses from the femtosecond pulse train.

The optical pulses input the TCSPC system which is separated into three compartments to reduce scattered light. Fig. 4.3 shows a schematic of the experimental setup used for the TCSPC measurements. The first compartment contains a beam-splitter which splits a small fraction of the incident incident pulse-train for use as a trigger. The high intensity fraction of the laser pulse-train is reflected off two steering mirrors and is focused into the second compartment. In the second compartment the optical pulse is focused onto the sample. The sample holder is designed to accommodate a 1 cm cuvette but could be adapted to fit nonuniform shaped samples. It contains two perpendicular polarized windows to eliminate the reflection of the excitation pulse into the detection arm. The temperature of the sample-holder was controlled by passing either heated or chilled water through the sample block. The emission from the sample enters the third chamber and is focused using a concave mirror onto the entrance slits of a monochromater (Applied Photo Physics f/3.4). The monochromater spectrally filters the emission before detection using a multichannel plate (Hamamatsu, Model R28090) .

Since TCSPC requires a maximum emission of one photon per excitation shot, the incident energy was adjusted to allow an emission of one emission photon for every 100 excitation pulses. The frequency of the arrival of the emission photons were counted using a frequency counter. Attenuation of the excitation pulse was accomplished using both neutral density filters before the excitation enters the TCSPC system and filters that can be inserted between the first and second compartments.

The signal from the multi-channel plate was amplified using a EG&G Ortec Model 9306 1 GHz preamplifier. A EG&G Ortec Model 9307 pico-timing discriminator was used to select the amplified emission pulse from the dark noise produced be the multi-channel plate. The TTL pulse that was emitted from the discriminator was then used as a trigger for a Tennelec TC 864 time to amplitude converter (TAC). The TAC was used as a timer and works in the following manner. An initial pulse triggers the TAC which begins to to ramp up a potential difference. A second pulse then stops the voltage ramp, the potential is then measured by a multi-channel scaler contained in a computer card. The TAC can be overloaded if the repetition rate of the start pulses is too large. To circumvent this problem, the trigger used to start the TAC is the signal pulse. This ensures that the TAC will only activate if there is a signal pulse to be counted and the delayed trigger pulse from the following excitation pulse stops the TAC. The resulting voltages are then stored using multi-channel scaler in the computer as a reversed histogram of the time distributions between the excitation pulse and the following trigger pulse. The fluorescence lifetime is then obtained by fitting an exponential to the TCSPC signal.

4.2.2 Results and Discussion

Time correlated single photon counting was used to measure the fluorescence lifetime of GFP in both an aqueous solution and in polyacrylamide film. Fig. 4.4 shows the resulting fluorescence transients for GFP in an aqueous solution for various emission wavelengths. All of the decay curves with wavelengths longer than 470 nm display single exponential decay characteristics. In order to determine the excited state lifetime from the decay curves for wavelengths longer than 470 nm, an exponential function was fitted to the experimental data to extract a value of 3.4 ns. From this value an oscillator strength of 0.31 was calculated for GFP. Using fig. 4.2 it can be seen that the emission below 470 nm lies within the excitation band of GFP. The non-exponential decay may indicate energy transfer between GFP dimers.

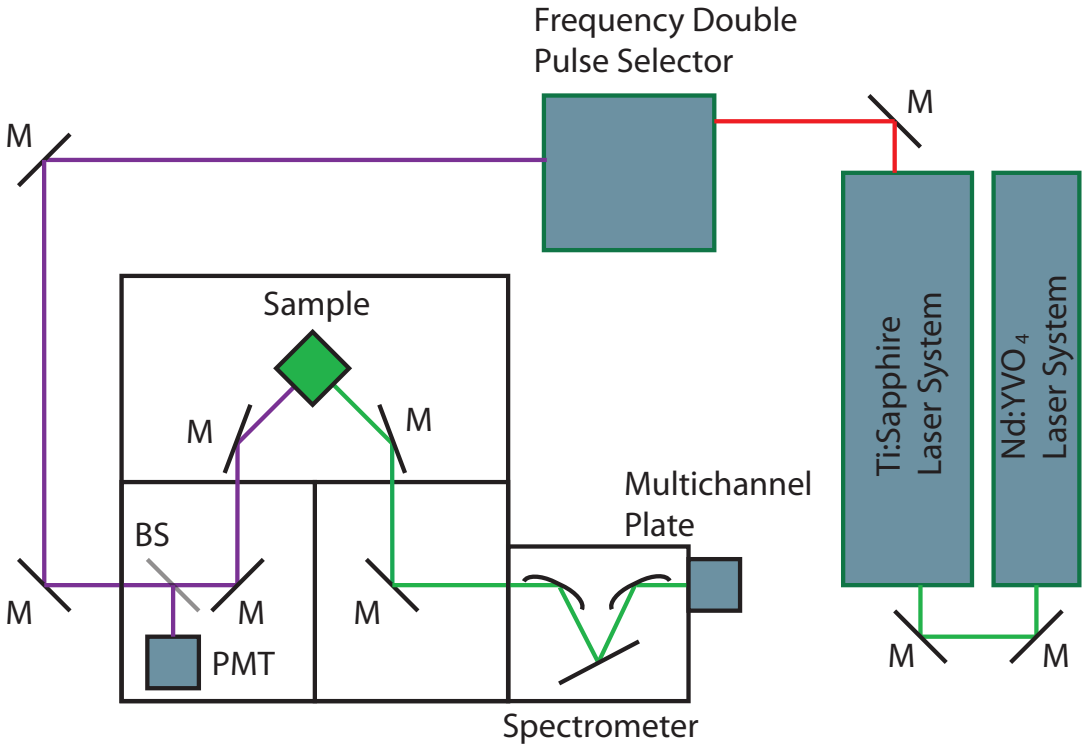

Figure 4.3: Schematic diagram showing the setup of the time correlated single photon counting system. M corresponds to mirrors, BS corresponds to a pick-off beamsplitter, PMT corresponds to the trigger photomultiplier tube. The GFP sample was excited using a doubled Ti:Sapphire laser pulse with a central frequency of 394 nm. The fluorescence wavelength was selected using the exit spectrometer and detected using a multichannel plate.

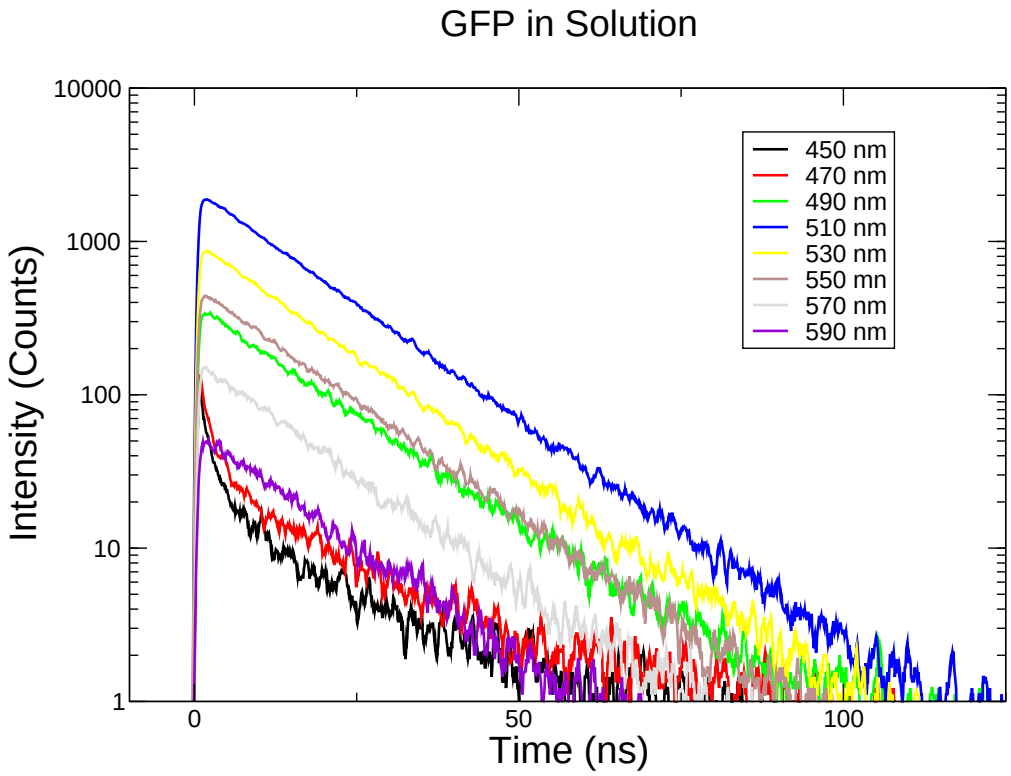

Figure 4.4: Plot showing the decay of the excited state lifetime decay of GFP in solution. For emission that does not overlap into the excitation band, the extracted decay time is 3.4 ns. The non-exponential decay when the emission band overlaps the excitation band may indicate energy transfer between GFP dimers as well as providing evidence for inhomogeneous broadening.

Table 4.1: Excited state lifetime of GFP in several materials.

Sample Host	Excitation Wavelength (nm)	Excited State Lifetime (ns)	Source
H_2O/DMSO	394	3.4	This Study
Polyacrylamide Film	394	2.7	This Study
Tris-HCl buffer/NaCl	400	3.16	Volkmer *et al.* [12]
Tris-HCl buffer/NaCl	800	3.10	Volkmer *et al.* [12]
Mammalian Cell	800	2.4	Tirlapur *et al.* [13]

Similarly the TCSPC measurements were made on the GFP in the polyacrylamide film sample. Fig. 4.5 shows the resulting fluorescence transients for wavelengths between 450 nm and 590 nm. Again for wavelengths larger than 470 nm the excited state lifetime behaves exponentially. The resulting excited state lifetime was determined to be 2.7 ns. This lifetime yields the same oscillator strength as that for GFP in the aqueous solution indicating that the difference in the fluorescence lifetimes is merely due to local field effects. Table 4.1 shows the measured values of the excited state lifetime for GFP in several host materials. It can be seen that the excited state lifetime for GFP in both the aqueous solution and in the polyacrylamide film host is very close to those measured in other host materials. Table 4.1 also indicates that it remains relatively unchanged when measured using two-photon excitation.

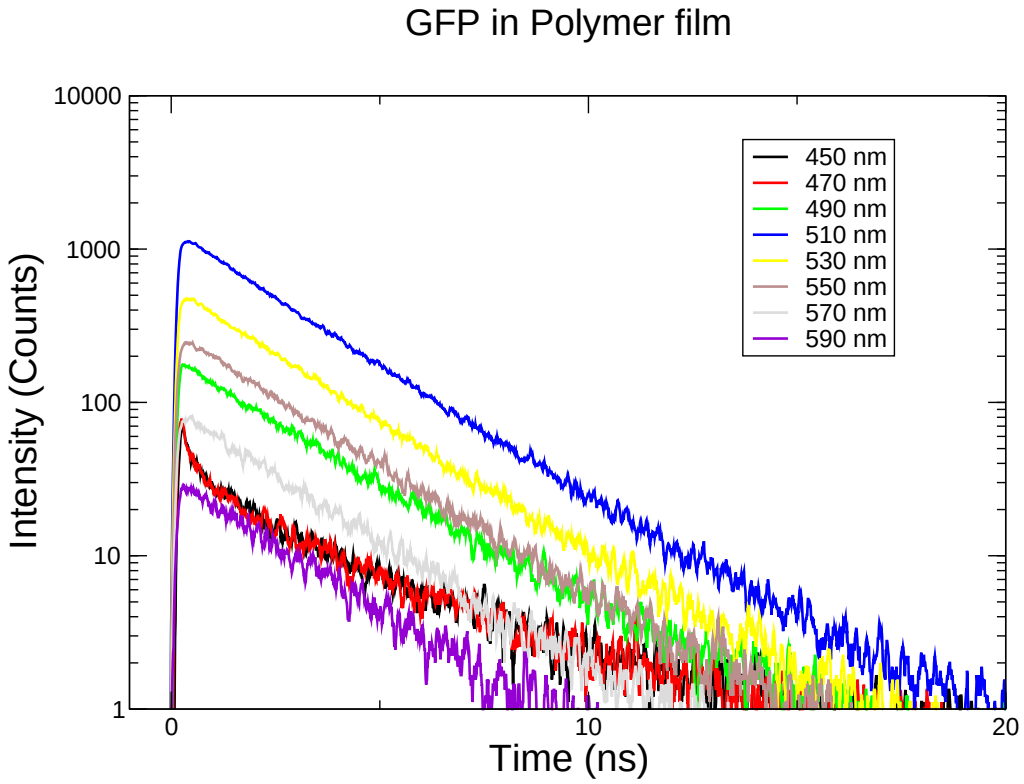

Figure 4.5: Plot showing the decay of the excited state lifetime decay of GFP in a polyacrylamide film. For emission that does not overlap into the excitation band, the extracted decay time is 2.7 ns.

4.3 Pressure Dependence of Emission Spectra

Both excitation and emission spectra can give significant insight into the state and environment of the chromophore. In particular, the excitation spectra show evidence of two species of GFP differentiated by the protonation of chromophore. By exploring the effects of hydrostatic pressure on the emission of GFP some information on how changes in the local environment can affect the behavior of the GFP chromophore can be obtained. Additionally semi-empirical quantum chemistry calculations, Zerner's intermediate neglect of differential overlap (ZINDO), was used to calculate the spectral shifts that occur as the chromophore is distorted and provide possible explanation of the spectral changes that occur at high pressure.

4.3.1 Experimental

Fig. 4.6 is a schematic diagram showing the experimental setup used to measure the emission spectra at high hydrostatic pressures. A reservoir containing hydraulic fluid was connected to the pressure apparatus using stainless steel hydraulic lines. Care was taken to ensure that the hydraulic fluid would not denature the protein structure. The fluid was then pumped through the entrance valve into the rest of the apparatus and purge the remaining air from all of the hydraulic lines through a bleeding valve. Upon closing the valves, the hydrostatic pressure of the system can be increased by compressing the cylinder in the pressure generator. The GFP sample was inserted into a glass tube that was in turn inserted into the sample chamber. Sapphire spheres were used as windows through which the protein could be both optically excited and the resulting fluorescence measured. The windows were placed perpendicular to each other to decrease the reflections within the sample chamber and were in line with the detector.

The GFP was excited using a light emitting diode (LED) which emits at 405 nm, *i.e.* close to the excitation peak of GFP to maximize the emission from the protein. The emission from the protein was collected using a fiber optic bundle which allowed the light to be matched

to the entry slits of a spectrometer. The emission spectrum was then collected using a CCD. The resulting spectrum was captured and displayed on a computer.

The emission spectra for GFP were measured for hydrostatic pressures between 0 psi and 60,000 psi in steps of 1000 psi. Although the GFP sample was secured in a glass tube within the sample chamber, currents in the hydraulic fluid and vibrations caused by the cranking of the pressure generator as the pressure was changed may have caused changes in the orientation of the polyacrylamide film within the sample chamber. These changes can cause a change in the overall fluorescence intensity and a distortion to the resulting spectra. To minimize these effects the pressure was brought to 60,000 psi, stepwise was released and the spectra were measured in decreasing order.

4.3.2 Results and Discussion

Fig. 4.7 shows the resulting emission spectra of GFP for a series of hydrostatic pressures. Although the overall emission changes little, the peak absorption spectrum shifts to lower wavelengths with increasing pressure. Fig. 4.8 shows maximum fluorescence peak as a function of the pressure. To extract a rate of change of the peak fluorescence as a function of pressure, the data was fit to a linear function (solid black line). For GFP, the peak wavelength shifts at a rate of -2.0×10^{-5} nm/psi. Since the characteristics of the spectrum remains similar under high pressure, the chromophore, which is positively charged due to protonation that occurs in a low pH solution, may experience an interaction with a nearby ions or the chromophore may experience a distortion as the pressure is increased.

As a comparison, the spectrum of DsRed was also measured at a series of pressures. DsRed is a fluorescent protein originally isolated from the *Discosoma* coral which has a similar structure to GFP but the chromophore undergoes further chemical modification which extends the conjugated π-electronic system of the chromophore which shifts the the emission to the red[14]. Fig. 4.9 shows the maximum wavelength as a function of the hydrostatic pressure. The overall rate of the shift of the fluorescence peak was determined to be $1.53 \times$

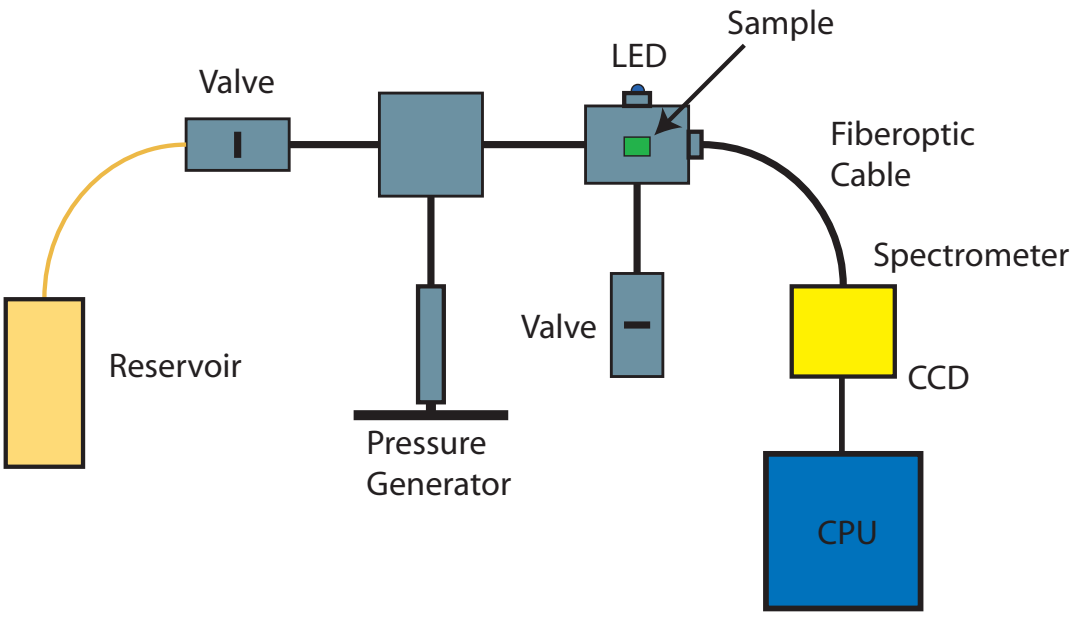

Figure 4.6: Schematic of the pressure apparatus used in the measurement of the emission spectra of GFP as at hydrostatic pressures varying from 0 psi to 60,000 psi.

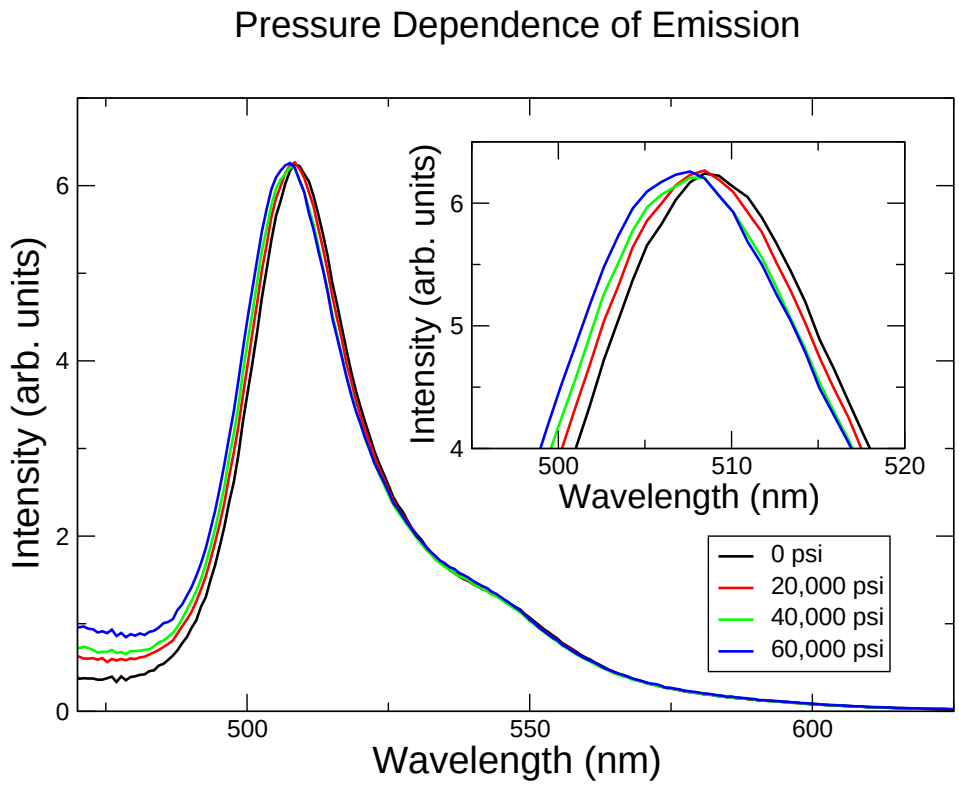

Figure 4.7: The resulting emission spectrum of GFP in the polyacrylamide film host as a function several pressures. The fluorescence peak blueshifts as a rate of -2.02×10^{-5} nm/psi.

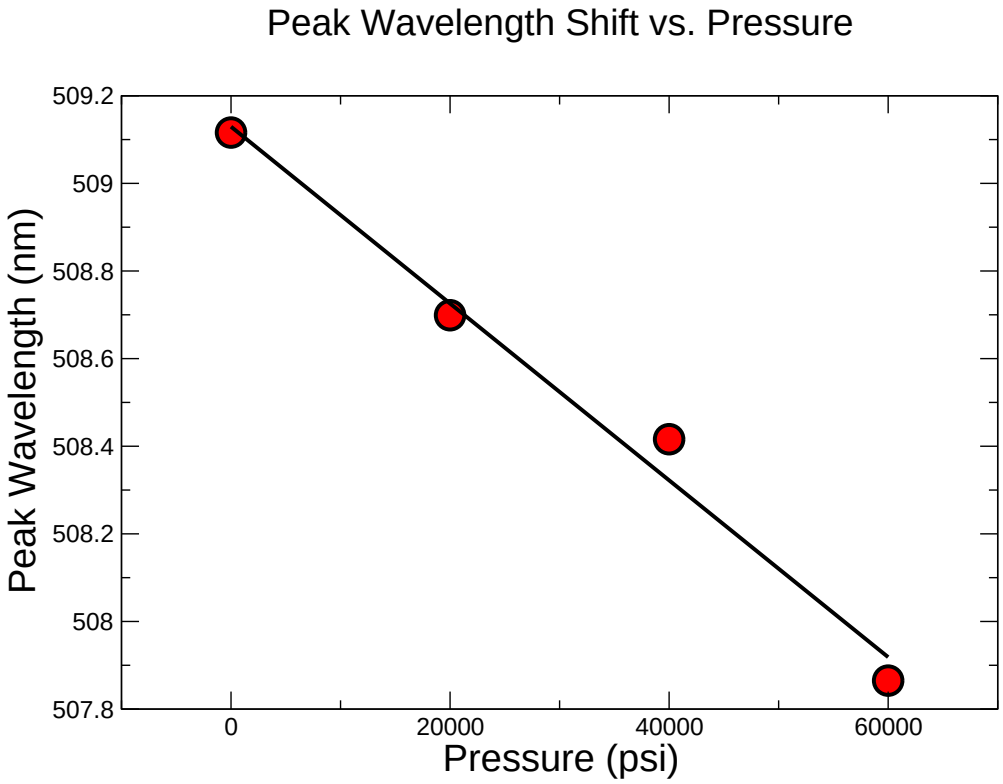

Figure 4.8: The measured shift in the peak wavelength of GFP as a function of the hydrostatic pressure (red dots). The solid line shows a linear fit of the experimental data. The peak wavelength changes as a rate of -2.02×10^{-5} nm/psi.

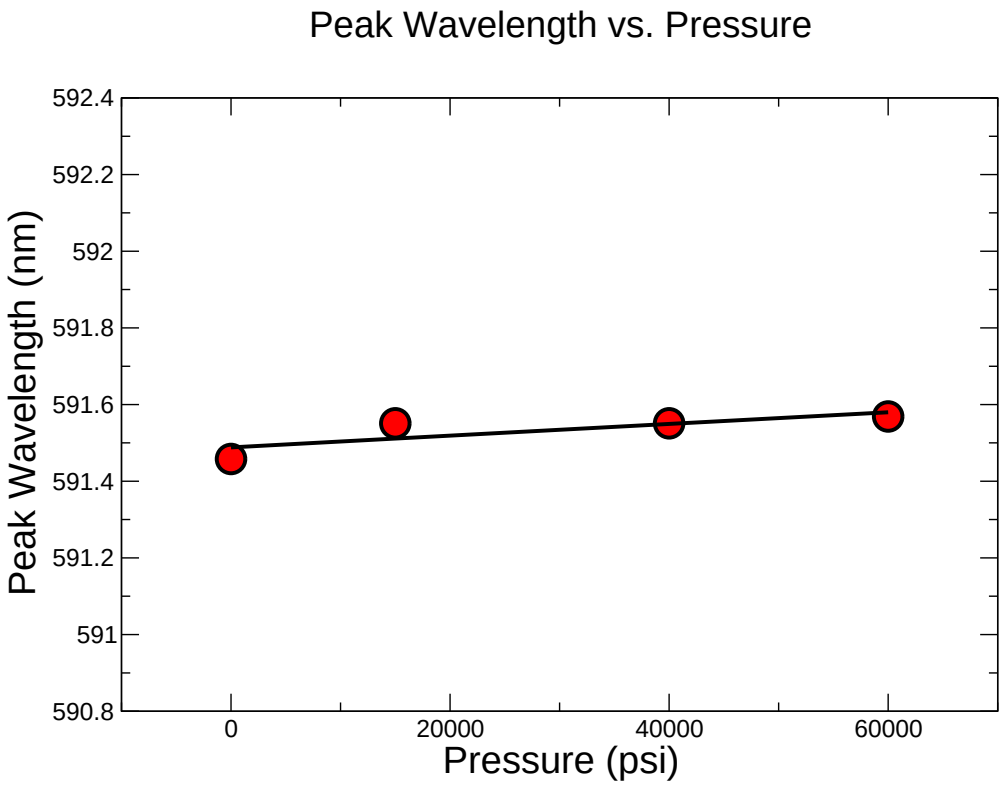

Figure 4.9: The measured shift in the peak emission wavelength of DsRed as a function of the hydrostatic pressure (red dots). The solid line shows a linear fit of the experimental data. The peak wavelength changes as a rate of 1.53×10^{-6} nm/psi.

10^{-6} nm/psi. This shift is an order of magnitude less than the shift rate measured in GFP and the shift is in the opposite direction. The magnitude of the shift in the GFP may therefore be related to the protonation of the chromophore. This behavior has been confirmed by Verkhusha *et al.* in 2003[15].

To determine possible mechanisms for the shifting of the fluorescence of GFP, quantum chemical calculations were used to explore the excitation energy of the GFP chromophore as a function of the angle between the two aromatic rings (α, See fig. 4.1). The values of the excitation energy were calculated using the semi-empirical ZINDO techniques within

Gaussian 98[16]. Initially, the GFP chromophore was allowed to relax to an angle of 130^o, and the excitation energy was calculated. The angle α was then varied and the excitation was calculated again. Fig. 4.10 shows the resulting excitation energy as a function of the angle α. To obtain a rate of of the excitation peak as a function of α, a line was fit to the calculated wavelengths. The rate of change of the excitation wavelength as a function of α is $\approx -1.1\,\mathrm{nm/degree}$. It can be seen as α increases the excitation energy blue shifts; this is similar to the resulting emissions measured as the pressure increases. If this is a possible mechanism that may account for the changes in the wavelength of emission of GFP at high hydrostatic pressures, the changes to the angle of the chromophore varies only slightly to account for the small rate of change of the emission. For more complete study of the effects of pressure on the spectral properties it will be necessary to measure the excitation spectra of GFP and DsRed as a function of pressure. It will also be necessary to model the distortions of the chromophore at high pressure using molecular dynamic simulations. ZINDO can be used to calculate the change in the excitation of the distorted chromophore. These additional calculations are beyond the scope of this dissertation.

4.4 Determination of the Nonlinear Absorption Cross-section σ_2

GFP has been observed to exhibit an extremely high two-photon absorption (TPA) cross-section. This suggests that it may be possible to find a wide range of nonlinear optical applications in addition to its use as a fluorescence probe. Recent measurements of the two-photon absorption cross-section in GFP indicate that this parameter saturates at high intensities. In this section, a comparatively low intensity measurement of the TPA absorption using 10 ns pulses is described.

The magnitude of the nonlinear susceptibility is the source of nonlinear optical properties of the materials. Measurements of the nonlinear third-order susceptibility, $\chi^{(3)}$, have traditionally been made using four-wave mixing or other multi-beam experiments. These experiments can be quite challenging making the results difficult to interpret. Van Stryland

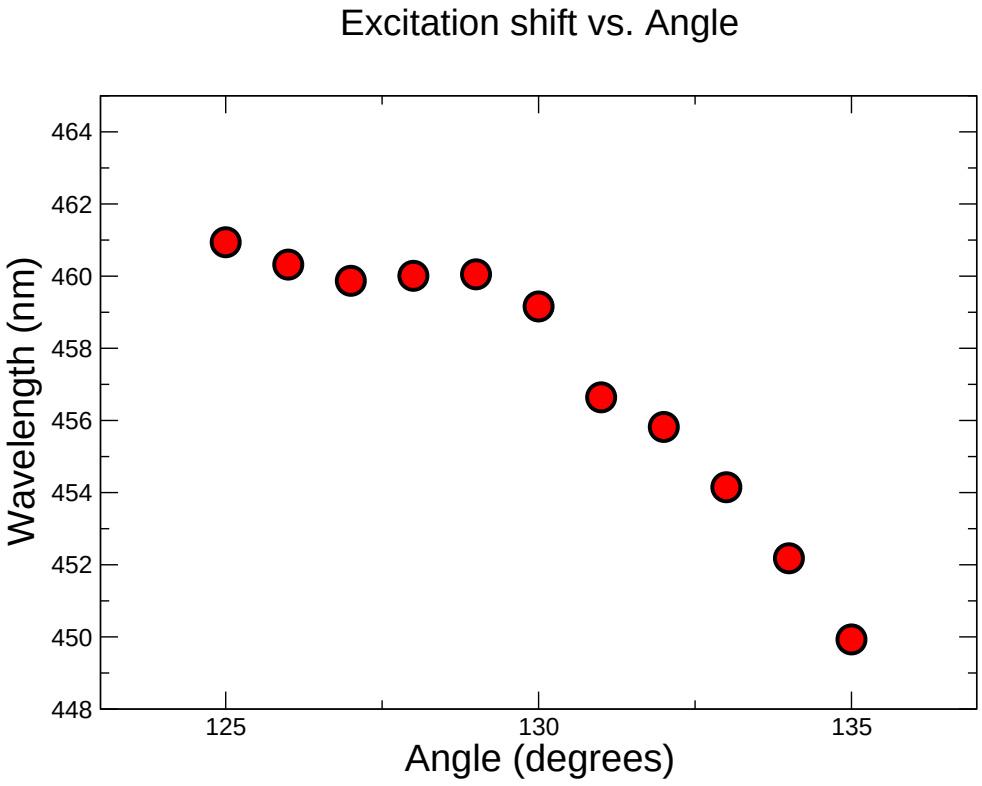

Figure 4.10: The calculated wavelength of in the peak excitation of the GFP chromophore as a function of the angle α (See fig. 4.1). The rate of change of the excitation wavelength is $\approx$-1.1 nm/degree.

et al.[17] developed a technique allowing for the measurement of both the real and imaginary part of the $\chi^{(3)}$ using a single beam experiment commonly known as Z-scan. The Z-scan method is commonly used in two configurations, closed and open aperture. Open aperture Z-scan is used to measure both the magnitude and the sign of the real part of $\chi^{(3)}$ which is directly associated to the nonlinear index of refraction. By removing the aperture, open aperture Z-scan measures the magnitude of the imaginary part of $\chi^{(3)}$. The imaginary part of $\chi^{(3)}$ is associated with the nonlinear absorption coefficient of in the nonlinear material. The magnitude of the intensity dependent absorption coefficient can then be used to calculate the two-photon absorption cross-section, σ_2.

4.4.1 Z-scan Experiment

The open aperture Z-scan follows the experimental setup illustrated in fig. 4.11. The excitation source was a home built dye laser, which used a a flowing dye cell containing a 4.80×10^{-4} M solution of Excition LDS 798 laser dye in a methanol solution. To obtain a broad band source no tuning elements were used to limit the bandwidth and the dye laser cavity was constructed using only two mirrors and the dye cell. The dye laser produced a broadband 7 ns pulse, at 794 nm with a bandwidth of 12 nm. The particular spectral characteristics were chosen to closely resemble the wavelength and bandwidth of an ultrafast Ti:Sapphire laser system. The pump source was a frequency doubled Nd:YAG laser which generated 10 ns pulses at 532 nm with a repetition rate of 10 Hz. The pump pulse was focused into the dye cell using a cylindrical lens. The laser pulse was then apertured to control the profile of the beam.

A pick-off beam splitter was used to send a small fraction of the laser pulse into an EOT ET-2040 Silicon PIN large area photo-detector which has an active area of 20 mm^2. This fraction of the pulse acts as a trigger for the system and allows the intensity of the pump pulse to be monitored. The remaining pulse was then focused using a 15 cm lens to focus the beam along the Z-axis. The sample GFP embedded in a polyacrylamide film discussed on

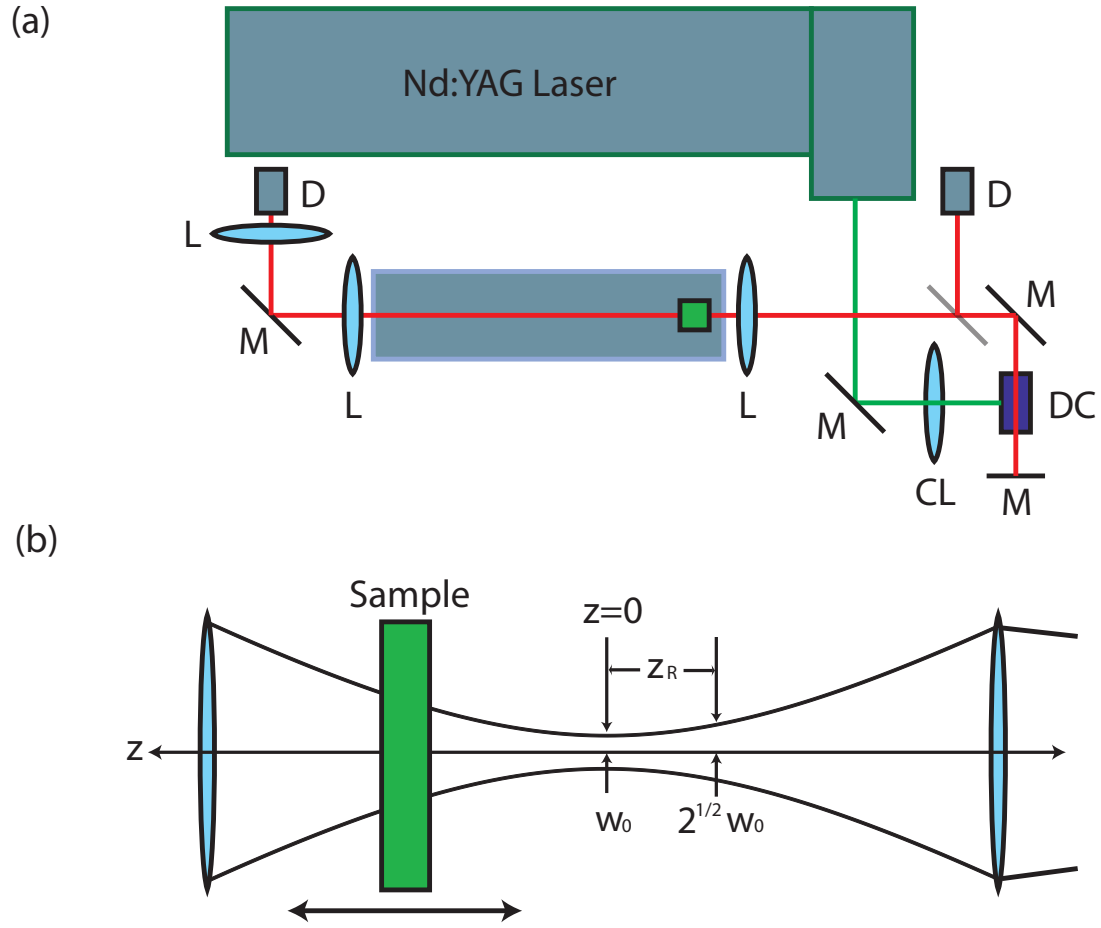

Figure 4.11: (a) A schematic showing the experimental setup for open aperture Z-scan measurements, where M corresponds to a mirror, CL to the cylindrical lens DC to a flowing dye laser cell and D to the photo-detectors. (b) A close up illustration of a typical open aperture Z-Scan experiment where w_0 is the beam waist, z_R is the Rayleigh range and the sample, GFP embedded in a polyacrylamide film, mounted on a 60 cm translation stage.

section 4.1 was translated along the focused beam on a translation stage (Compumotor S57 digital stepping motor, SX drive/indexer, RP240 interface, and a Daedal 60 cm translation stage). The sample was translated a total distance of 35.4 cm. The transmittance through the sample was then focused onto another ET-2040 Silicon PIN photo-detector. The signal from each of the detectors was captured and averaged using a Tektronix (TDS 3052) digitizing oscilloscope. Control of the translation stage and data acquisition was handled using a computer and interface/control programs written using the C programing language.

4.4.2 Results and Discussion

Open aperture Z-scan measurements were performed on GFP embedded in a polyacrylamide. Fig. 4.12 shows the normalized transmittance obtained using a wavelength of 794 nm. The model used in the analysis of the normalized transmittance measured as a function of distance by Z-scan follows the treatment of Van Stryland *et al.*[17] A detailed discussion of the calculation can be found in appendix F. The calculated normalized transmittance was fit to the experimental data using a Levenberg-Marquardt nonlinear least squares fitting routine. A value of 0.03 cm/GW was extracted for the nonlinear absorption constant. The concentration of the protein in the polyacrylamide was 0.98 μM. Using these values in equation F.24 yields a value of 7.64×10^{-44} G-M for σ_2. Table 4.5.2 shows results of the measurement of the two-photon absorption cross-section for several materials. The value of σ_2 for GFP in embedded in a polyacrylamide film is on the same order of magnitude as other (unsaturated) measurements of GFP in an aqueous solution. Table 4.5.2 also shows the measured two-photon absorption cross-section for rhodamine 610 which is a common laser dye considered to have a high reasonably two-photon absorption cross-section. It can be seen that the measured values of σ_2 for GFP are significantly higher than those measured in Rhodamine 610. Indeed, the two-photon absorption cross-sections measured in GFP are significantly larger than designer TPA molecules such as the optical power limiting molecule synthesized by Spangler *et al.*[18]

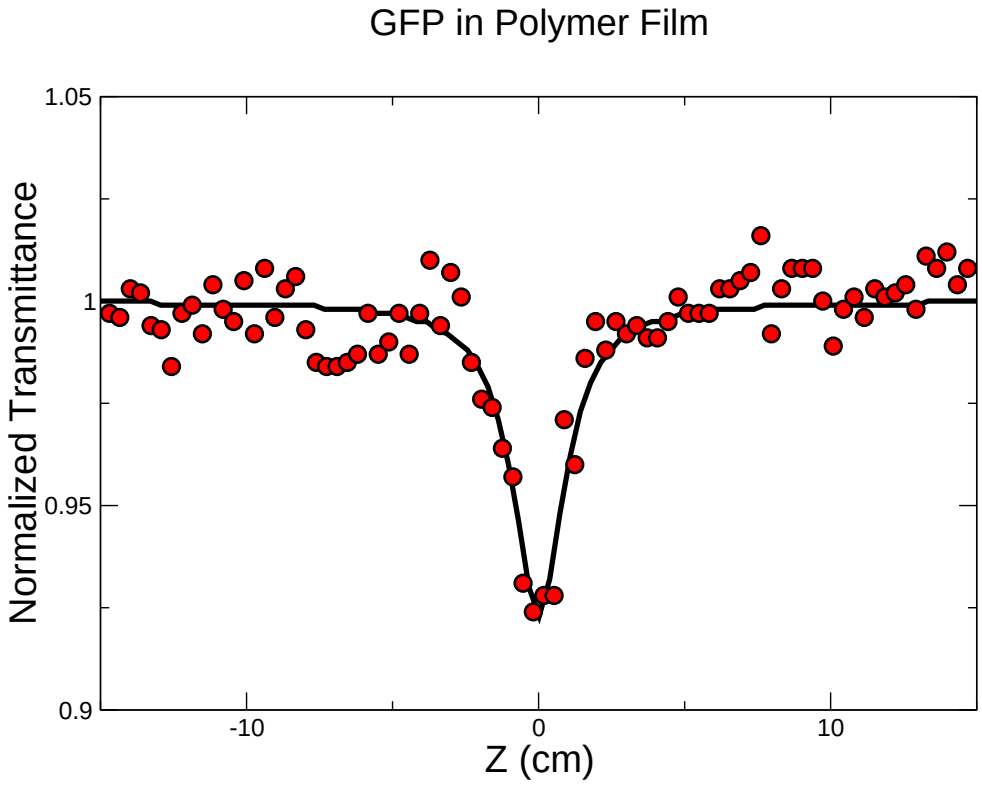

Figure 4.12: The normalized transmittance from Z-scan experiment (red dots) using $\lambda = 794\,\text{nm}$ light in GFP embedded in a polyacrylamide film, and the best fit Z-scan curve which corresponds to a $\sigma_2 = 7.64 \times 10^{-44}$ G-M.

In order to explore the role of the GFP chromophore in the TPA process, the TPA cross-section was calculated for the chromophore in the absence of the protein backbone. A calculation of the two-photon absorption cross-section requires the sum over states calculation. This technique is a direct implementation of the formula first derived by Göppert-Mayer[19]

$$\sigma_2 = \frac{\omega^2}{4n^2c^2\epsilon_0^2}\mathrm{Im}\left[\frac{1}{\Omega_{fg} - i\Gamma_{fg} - 2\omega} \cdot \overline{\alpha_{fg}(\omega,\omega)^* \alpha_{fg}(\omega,\omega)}\right], \tag{4.1}$$

where ω is the frequency of the incident light, Ω_{fg} is the frequency difference associated with the $g \rightarrow f$ transition, $\Gamma_{fg} = T_2^{-1}$ is the homogeneous linewidth and T_2 is the dephasing time. The first order transition polarizability, $\alpha_{fg}(\omega,\omega)$, is a second rank tensor and is given by

$$\alpha_{fg}(\omega,\omega) = \frac{e^2}{\hbar}\sum_i \left[\frac{\langle f|\mathbf{e}_1 \cdot \mathbf{r}|i\rangle\langle i|\mathbf{e}_2 \cdot \mathbf{r}|g\rangle}{\Omega_{ig} - \omega} + \frac{\langle f|\mathbf{e}_2 \cdot \mathbf{r}|i\rangle\langle i|\mathbf{e}_1 \cdot \mathbf{r}|g\rangle}{\Omega_{ig} - \omega}\right]. \tag{4.2}$$

The matrix elements that are required to solve for the transition polarizability equation 4.1 can be evaluated using quantum chemical calculations. Unfortunately due to the complicated interactions between GFP and its environment it is not possible to calculate the dephasing time. The dephasing time must be measured experimentally. Degenerate four-wave mixing in the forward two pulse geometry was used to obtain an estimate of the dephasing time of GFP in the polyacrylamide host.

4.5 Estimation of the Electronic Dephasing Time $T_2 = \Gamma_{fg}^{-1}$

The investigation of the two-photon absorption cross-section yielded results that were significantly larger than those of other organic molecules that have similar structures to the chromophore of GFP. In order to calculate the two-photon absorption cross-section using the sum over states algorithm, it is necessary to have a value of $T_2 = \Gamma_{fg}^{-1}$. To measure the optical dephasing time of GFP, degenerate four-wave (DFWM) mixing in the forward two pulse geometry was used.

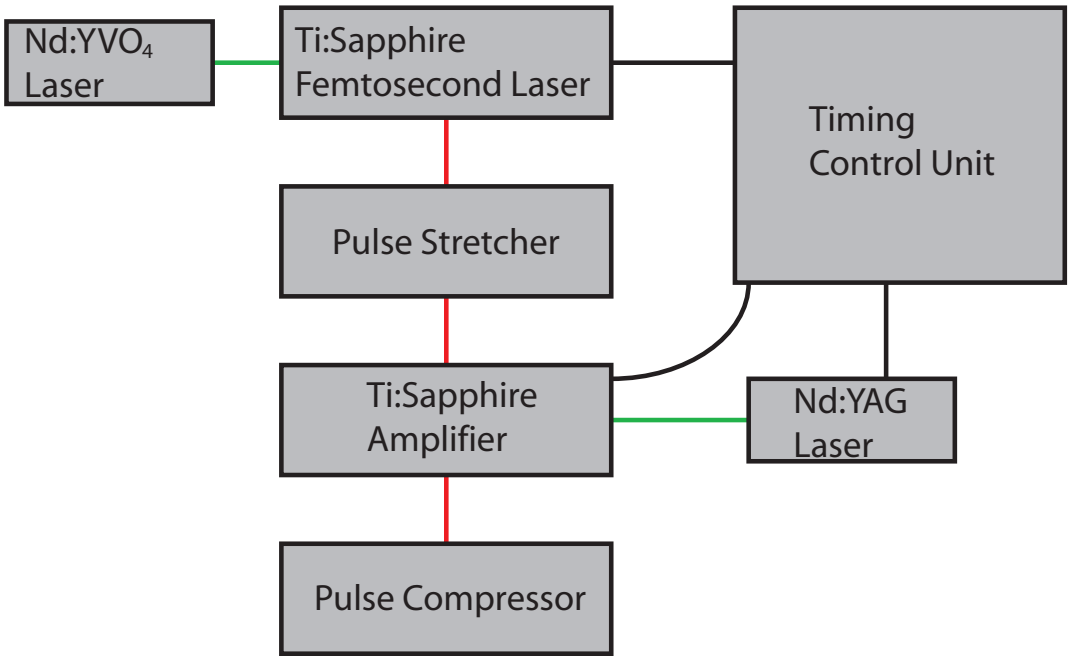

Figure 4.13: Diagram showing the major components required to produce an amplified Ti:Sapphire pulse.

4.5.1 Experimental Setup

Degenerate four-wave mixing in the two-pulse forward geometry was performed using the emission from an amplified Ti:Sapphire laser system. Fig. 4.13 shows a schematic diagram of the amplified Ti:Sapphire femtosecond pulse used in these experiments. The seed pulse is produced by a mode-locked Coherent Inc. Mira Ti:Sapphire laser pumped by a Coherent Inc. intra-cavity, frequency doubled Verdi V5 Nd:YVO_4 laser which produces a 5W frequency doubled CW beam which was frequency doubled to 532 nm. The seed pulse train is a near Fourier transform limited pulse with a pulse width of 110 fs as measured by autocorrelation assuming hyperbolic secant squared pulses, and a bandwidth of 8 nm with a central wavelength of 800 nm of a repetition rate of 76 MHz.

To prevent optical damage to the amplifier system due to high intensity pulses that exists in the amplifier cavity, the seed pulses must be stretched. The stretching takes place in the in the first major component of the Coherent Inc. Legend regenerative amplifier. The seed pulse is spread spectrally using a diffraction grating. The spectrally spread pulse is then re-collimated and allowed to propagate to a large area high reflector and retroreflected and refocused on the grating. This process is repeated and allows the laser pulse to be stretched to the order of 200 ps. With the increased pulse width, the intensity of pulse as it is being amplified will be below the damage threshold of the optics within the amplifier cavity.

The amplifier is pumped using a Coherent Inc. Evolution-30 DPSS frequency doubled Q-switched Nd:YLF laser system that emits a wavelength of 527 nm, at a repetition rate of up to 1 kHz, with a typical pulse energy of 20 mJ and a pulse width of 200 ns. To efficiently amplify the pulses, the stretched seed pulses must be injected into the amplification cavity after the pump pulse has excited the Ti:Sapphire amplification rod. The timing of the synchronization of the pump pulse from the Evolution-30 and the Mira 900 is governed by a frequency divider in the control unit (Coherent Inc. SDG). The pulses are also synchronized to two Q-switches which are used to both inject the seed pulse into the amplifier and extract the amplified pulse from the cavity. The delays between the Q-switches were individually controlled and

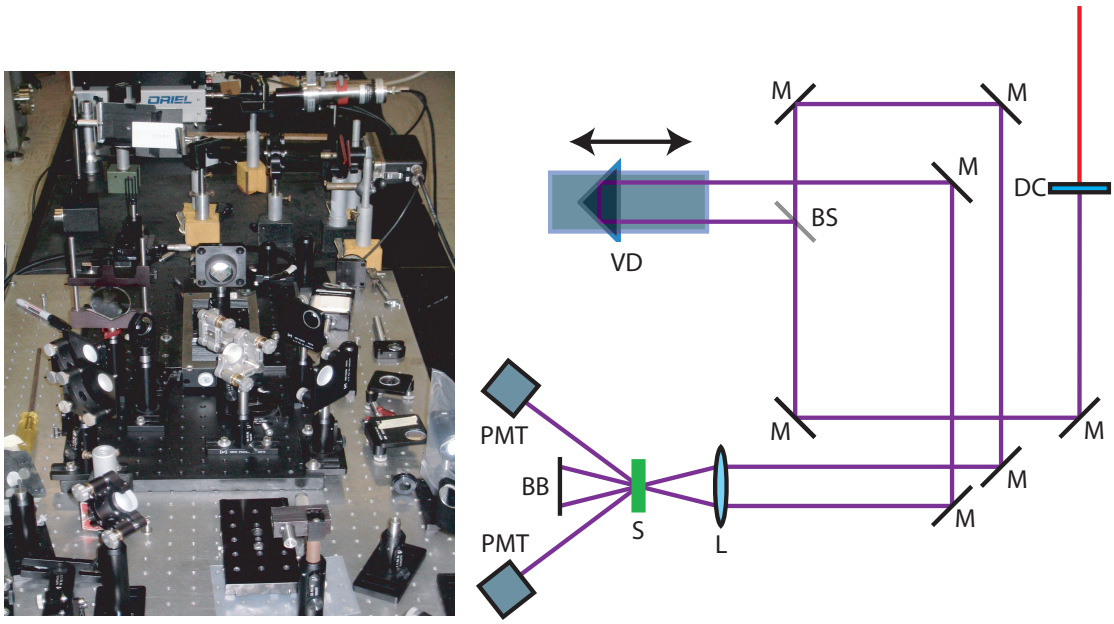

Figure 4.14: A schematic of the forward two pulse degenerate four-wave mixing setup used in this work. Photograph of the experimental setup.

the pulse train within the amplifier was monitored using a photodiode outside of one of the amplifier cavity mirrors to optimize the delays of both the injection and the extraction of the amplified pulse. After the amplified pulse is maximized, the pulse is extracted from the amplifier cavity and compressed. If the bandwidth of the amplified pulse has not been clipped in the amplification process, the amplified pulse should be able to be compressed to the original pulse width of the seed pulse. The final pulse energy of the 110 fs optical pulses was measured to be 2.5 mJ centered at 800 nm with a repetition rate of 1 kHz.

The intensity of the amplified pulses was attenuated to a pulse energy of 750 μJ to prevent optical damage to both the optics used in the DFWM experiment and the sample. The femtosecond pulses were then frequency doubled to a central frequency of 400 nm and a pulse energy of 250 μJ. To prevent the build up of excess heat in the DFWM measurements and to prevent multi-pulse effects such as photo-bleaching and heat damage, the repetition

rate of the amplified pulses was decreased to ≈10 Hz. The experimental setup used for these DFWM measurements were completed using an experimental setup that was modified from an existing frequency resolved optical gating (FROG) apparatus. This experimental setup allowed the measurement of DFWM signals using a compact experimental apparatus that was easily transportable between experiment locations. Fig. 4.14 shows a schematic of the experimental setup used in these measurements, and the inset in fig. 4.14 is a photograph of showing the apparatus used for these measurements. The experimental principles are similar to those discussed in chapter 2. The excitation pulse is split by division of amplitude into two equal intensity pulses using a 50/50 beamsplitter. Each pulse was then propagated along two independent, adjustable length beam paths. The beam paths are adjusted using retro-reflectors mounted Newport UMT100pp.1 translation stages controlled using an Newport ESP300 motion controller. The translation stages have a resolution of 100 nm. The two pulses were focused into the sample (with directions $\vec{k}_1$ and $\vec{k}_2$) using a single 80 cm focal length lens. The DFWM signal pulse trains in both the $2\vec{k}_1 - \vec{k}_2$ and the $2\vec{k}_2 - \vec{k}_1$ directions were detected using a photomultiplier tube (Oriel 77341) and compared with a control beam which was used both to trigger and to monitor the fluctuation in the intensity of the excitation pulse. Both the reference pulse and the DFWM signals were captured and averaged using a Tektronix (TDS 3052) digitizing oscilloscope. The resulting signal intensities were then recorded for analysis using a computer.

4.5.2 Results and Discussion

It was not possible to perform DFWM measurements of GFP in an aqueous solution, since heating effects caused vaporization of the sample. Due to the small quantities of GFP available it was not possible to use either a flowing dye cell or jet configuration. Instead the measurements were performed using the GFP/polyacrylamide gel sample. Fig. 4.15 shows the normalized DFWM signal intensities in both the $2\vec{k}_1 - \vec{k}_2$ and $2\vec{k}_2 - \vec{k}_1$ directions for a sample of GFP embedded in a polyacrylamide film as a function of the delay time between

pulse $\vec{k}_1$ and $\vec{k}_2$. The solid black circles correspond to the experimental $2\vec{k}_1 - \vec{k}_2$ signal, and the solid red circles correspond to the experimental $2\vec{k}_2 - \vec{k}_1$ signal.

A background measurement was performed as shown in Fig. 4.16. Unfortunately with experimental error it was not possible to distinguish between the two signals; thus, indicating the DFWM signals were dominated by the polymer host. The signal originating from the transparent host was substantiated by the absence of a peak shift between the $2\vec{k}_1 - \vec{k}_2$ and $2\vec{k}_2 - \vec{k}_1$ signals as observed in chapter 2. Instead, the signals resemble a third-order autocorrelation as might be expected from an instantaneous non-resonant nonlinearity. The third-order autocorrelation function

$$G^{(3)}(\tau) = \frac{\langle I(t)^2 I(t-\tau)\rangle}{\langle I(t)^3\rangle} \tag{4.3}$$

was fit to the experimental data and an mean input pulse width of $\tau_{\mathrm{FWHM}} = 123 \pm 9\,\mathrm{fs}$ was extracted. This is consistent with the pulsewidth of the unamplified pulse as measured by second-order autocorrelation.

Due to the experimental conditions described above, a measurement of T_2 for GFP is beyond the scope of this dissertation. Since the dephasing time is both temperature and material specific, the choice of the excitation wavelength, host material are important. The major concern for the measurement of the dephasing time in GFP embedded in the polyacrylamide film host is that in order for the polyacrylamide to produce DFWM signals that have been measured its $\chi^{(3)}$ must be significant at a wavelength of 400 nm. To facilitate the measurement of the dephasing time of GFP it will be necessary to choose a host in which the magnitude of $\chi^{(3)}$ is small. GFP presents many problems of its own which make measuring the dephasing difficult; in particular, many of the solvents or materials which may have small susceptibilities may also denature the fragile protein structure, this eliminates most alcohol solvents. Other potential difficulties include the limited lifetime of GFP before it denatures and the limited production of high quality purified GFP.

It is still of interest to estimate the two-photon absorption cross-section for the GFP chromophore by using a value $T_2 = \Gamma_{fg}^{-1}$ from a similar molecule since it may yield a reasonable

Table 4.2: Oscillator strengths and two-photon absorption cross-section for GFP, GFP chromophore, Rhodamine 610 and an optical power limiting molecule synthesized by Spangler *et al.*[18]

Sample	σ_2 $(\frac{10^{-50}\,\mathrm{cm}^4\cdot\mathrm{s}}{\mathrm{photon}\cdot\mathrm{molecule}})$
GFP (Z-scan)	7.6×10^6
GFP (Z-scan)	6×10^5 [8]
GFP (Calc.) chromophore	1.43
Rhodamine	410 [20]
Spangler *et al.*[18]	6.6×10^4

value. The dephasing time of photoactive Yellow Protein has been reported to be 15 fs. σ_2 was using this value in equation 4.1 and matrix elements calculated using the configuration interaction singles (CIS) method in Gaussian 98[21]. The calculated σ_2 was determined to be $1.5 \times 10^{-50} \frac{\mathrm{cm}^4\mathrm{s}}{\mathrm{photon-molecule}}$. Table 4.5.2 shows several measured and calculated two-photon absorption cross-sections. The estimated value of the two-photon absorption cross-sections for the GFP chromophore is six orders of magnitude smaller than that measured in GFP. The 10^6 discrepancy between the two-photon absorption cross-sections measured in GFP and those calculated using the chromophore cannot simply be attributed to poor estimate of T_2. One must conclude that the chromophore itself is not solely responsible for the large two-photon absorption cross-section. Future work on GFP to resolve the discrepancies between the calculated and measured values of σ_2 will require modeling not only the GFP chromophore, but also a significant portion of the protein backbone.

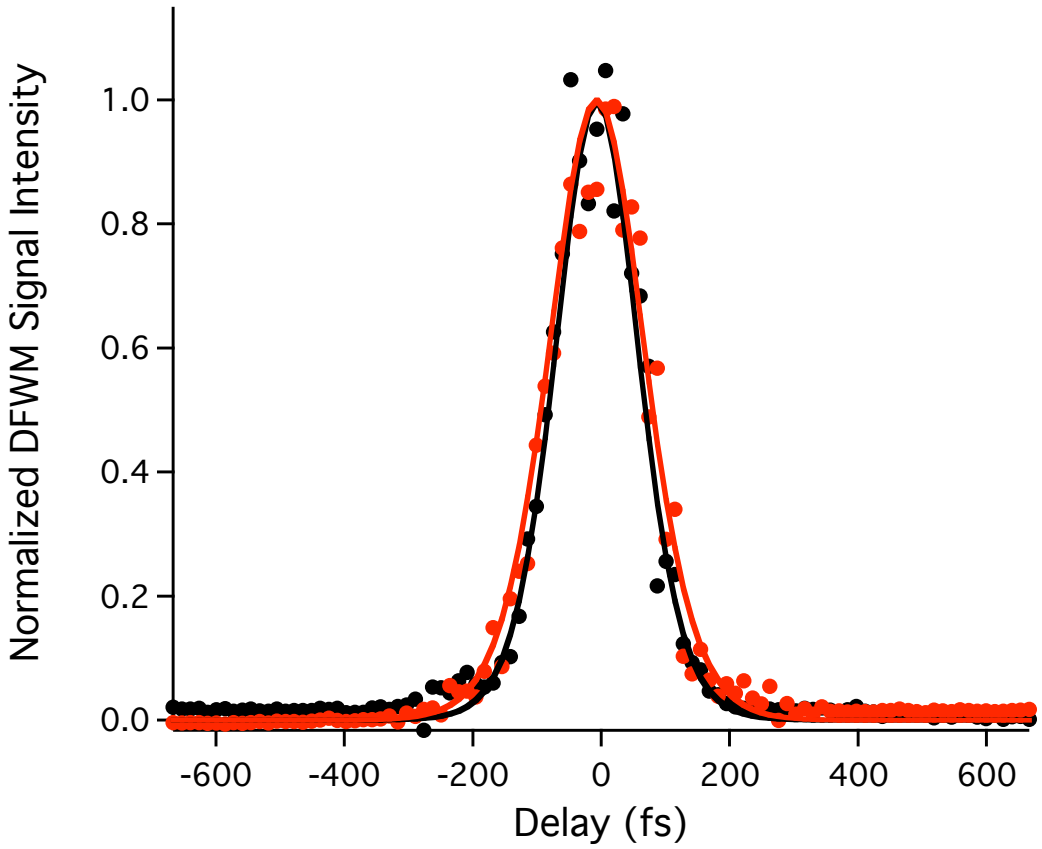

Figure 4.15: The normalized DFWM signal intensities GFP embedded in a polyacrylamide film in both the $2\vec{k}_1 - \vec{k}_2$ (black) and $2\vec{k}_2 - \vec{k}_1$ (red) directions. The dots refer to the experimentally measured data and the solid lines correspond to a third-order autocorrelation function. See equation 4.3.

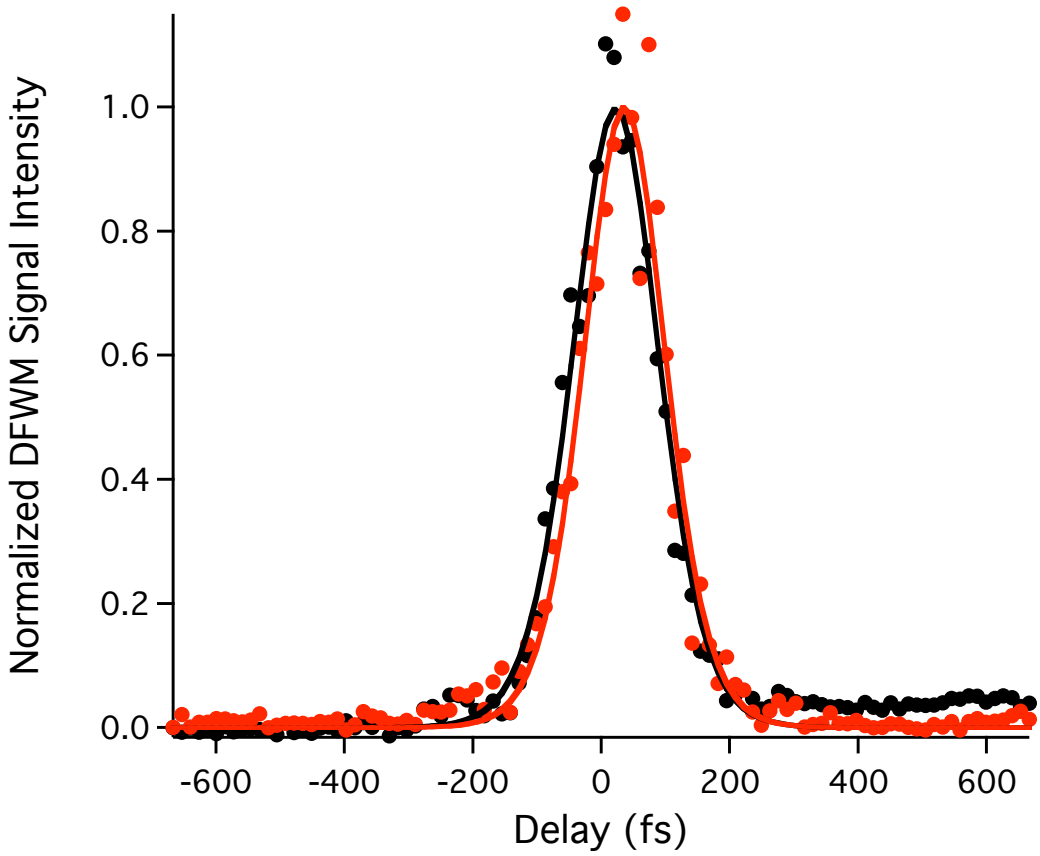

Figure 4.16: The normalized DFWM signal intensities in the polyacrylamide film which was used as a substrate for the GFP in both the $2\vec{k}_1 - \vec{k}_2$ (black) and $2\vec{k}_2 - \vec{k}_1$ (red) directions. The dots refer to the experimentally measured data and the solid lines correspond to a third-order autocorrelation function. See equation 4.3.

4.6 Conclusions

This chapter has described the application of several linear and nonlinear optical spectroscopies to GFP. In section 4.2, the excited state lifetimes of GFP were measured in both solution and the polyacrylamide film hosts. The excited state lifetime for GFP in solution was measured to be 3.4 ns while in the polyacrylamide film the excited state lifetime was measured to be 2.7 ns. These results were similar to those measured in GFP in other hosts. To explore the interaction between the chromophore and environment, the emission spectrum was measured for both GFP and a similar fluorescent protein DsRed. The peak fluorescence of GFP blue-shifted as the pressure was increased, while the peak fluorescence of DsRed remained fairly constant or slightly red-shifted as the pressure increased. These studies may eventually aid in the development of customized fluorescent proteins.

To explore the high two-photon absorption cross-section of GFP, Z-scan was used to obtain a value of the two-photon absorption cross-section for GFP in the polyacrylamide film on the nanosecond time scale. The resulting measurements were consistent with the two-photon absorption cross-sections measured in literature. In an effort to gain an understanding of the dynamical processes of GFP, degenerate four-wave mixing was attempted to measure the dephasing time. More over, it was not possible to extract the dephasing time of the GFP from the DFWM signals. In future studies, it may be possible to measure the dephasing characteristics for GFP with a judicious choice of the host for the protein and excitation wavelengths. It may also be necessary to use a dye jet to reduce the effects of photobleaching. Using dephasing times measured in other fluorescent proteins, a calculated value of the two-photon absorption cross-section was obtained for the GFP chromophore in the absence of the protein backbone. The calculated value of the two-photon absorption was significantly smaller than the experimentally measured value, leading to the conclusion that the chromophore is not solely responsible for the large cross-section but rather it is also a consequence of the protein backbone.

4.7 References

[1] O. Shimomura, F. H. Johnson, Y. Siaga, "Extraction, purification and properties of aequorin, a bioluminescent protein from the luminous *hydromedusan Aequorea*," J. Cell. Comp. Physiol. **59**, 223-239 (1962).

[2] H. Morise and O. Shimomura and F. H. Johnson and J. Winant, "Intermolecular energy transfer in bioluminescent system *Aequorea*," biochemistry **13**, 2656-2662 (1974).

[3] R. Y. Tsien, "The Green Fluorescent Protein," Annu. Rev. Biochem. **67**, 509-544 (1998).

[4] M. Chalfie, Y. Tu, G. Euskirchen, W. W. Ward, D. C Prasher, "Green fluorescent protein as a maker for gene expression," Science **263**, 802-805 (1994).

[5] D. J. Pikas, S. M. Kirkpatrick, E. Tewksbury, L. L. Brott, R. R. Naik, M. O. Stone, W. M. Dennis, J. Phys. Chem. B **106**, 4831-4837 (2002).

[6] S. T. Hess, A. A. Heikal, W. W. Webb, "Fluorescence Photoconversion Kinetics in Novel Green Fluorescent Protein pH Sensors (pHluorins)," J. Phys. Chem. B **108**, 10138-10148 (2004).

[7] R. A. G. Cinelli, V. Tozzini. V. Pellegrini, F. Beltram, G. Cerullo, M. Zavelani-Rossi, S. De Silvestri, M. Tyagi, M. Giacca, "Coherent Dynamics of Photoexcited Green Fluorescent Proteins," Phys. Rev. Lett. **86**, 3439-3442 (2001).

[8] S. M. Kirkpatrick, R. R. Naik, M. O. Stone, "Nonlinear Saturation and Determination of the Two-Photon Absorption Cross-section of Green Fluorescent Protein," J. Phys. Chem. B **105**, 2867-2873 (2001).

[9] D. C. Prasher, Virginia K. Eckenrode, W. W. Ward, F. G. Prendergast, M. J. Cormier, "Primary structure of the Aequorea victoria green-fluorescent protein," Gene **111**, 229-233 (1992).

[10] See for example webpage showing commercially available fluorescent proteins: http://www.clontech.com/clontech/.

[11] D. V. O'Connor, D. Phillips, *Time-correlated Single Photon Counting*, Academic Press Inc. London, (1984).

[12] A. Volkmer, V. Subramaniam, D. J. S. Birch, T. M. Jovin, "One- and Two-Photon Excited Fluorescence Lifetimes and Anisotropy Decays of Green Fluorescent Proteins," Biophys. J. **78**, 1589-1598 (2000).

[13] U. K. Tirlapur, K. König, Targeted transfections by femtosecond laser, Nature **418**, 290-291 (2002).

[14] M. A. Wall, M. Socolich, R. Ranganathan, "The structural basis for red fluorescence in the tetrameric GFP homolog DsRed," Nat. Struct. Mol. Biol. **7**, 1133-1138 (2000).

[15] V. V. Verkhusha, A. E. Pozhitkov, S. A. Smirnov, J. W. Borst, A. van Hoek, N. L. Klyachko, A. V. Levashov , A. J .W . G. Visser, "Effect of high pressure and reversed micelles on the fluorescent proteins," Biochimica. et. Biophysica. Acta. **1622**, 192-195 (2003).

[16] Æ. Frisch, M. Frisch, *Gaussian 98 User's Refenence*, Gaussian Inc. Pittsburgh, (1999).

[17] M. Sheik-Bahae, A. A. Said, T-H Wei, D. Hagan, E. W. Van Stryland, "Sensitive measurement of optical nonlinearities using a simgle beam," J. Quantum. Electron. **26**, 760-769 (1990).

[18] C. W. Spangler, E. H. Elandaloussi, M. K. Casstevens, D. N. Kumar, J. F. Weibel, R, Burzynski, "Design and synthesis of new optical-power-limiting chromophores with enhanced two-photon absorption," Proc. SPIE **3798**, 117-122 (1999).

[19] M. Göppert-Mayer,"Elementary processes with two quantum jumps," Ann. Physik **9**, 273-294 (1931).

[20] C. M. Liebig, "The Nonlinear Spectroscopy of Organic Dyes and Proteins," Masters Thesis, The University of Georiga, USA, (2000).

[21] W. M. Dennis, "Linear and Nonlinear Optical Characterization of Fluorescent Proteins," Technical Management Concepts Inc. Final Report, (2002).

[22] R. L. Sutherland, *Handbook of Nonlinear Optics*, Marcel Dekker, Inc., 2nd ed. (2005).

Chapter 5

Conclusions

In this dissertation a combination of experimental and computational techniques were used to investigate the interaction of ultrashort optical pulses with several optical materials and systems. Degenerate four-wave mixing (DFWM) in the forward two pulse geometry was used to investigate optical dephasing in the organic mode-locking dye IR140. DFWM signals were simulated using a model based on the density matrix; these simulated signals were fit to the experimental data in order to extract a value of the dephasing time. The extracted dephasing time in IR140 was determined to be 50±5 fs, which is consistent with the dephasing measurements in other organic dyes.

Finite-difference time-domain simulations, which numerically solve Maxwell's for the electric and magnetic fields, were used to explore the changes in the reflectivity of three dielectric high reflecting interference filters: (i) a quarter-wave dielectric stack, (ii) continuous rugate filter, and (iii) a discrete rugate filter. At low intensities, the FDTD method was verified by comparison with the characteristic matrix method which allows for the exact calculation of the electric and magnetic fields at each material interface. There was excellent agreement between the analytic characteristic matrix method and the FDTD method at low intensities. At high intensities the FDTD method was used to calculate the reflectance of the dielectric filters with the inclusion of the nonlinear optical effects. Of the three filters studied, the quarter-wave dielectric stack and the continuous rugate filter showed very little change to the reflectance at high intensities. The discrete rugate, on the other hand, showed more dramatic changes at high intensities. The high reflectance peak of the discrete rugate filter narrowed, and there was significant distortions introduced in the reflected pulse envelope.

A combination of linear and nonlinear spectroscopic techniques were used to investigate the properties of green fluorescent protein. Time correlated single photon counting was used to measure the excited state lifetime for GFP in both an aqueous solution and embedded in a polyacrylamide film. In solution, the excited state lifetime of GFP was measured to be 3.4 ns, and in the polyacrylamide film it was measured to be 2.7 ns. These values were in good agreement with those measured in the literature and the results of semi-empirical quantum chemical calculations of the oscillator strength of the GFP chromophore. The effect of high hydrostatic pressure on the emission spectrum of GFP was investigated. The peak fluorescence of GFP was found to blue-shift as the pressure was increased indicating a distortion of the GFP chromophore.

Using the Z-scan technique with nanosecond pulses, the two-photon absorption cross-section was measured for GFP in the polyacrylamide film. The measured value of the σ_2 at a wavelength of 794 nm was 7.64×10^{-44} G-M. This value is comparable to the values of σ_2 measured using femtosecond optical pulses. Using DFWM in the forward two pulse geometry and amplified doubled Ti:Sapphire laser pulses centered at 400 nm, DFWM signals were measured for GFP in the polyacrylamide film. However, the presence of a strong DFWM signals from the polyacrylamide host prevented the measurement of T_2 in this system.

Appendix A

Characteristic Matrix Calculations

Electromagnetic wave interaction with multilayered thin-film structures have been discussed in depth in numerous texts[1]. The treatment discussed below will follow the discussion in the text by Macleod which calculates the transmittance and reflectance for electromagnetic wave interaction with multilayered thin film structures at oblique angles, but will be simplified to normal incidence for the calculations presented in this appendix[2]. Fig. A.1 shows an electromagnetic wave incident upon a simple multilayered structure consisting of one thin later and a thick substrate. At interface b, the tangential components of the electric and magnetic fields can be separated in the forward (+) and backward (-) propagating directions,

$$\begin{aligned} E_b &= E_{1b}^{+} + E_{1b}^{-} \\ H_b &= \eta_1 E_{1b}^{+} - \eta_1 E_{1b}^{-}, \end{aligned} \tag{A.1}$$

where η_1 the tilted optical admittance equals,

$$\eta_1 = \frac{y_1}{\cos\theta_1} = \frac{N_1 \mathcal{Y}}{\cos\theta_1} \tag{A.2}$$

where $y_1 = N_1\mathcal{Y}$ is the optical admittance of the material contained in layer 1, N_1 is the in complex index of refraction of material 1, $N_1 = n_1 + \mathrm{i}k_1$, where n_1 is the material index of refraction and k_1 is the extinction coefficient. $\mathcal{Y}$ is the optical admittance of free space and can be expressed

$$\mathcal{Y} = (\epsilon_0/\mu_0) = 2.6544 \times 10^{-3} s. \tag{A.3}$$

The forward and backward propagating electric and magnetic fields can be expressed in terms of the total fields at the interface.

$$E_{1b}^{+} = \tfrac{1}{2}(H_b/\eta_1 + E_b) \tag{A.4}$$

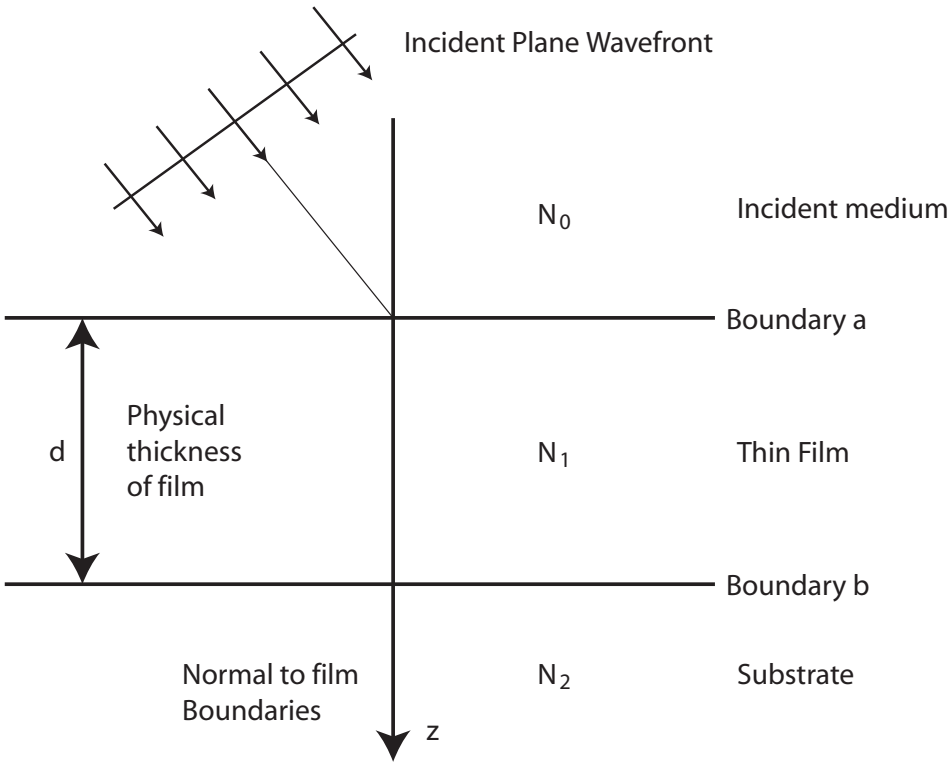

Figure A.1: Light incident upon a simple multilayered structure

$$E_{1b}^{-} = \tfrac{1}{2}(-H_b/\eta_1 + E_b) \tag{A.5}$$

$$H_{1b}^{+} = \tfrac{1}{2}(H_b + \eta_1 E_b) \tag{A.6}$$

$$H_{1b}^{-} = \tfrac{1}{2}(H_b - \eta_1 E_b). \tag{A.7}$$

The electric and magnetic fields at interface a at the same instant can be expressed in terms of the fields at interface b by introducing a phase factor caused by the delay that is due to the optical path the light travels within the layer,

$$\delta = 2\pi N_1 d_1 \cos\theta_1/\lambda, \tag{A.8}$$

where d_1 is the layer thickness and λ is the vacuum wavelength of the light. Then E and H at interface a can be expressed

$$E_{1a}^{+} = E_{1b}^{+}e^{(\mathrm{i}\delta)} = \frac{1}{2}(H_b/\eta_1 + E_b) \tag{A.9}$$

$$E_{1a}^{-} = E_{1b}^{+}e^{(\mathrm{i}\delta)} = \frac{1}{2}(-H_b/\eta_1 + E_b) \tag{A.10}$$

$$H_{1a}^{+} = E_{1b}^{+}e^{(\mathrm{i}\delta)} = \frac{1}{2}(H_b + \eta_1 E_b) \tag{A.11}$$

$$H_{1a}^{-} = E_{1b}^{+}e^{(\mathrm{i}\delta)} = \frac{1}{2}(H_b - \eta_1 E_b). \tag{A.12}$$

Rearranging the terms and solving for E_a and H_a,

$$\begin{aligned} E_a &= E_{1a}^{+} + E_{1a}^{-} \\ &= E_b\left(\frac{e^{\mathrm{i}\delta} + e^{-\mathrm{i}\delta}}{2}\right) + H_b\left(e^{\mathrm{i}\delta} - e^{-\mathrm{i}\delta}2\eta_1\right) \\ &= E_b\cos\delta + H_b\frac{\mathrm{i}\sin\delta}{\eta_1} \end{aligned} \tag{A.13}$$

$$\begin{aligned} H_a &= H_{1a}^{+} + H_{1a}^{-} \\ &= E_b\eta_1\left(\frac{e^{\mathrm{i}\delta} - e^{-\mathrm{i}\delta}}{2}\right) + H_b\left(e^{\mathrm{i}\delta} + e^{-\mathrm{i}\delta}2\eta_1\right) \\ &= E_b\mathrm{i}\eta_1\sin\delta + \mathrm{H_b}\cos\delta. \end{aligned} \tag{A.14}$$

By examination of equation A.13 and equation A.14 it can be seen that these system of equation can be using matrix notation

$$\begin{bmatrix} E_a \\ H_a \end{bmatrix} = \begin{bmatrix} \cos\delta & (\mathrm{i}\sin\delta)/\eta_1 \\ \mathrm{i}\eta_1\sin\delta & \cos\delta \end{bmatrix}\begin{bmatrix} E_b \\ H_b \end{bmatrix}. \tag{A.15}$$

This matrix expression for the tangential fields of E and H allows us to calculate the field amplitudes at the incident interface.

Once the electric and magnetic fields are obtained, the field reflectance coefficient can be calculated using

$$\rho = \frac{\eta_0 - Y}{\eta_0 + Y}. \tag{A.16}$$

The reflectance of the thin-film interface can then be calculated

$$R = \left(\frac{\eta_0 - Y}{\eta_0 + Y}\right)\left(\frac{\eta_0 - Y}{\eta_0 + Y}\right)^*, \tag{A.17}$$

where Y is the optical admittance of the assembly and is obtained from the calculated fields

$$Y = H_a/E_b. \tag{A.18}$$

To further simplify the expressions for the reflection coefficient and the reflectance, equation A.15 is normalized by dividing by the electric field at interface b yielding

$$\begin{bmatrix} E_a/E_b \\ H_a/E_a \end{bmatrix} = \begin{bmatrix} B \\ C \end{bmatrix} = \begin{bmatrix} \cos\delta & (\mathrm{i}\sin\delta)/\eta_1 \\ \mathrm{i}\eta_1\sin\delta & \cos\delta \end{bmatrix} \begin{bmatrix} 1 \\ \eta_2 \end{bmatrix}. \tag{A.19}$$

B and C are the normalized electric and magnetic fields the front interface and

$$\begin{bmatrix} B \\ C \end{bmatrix}, \tag{A.20}$$

is known as the characteristic matrix of the assembly. The characteristic matrix will be used for calculating the optical propertied of the thin-film. The optical admittance can then be expressed as

$$Y = \frac{H_a}{E_a} = \frac{C}{B} = \frac{\eta_2\cos\delta + \mathrm{i}\eta_1\sin\delta}{\cos\delta + \mathrm{i}(\eta_2/\eta_1)\sin\delta}. \tag{A.21}$$

From equation A.17 and equation A.21 the reflectance of the thin film assembly can be calculated.

The characteristic matrix can be adapted to an optical structure consisting of an assembly of dielectric thin-films as shown in fig. A.2. Consider a three layer structure with interfaces

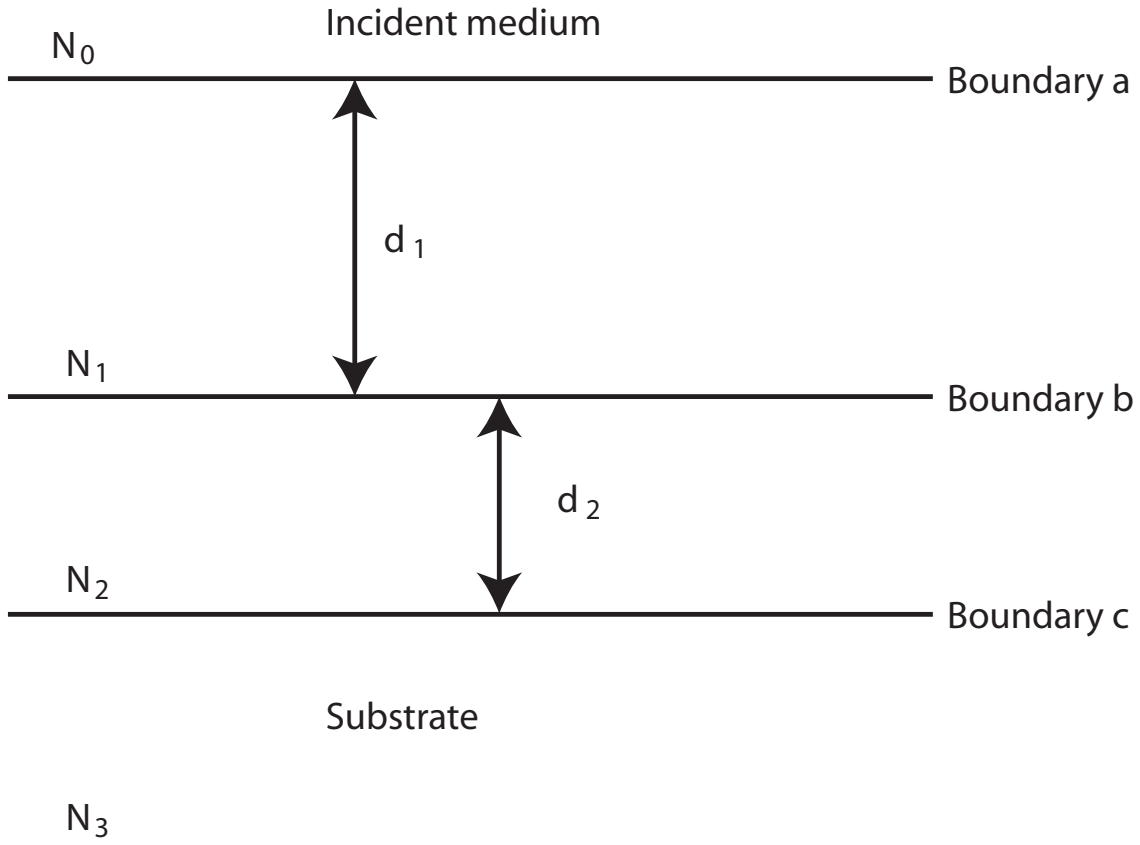

Figure A.2: Light incident upon a simple multilayered structure

a, b and c, applying the equation A.15 to the electric and magnetic fields at the interface, b can be calculated in terms of the electric fields at interface c

$$\begin{bmatrix} E_b \\ H_b \end{bmatrix} = \begin{bmatrix} \cos\delta_2 & (\mathrm{i}\sin\delta_2)/\eta_2 \\ \mathrm{i}\eta_2\sin\delta_2 & \cos\delta_2 \end{bmatrix} \begin{bmatrix} E_c \\ H_c \end{bmatrix}. \tag{A.22}$$

Equation A.22 can then be used to calculate the electric and magnetic fields at interface a by substituting into equation A.15

$$\begin{bmatrix} E_a \\ H_a \end{bmatrix} = \begin{bmatrix} \cos\delta_1 & (\mathrm{i}\sin\delta_1)/\eta_1 \\ \mathrm{i}\eta_1\sin\delta_1 & \cos\delta_1 \end{bmatrix} \begin{bmatrix} \cos\delta_2 & (\mathrm{i}\sin\delta_2)/\eta_2 \\ \mathrm{i}\eta_2\sin\delta_2 & \cos\delta_2 \end{bmatrix} \begin{bmatrix} E_c \\ H_c \end{bmatrix} \tag{A.23}$$

from equation A.23 the characteristic matrix for this structure can be calculated

$$\begin{bmatrix} B \\ C \end{bmatrix} = \mathcal{M}_1\mathcal{M}_2 \begin{bmatrix} 1 \\ \eta_3 \end{bmatrix}. \tag{A.24}$$

The results of equation A.24 can be used to calculate the reflection coefficient and the reflectance of the thin-film assembly using equation A.17 and equation A.21. This method can be generalized to an assembly of n layers using

$$\begin{bmatrix} B \\ C \end{bmatrix} = \prod_{j=1}^{n} \begin{bmatrix} \cos\delta_j & (\mathrm{i}\sin\delta_j)/\eta_j \\ \mathrm{i}\eta_j\sin\delta_j & \cos\delta_j \end{bmatrix} \begin{bmatrix} 1 \\ \eta_m \end{bmatrix}, \tag{A.25}$$

where

$$\delta_j = \frac{2\pi N_j d_j \cos\theta_j}{\lambda}, \tag{A.26}$$

is the phase shift caused be the beam traveling through layer j, and

$$\eta_j = \mathcal{Y} N_j \cos\theta_j, \tag{A.27}$$

is the tilted optical admittance for s-polarized (TE) light in layer j

$$\eta_j = \mathcal{Y} N_j / \cos\theta_j, \tag{A.28}$$

is the titled optical admittance for p-polarized (TM) light in layer j, and η_m is the optical admittance of the substrate material. The angle of incidence of each layer, θ_j, can be calculated using Snell's law. The calculations will now be limited to the case where the angle

of incidence of the light is normal to the first layer. This will simplify the model and is consistent with our one dimensional simulations discussed in section 3.3.

The calculation of the reflectance can be simplified further and expressed in terms of the characteristic matrix.

$$R = \left(\frac{\eta_0 B - C}{\eta_0 B + C}\right)\left(\frac{\eta_0 B - C}{\eta_0 B + C}\right)^{*}. \tag{A.29}$$

The transmittance can then be calculated using:

$$T = \frac{4\eta_0 \mathrm{Re}(\eta_\mathrm{m})}{(\eta_0 B + C)(\eta_0 B + C)^{*}}. \tag{A.30}$$

In this model the absorption and dispersion of the material was neglected to compare directly with simulations performed using FDTD discussed in section 3.3.

The reflectance or transmittance spectra of an optical filter can be easily calculated using the characteristic matrix to calculate the reflectance or transmittance for a series of wavelengths. Due to the repetition of this procedure and the complicated expression that can easily develop when calculating the matrices for multilayered structures, it is necessary to use computational methods for these calculations.

References

[1] See for example: M. Born and E. Wolf, *Principles of Optics*, Pergamon Press, Oxford, 6th ed. (1980).

[2] H. A. Macleod, *Thin-Film Optical Filters*, Institute of Physics Publishing, Philadelphia, 3rd ed. (2001).

Appendix B

The Yee Algorithm

The following treatment of the Yee algorithm follows the work of Taflove *et al*[1]. The Yee algorithm begins with Maxwell's curl equations in differential form

$$\frac{\partial \vec{B}}{\partial t} = -\nabla \times \vec{E} - \vec{J}_m, \tag{B.1}$$

where $\vec{B}$ is the magnetic flux density, $\vec{E}$ is the electric field. $\vec{J}_m$ is the magnetic current density which follows the magnetic equivalent of Ohm's law $\vec{J}_m = \rho' \vec{H}$. ρ' is the magnetic resistivity and

$$\frac{\partial \vec{D}}{\partial t} = -\nabla \times \vec{H} - \vec{J}_e, \tag{B.2}$$

where $\vec{D}$ is the electric flux density $\vec{H}$ is the magnetic field. $\vec{J}_e$ is the electric conduction current density and follows Ohm's law $\vec{J}_e = \sigma \vec{E}$. σ is the electric conductivity. In linear isotropic nondispersive materials the constitutive equations are

$$\vec{B} = \mu \vec{H} \tag{B.3}$$

$$\vec{D} = \epsilon \vec{E}, \tag{B.4}$$

where μ is the magnetic permeability and ϵ is the electric permittivity. Expanding the vector components of the curl equations, in cartesian coordinates, yields a system of six coupled scalar equations

$$\frac{\partial H_x}{\partial t} = \frac{1}{\mu}\left(\frac{\partial E_y}{\partial z} - \frac{\partial E_z}{\partial y} - \rho' H_x\right) \tag{B.5}$$

$$\frac{\partial H_y}{\partial t} = \frac{1}{\mu}\left(\frac{\partial E_z}{\partial x} - \frac{\partial E_x}{\partial z} - \rho' H_y\right) \tag{B.6}$$

$$\frac{\partial H_z}{\partial t} = \frac{1}{\mu}\left(\frac{\partial E_x}{\partial y} - \frac{\partial E_y}{\partial x} - \rho' H_z\right) \tag{B.7}$$

$$\frac{\partial E_x}{\partial t} = \frac{1}{\epsilon}\left(\frac{\partial H_z}{\partial y} - \frac{\partial H_y}{\partial z} - \sigma E_x\right) \tag{B.8}$$

$$\frac{\partial E_y}{\partial t} = \frac{1}{\epsilon}\left(\frac{\partial H_x}{\partial z} - \frac{\partial H_z}{\partial x} - \sigma E_y\right) \tag{B.9}$$

$$\frac{\partial E_z}{\partial t} = \frac{1}{\epsilon}\left(\frac{\partial H_y}{\partial x} - \frac{\partial H_x}{\partial y} - \sigma E_z\right). \tag{B.10}$$

The system of six differential equations serve as the foundation of the Yee algorithm. This system can be further reduced if only one dimension is considered. Consider a pulse propagating in the z direction, the curl equations reduced to

$$\frac{\partial E_x}{\partial t} = \frac{1}{\epsilon}\left(-\frac{\partial H_y}{\partial z} - \sigma E_x\right) \tag{B.11}$$

$$\frac{\partial H_y}{\partial t} = \frac{1}{\mu}\left(-\frac{\partial E_x}{\partial z} - \sigma H_y\right). \tag{B.12}$$

To proceed it is necessary to discuss the standard notation that will be used for in the discussion of the FDTD algorithm. A spatial position in a uniform lattice can be expressed

$$(i, j, k) = (i\Delta x, j, \Delta j, k\Delta z), \tag{B.13}$$

where Δx, Δy, and Δz at the correspond to the grid spacing in the x, y, and z directions, and i, j, and k are integers. Any function of space and time can be denoted at a discrete point in both time and space as

$$u(i\Delta x, j, \Delta j, k\Delta z, n\Delta t) = u|^n_{i,j,k}, \tag{B.14}$$

where Δt is a uniform time interval and n is an integer. This notation will be used in the central finite differencing for calculating the derivatives. Considering the spatial derivative

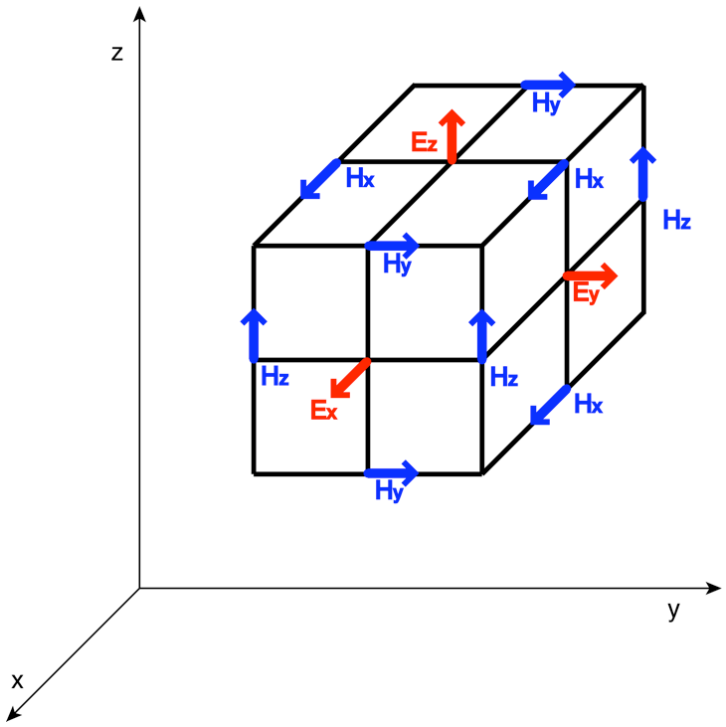

Figure B.1: Position of the electric and magnetic fields about a cubic unit Yee cell. Illustration adapted from Taflove *et al.*[1]

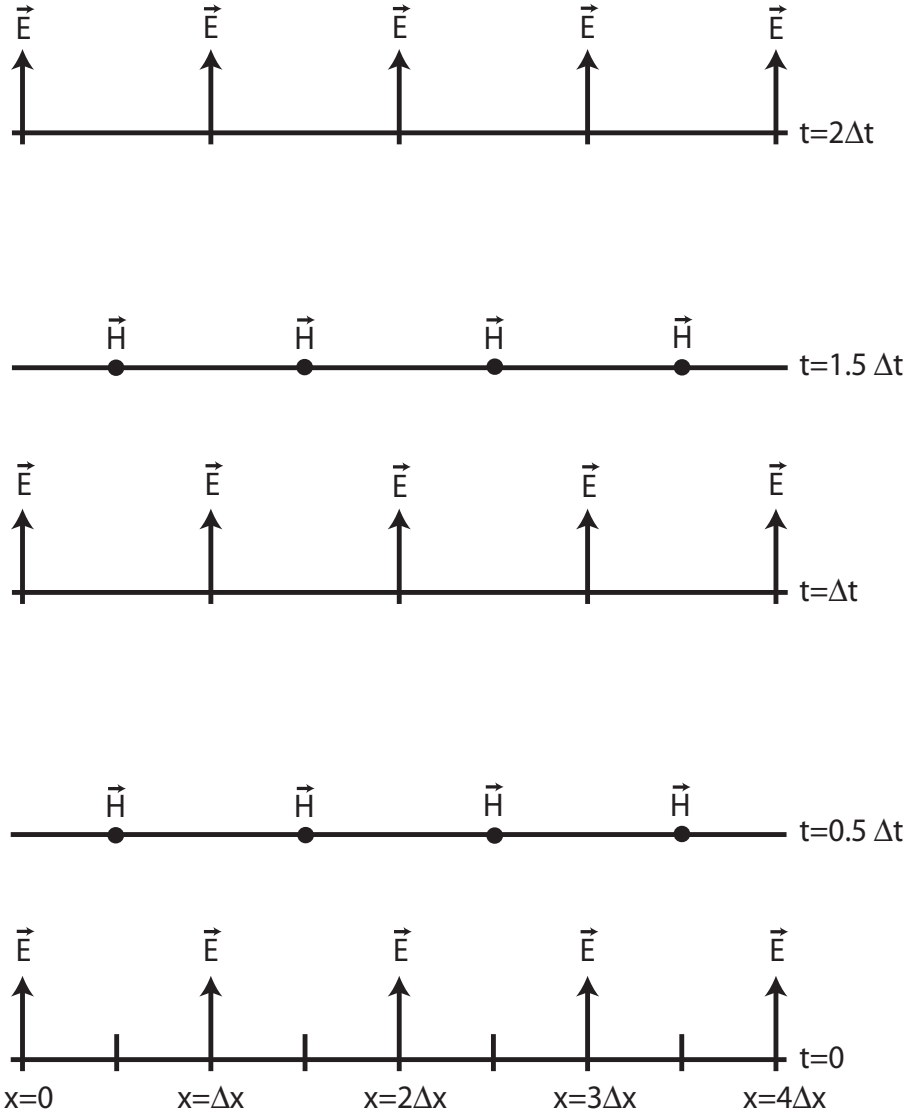

Figure B.2: A space time chart showing the position of the electric and magnetic fields that will be calculated using using a one dimensional Yee algorithm. This diagram shows the "leap frogging" that takes place between the electric and magnetic field in time and space. Illustration adapted from Taflove *et al.*[1]

in the x direction of the function u evaluated at a fixed time $n\Delta t$

$$\frac{\partial u}{\partial x}(i\Delta x, j\Delta y, k\Delta z) = \frac{u|^n_{i+1/2,j,k} - u|^n_{i-1/2,j,k}}{\Delta x} + O\left[(\Delta x)^2\right]. \tag{B.15}$$

This expression for the derivative is second order accurate in (Δx) and centered about iΔx. The central difference is the backbone of the Yee algorithm. The use of the half spatial steps requires the knowledge of the values of function u at $\pm\Delta x/2$. A similar expression can be used to calculate the temporal derivatives at a fixed spatial point

$$\frac{\partial u}{\partial t}(i\Delta x, j\Delta y, k\Delta z) = \frac{u|^{n+1/2}_{i,j,k} - u|^{n-1/2}_{i,j,k}}{\Delta t} + O\left[(\Delta t)^2\right]. \tag{B.16}$$

Like its spatial analog the equation B.16 is accurate to second order in Δt; it is also necessary to know the value of the function at time points $\pm\Delta t/2$.

Applying these principles to equation B.5 – equation B.10. By substituting the spatial and temporal derivatives into equation B.5, it can then be written

$$\begin{aligned}\frac{H_x|^{n+1/2}_{i,j,k} - H_x|^{n-1/2}_{i,j,k}}{\Delta t} &= \frac{1}{\mu_{i,j,k}}\left(\frac{E_y|^n_{i,j,k+1/2} - E_y|^n_{i,j,k-1/2}}{\Delta z} - \right.\\ &\left.\frac{E_z|^n_{i,j+1/2,k} - E_z|^n_{i,j-1/2,k}}{\Delta y} - \rho'_{i,j,k} H_x|^n_{i,j,k}\right).\end{aligned} \tag{B.17}$$

It can be seen that in equation B.17 that the right hand side of the equation is evaluated at time step n while the left hand side is evaluated to time $n \pm 1/2$. Yielding the problem that the magnetic fields that must be evaluated at both the integer values of n and $n \pm 1/2$. To eliminate this problem a semi-implicit approximation was used

$$H_x|^n_{i,j,k} = \frac{H_x|^{n+1/2}_{i,j,k} + H_x|^{n-1/2}_{i,j,k}}{2}, \tag{B.18}$$

Equation B.18 states that $H_x|^n_{i,j,k}$ can be calculated from the mean of the values of the magnetic fields that are on the left hand side of equation B.17. This allows the solution for a value of the magnetic fields $(H_x|^{n+1/2}_{i,j,k})$ using a value of the magnetic fields that has been calculated at an earlier time step and stored in the memory $(H_x|^{n-1/2}_{i,j,k})$ and electric fields

that are spatially offset from the point of the magnetic field. $H_x|_{i,j,k}^{n+1/2}$ can be expressed

$$H_x|_{i,j,k}^{n+1/2} = \left(\frac{1-\frac{\rho'_{i,j,k}\Delta t}{2\mu_{i,j,k}}}{1+\frac{\rho'_{i,j,k}\Delta t}{2\mu_{i,j,k}}}\right) H_x|_{i,j,k}^{n-1/2} + \left(\frac{\frac{\Delta t}{\mu_{i,j,k}}}{1+\frac{\rho'_{i,j,k}\Delta t}{2\mu_{i,j,k}}}\right) \times \left(\frac{E_y|_{i,j,k+1/2}^{n} - E_y|_{i,j,k-1/2}^{n}}{\Delta z} - \frac{E_z|_{i,j+1/2,k}^{n} - E_z|_{i,j-1/2,k}^{n}}{\Delta y}\right). \quad \text{(B.19)}$$

Similarly the other components of the magnetic fields can be solved for

$$H_y|_{i,j,k}^{n+1/2} = \left(\frac{1-\frac{\rho'_{i,j,k}\Delta t}{2\mu_{i,j,k}}}{1+\frac{\rho'_{i,j,k}\Delta t}{2\mu_{i,j,k}}}\right) H_y|_{i,j,k}^{n-1/2} + \left(\frac{\frac{\Delta t}{\mu_{i,j,k}}}{1+\frac{\rho'_{i,j,k}\Delta t}{2\mu_{i,j,k}}}\right) \times \left(\frac{E_z|_{i+1/2,j,k}^{n} - E_z|_{i-1/2,j,k}^{n}}{\Delta x} - \frac{E_x|_{i,j,k+1/2}^{n} - E_x|_{i,j,k-1/2}^{n}}{\Delta z}\right) \quad \text{(B.20)}$$

$$H_z|_{i,j,k}^{n+1/2} = \left(\frac{1-\frac{\rho'_{i,j,k}\Delta t}{2\mu_{i,j,k}}}{1+\frac{\rho'_{i,j,k}\Delta t}{2\mu_{i,j,k}}}\right) H_z|_{i,j,k}^{n-1/2} + \left(\frac{\frac{\Delta t}{\mu_{i,j,k}}}{1+\frac{\rho'_{i,j,k}\Delta t}{2\mu_{i,j,k}}}\right) \times \left(\frac{E_x|_{i,j+1/2,k}^{n} - E_x|_{i,j-1/2,k}^{n}}{\Delta y} - \frac{E_y|_{i+1/2,j,k}^{n} - E_y|_{i-1/2,j,k}^{n}}{\Delta x}\right). \quad \text{(B.21)}$$

The Yee algorithm calculates the components of the electric and magnetic fields in isotropic media on a rectangular grid such that the magnetic field components are evaluated at points centered between two electric field points. Fig. B.1 shows a three dimensional model of a simple yee grid. It can be seen that each electric field is surrounded by a circulating magnetic field. A similar process is also used for the temporal derivatives, the algorithm takes advantage of centered finite differencing for the spatial derivatives and uses an explicit "leap-frog" scheme for the time derivatives. Similarly, the electric field components can be expressed

$$E_x|_{i,j,k}^{n+1} = \left(\frac{1-\frac{\sigma_{i,j,k}\Delta t}{2\epsilon_{i,j,k}}}{1+\frac{\sigma_{i,j,k}\Delta t}{2\epsilon_{i,j,k}}}\right) E_x|_{i,j,k}^{n} + \left(\frac{\frac{\Delta t}{\epsilon_{i,j,k}}}{1+\frac{\sigma_{i,j,k}\Delta t}{2\mu_{i,j,k}}}\right)$$

$$\times \left(\frac{H_z|^{n+1/2}_{i,j,k+1/2} - H_z|^{n+1/2}_{i,j,k-1/2}}{\Delta y} - \frac{H_y|^{n+1/2}_{i,j,k+1/2} - H_y|^{n+1/2}_{i,j,k-1/2}}{\Delta z} \right) \tag{B.22}$$

$$E_y|^{n+1}_{i,j,k} = \left(\frac{1 - \frac{\sigma_{i,j,k}\Delta t}{2\epsilon_{i,j,k}}}{1 + \frac{\sigma_{i,j,k}\Delta t}{2\epsilon_{i,j,k}}} \right) E_y|^{n}_{i,j,k} + \left(\frac{\frac{\Delta t}{\epsilon_{i,j,k}}}{1 + \frac{\sigma_{i,j,k}\Delta t}{2\mu_{i,j,k}}} \right) \cdot \times \left(\frac{H_z|^{n+1/2}_{i,j,k+1/2} - H_z|^{n+1/2}_{i,j,k-1/2}}{\Delta z} - \frac{H_z|^{n+1/2}_{i+1/2,j,k} - H_z|^{n+1/2}_{i-1/2,j,k}}{\Delta x} \right) \tag{B.23}$$

$$E_z|^{n+1}_{i,j,k} = \left(\frac{1 - \frac{\sigma_{i,j,k}\Delta t}{2\epsilon_{i,j,k}}}{1 + \frac{\sigma_{i,j,k}\Delta t}{2\epsilon_{i,j,k}}} \right) E_z|^{n}_{i,j,k} + \left(\frac{\frac{\Delta t}{\epsilon_{i,j,k}}}{1 + \frac{\sigma_{i,j,k}\Delta t}{2\mu_{i,j,k}}} \right) \times \left(\frac{H_y|^{n+1/2}_{i+1/2,j,k} - H_z|^{n+1/2}_{i-1/2,j,k}}{\Delta x} - \frac{H_x|^{n+1/2}_{i,j+1/2,k} - H_x|^{n+1/2}_{i,j-1/2,k}}{\Delta y} \right) . \tag{B.24}$$

The finite difference expressions can be simplified by setting $\Delta x = \Delta y = \Delta z = \Delta$ and grouping the material parameters into single variables, the FDTD algorithm becomes

$$H_x|^{n+1/2}_{i,j,k} = D_{a,H_x}(m)|_{i,j,k} H^{n+1/2}_x + D_{b,H_x}|_{i,j,k} \times \left(E_y|^{n}_{i,j,k+1/2} - E_y|^{n}_{i,j,k-1/2} + E_z|^{n}_{i,j-1/2,k} - E_z|^{n}_{i,j+1/2,k} \right) \tag{B.25}$$

$$H_y|^{n+1/2}_{i,j,k} = D_{a,H_y}(m)|_{i,j,k} H^{n+1/2}_y + D_{b,H_y}|_{i,j,k} \times \left(E_z|^{n}_{i+1/2,j,k} - E_z|^{n}_{i-1/2,j,k} + E_x|^{n}_{i,j,k-1/2} - E_z|^{n}_{i+1/2,j,k} \right) \tag{B.26}$$

$$H_z|^{n+1/2}_{i,j,k} = D_{a,H_z}(m)|_{i,j,k} H^{n+1/2}_z + D_{b,H_z}|_{i,j,k} \times \left(E_x|^{n}_{i,j+1/2,k} - E_x|^{n}_{i,j-1/2,k} + E_y|^{n}_{i-1/2,j,k} - E_y|^{n}_{i+1/2,j,k} \right) \tag{B.27}$$

$$E_x|^{n+1}_{i,j,k} = C_{a,E_x}|_{i,j,k} E_x|^{n}_{i,j,k} + C_{b,E_x}|_{i,j,k} \times \left(H_z|^{n+1/2}_{i,j+1/2,k} - H_z|^{n+1/2}_{i,j-1/2,k} + H_y|^{n-1/2}_{i,j,k-1/2} - H_y|^{n+1/2}_{i,j,k+1/2} \right) \tag{B.28}$$

$$E_y|_{i,j,k}^{n+1} = C_{a,E_y}|_{i,j,k} E_y|_{i,j,k}^{n} + C_{b,E_y}|_{i,j,k} \times \left(H_x|_{i,j,k+1/2}^{n+1/2} - H_x|_{i,j,k-1/2}^{n+1/2} + H_z|_{i-1/2,j,k}^{n+1/2} - H_z|_{i+1/2,j,k}^{n+1/2} \right) \quad \text{(B.29)}$$

$$E_z|_{i,j,k}^{n+1} = C_{a,E_z}|_{i,j,k} E_z|_{i,j,k}^{n} + C_{b,E_z}|_{i,j,k} \times \left(H_y|_{i+1/2,j,k}^{n+1/2} - H_y|_{i-1/2,j,k}^{n+1/2} + H_z|_{i,j-1/2,k}^{n+1/2} - H_x|_{i,j+1/2,k}^{n+1/2} \right), \quad \text{(B.30)}$$

where the electric field coefficients are

$$C_a|_{i,j,k} = \frac{\left(1 - \frac{\sigma_{i,j,k}\Delta t}{2\epsilon_{i,j,k}}\right)}{\left(1 + \frac{\sigma_{i,j,k}\Delta t}{2\epsilon_{i,j,k}}\right)} \quad \text{(B.31)}$$

$$C_b|_{i,j,k} = \frac{\left(\frac{\Delta t}{\epsilon_{i,j,k}\Delta}\right)}{\left(1 + \frac{\sigma_{i,j,k}\Delta t}{2\epsilon_{i,j,k}}\right)}, \quad \text{(B.32)}$$

and the magnetic field coefficients are

$$D_a|_{i,j,k} = \frac{\left(1 - \frac{\rho'_{i,j,k}\Delta t}{2\mu_{i,j,k}}\right)}{\left(1 + \frac{\rho'_{i,j,k}\Delta t}{2\mu_{i,j,k}}\right)} \quad \text{(B.33)}$$

$$D_b|_{i,j,k} = \frac{\left(\frac{\Delta t}{\mu_{i,j,k}\Delta}\right)}{\left(1 + \frac{\rho'_{i,j,k}\Delta t}{2\mu_{i,j,k}}\right)}. \quad \text{(B.34)}$$

The simulations in this dissertation were limited to one dimension. The FDTD algorithm can greatly simplified under these restrictions. For an optical pulse traveling in the z-direction, the FDTD algorithm can then be expressed

$$E_x|_{k}^{n+1} = C_a|_k E_x|_{k}^{n} + C_b|_k \left(H_y|_{k+1/2}^{n+1/2} - H_y|_{k-1/2}^{n+1/2} \right) \quad \text{(B.35)}$$

$$H_y|_{k-1/2}^{n+1/2} = D_a|_k H_y|_{k-1/2}^{n-1/2} + D_b|_k \left(E_x|_{k}^{n} - E_x|_{k-1}^{n} \right). \quad \text{(B.36)}$$

References

[1] A. Taflove and S. C. Hagness, *Computational Electrodynamics the Finite-Difference Time-Domain Method*, Artech House, Boston, London, 3rd ed. (2005).

Appendix C

Linear Dispersion Calculations

The following treatment follows the treatment of Taflove *et al.*[1]. To account for linear dispersion in our FDTD simulations the auxiliary differential equation method was used to a cast it into the terms of the Yee algorithm. Assuming a Lorentz dispersive media with P pole pairs in the susceptibility. The frequency dependent permativity of a Lorentz media can be expressed as

$$\epsilon(\omega) = \epsilon_0 + \sum_{p=1}^{P} \frac{\Delta\epsilon_p \omega_p^2}{\omega_p^2 + 2\mathrm{i}\omega\delta_p - \omega^2}, \tag{C.1}$$

where p denotes the number of the Lorentz pairs, $\Delta\epsilon_p = \epsilon_{s,p} - \epsilon_{\infty,p}$ is the change in the relative permitivity due to the p^{th} pole pair, ω_p is the undamped frequency of the p^{th} pole pair and δ_p is the damping factor. The current density in frequency space can then be calculated

$$\breve{J}_p = \epsilon_0 \Delta\epsilon_p \omega_p^2 \left(\frac{\mathrm{i}\omega}{\omega_p^2 + 2\mathrm{i}\omega\delta_{\mathrm{p}} - \omega^2} \right) \breve{E}, \tag{C.2}$$

to obtain an equation in which the inverse Fourier transform can be easily obtained it is necessary to multiply equation C.2 by $(\omega_p^2 + 2\mathrm{i}\omega\delta_{\mathrm{p}} - \omega^2)$ obtaining

$$\omega_p^2 \breve{J}_p + 2\mathrm{i}\omega_p \breve{J}_p - \omega^2 \breve{J}_p = \epsilon_0 \Delta\epsilon_p \omega_p^2 \breve{E}. \tag{C.3}$$

Taking the inverse Fourier transform of equation C.3 yields a partial differential equation

$$\omega_p^2 J_p + 2\delta_p \frac{\partial J_p}{\partial t} + \frac{\partial^2 J_p}{\partial t^2} = \epsilon_0 \Delta\epsilon_p \omega_p^2 \frac{\partial E}{\partial t}. \tag{C.4}$$

Equation C.4 is the auxiliary differential equation for J_p, and can be easily implemented in an FDTD algorithm using simi-implicit scheme. Thus equation C.4 becomes

$$\begin{aligned} \omega_p J_p|^n + 2\delta \left(\frac{J_p|^{n+1} - J_p|^{n-1}}{2\Delta t} \right) \quad &+ \quad \left(\frac{J_p|^{n+1} - 2J_p|^n + J_p|^{n-1}}{(\Delta d)^2} \right) \\ &= \quad \epsilon_0 \Delta\epsilon_p \omega_p^2 \left(\frac{E|^{n+1} - E|^{n-1}}{2\Delta t} \right), \end{aligned} \tag{C.5}$$

simplifying and solving for $J_p|^{n+1}$

$$J_p|^{n+1} = \alpha_p J_p^n + \xi_p J_p|^{n-1} + \gamma_p \left(\frac{E|^{n+1} - E|^{n-1}}{2\Delta t} \right), \tag{C.6}$$

where

$$\begin{aligned} \alpha_p &= \frac{2 - \omega_p^2 (\Delta t)^2}{1 + \delta_p \Delta t} \\ \xi_p &= \frac{\delta_p \Delta t - 1}{\delta_p \Delta t + 1} \\ \gamma_p &= \frac{\epsilon_0 \Delta \epsilon_p \omega_p^2 (\Delta t)^2}{1 + \delta_p \Delta t}. \end{aligned} \tag{C.7}$$

Equation C.6 can be used with equation 3.2 to solve for E. This requires the knowledge of J_p at time step $n+1/2$. Again using the simi-implicit scheme $J|_p^{n+1/2}$ can be calculated using

$$\begin{aligned} J_p|^{n+1/2} &= \frac{1}{2} \left(J_p|^n + J_p|^{n+1} \right) \\ &= \frac{1}{2} \left[(1 + \alpha_p) J_p|^n + \xi_p J_p|^{n-1} + \frac{\gamma_p}{2\Delta t} (E|^{n+1} - E|^{n-1}) \right], \end{aligned} \tag{C.8}$$

which can now simplify equation 3.2 to calculate $E|^{n+1/2}$ which becomes

$$\begin{aligned} E|^{n+1} &= C_1 E|^{n-1} + C_2 E^n \\ &\quad + C_3 \left(\nabla \times \vec{H} - 1/2 \sum_{p=1}^{P} \left[(1 + \alpha_p) J_p|^n + \xi_p J_p^{n-1} \right] \right), \end{aligned} \tag{C.9}$$

where

$$\begin{aligned} C_1 &= \frac{1/2 \sum_{p=1}^{P} \gamma_p}{2\epsilon_0 \epsilon_\infty + 1/2 \sum_{p=1}^{P} \gamma_p + \sigma \Delta t} \\ C_2 &= \frac{2\epsilon_0 \epsilon_\infty - \sigma \Delta t}{2\epsilon_0 \epsilon_\infty + 1/2 \sum_{p=1}^{P} \gamma_p + \sigma \Delta t} \\ C_3 &= \frac{2\Delta t}{2\epsilon_0 \epsilon_\infty + 1/2 \sum_{p=1}^{P} \gamma_p + \sigma \Delta t}. \end{aligned} \tag{C.10}$$

The complete calculation of the fields within a Lorentz medium becomes a three step process. Using the stored values of $E|^n$, $E|^{n-1}$,$J_p|^n$,$J_p|^{n-1}$, and $H|^{n+1/2}$, $E|^{n+1}$ is calculated using equation C.9. The resulting electric field is then used to calculate $J_p|^{n+1}$ using equation C.6. The updated magnetic fields can be obtained using the Yee algorithm that using the values of $E|^n$ and $E|^{n+1}$, the cycle then repeats itself.

References

[1] A. Taflove and S. C. Hagness, *Computational Electrodynamics the Finite-Difference Time-Domain Method*, Artech House, Boston, London, 3rd ed. (2005).

Appendix D

FDTD and Nonlinear Susceptibility

To in include the effects of nonlinear optics, it is necessary to employ a nonlinear susceptibility into the FDTD algorithm. This section again follows the work of Taflove *et al.* [1] To implement a time stepping scheme to the nonlinear susceptibility, the auxiliary differential equation method is used. Starting with Ampere's law which can be expressed

$$\nabla \times \vec{H}(t) = \epsilon_0 \epsilon_\infty \vec{E}(t) + \sigma \vec{E}(t) + \vec{J}_{\rm l} + \vec{J}_{\rm nl}, \tag{D.1}$$

where $\vec{J}_{\rm l}$ is the polarization current that accounts for linear dispersion and is discussed in appendix C for simplification and to emphasize the nonlinear terms, this term will be neglected in this discussion $\vec{J}_{\rm l}$ is the polarization current that associated with the an instantaneous Kerr nonlinear medium. In one dimension $\vec{J}_{\rm nl}$ can be expressed

$$\begin{aligned} J_{\rm nl} &= \frac{\partial P_{\rm nl}}{\partial t} \\ &= \frac{\partial}{\partial t}(\epsilon_0 \chi^{(3)} E_x^3) \\ &= \epsilon_0 \chi^{(3)} \frac{\partial}{\partial t} E_x^3 \\ &= 3\epsilon_0 \chi^{(3)} E_x^2 \frac{\partial E_x}{\partial t}, \end{aligned} \tag{D.2}$$

where $P_{\rm nl}$ is the nonlinear polarization and $\chi^{(3)}$ is the third-order susceptibility. Equation D.2 is the auxiliary differential equation for the instantaneous Kerr nonlinear media, it can be

easily implemented into an FDTD algorithm using a simi-implicite scheme, as follows

$$\frac{J_{\rm nl}|^{n+1} + J_{\rm nl}|^{n}}{2} = 3\epsilon_0\chi^{(3)}\left(\frac{E_x|^{n+1} + E_x|^{n}}{2}\right)^2\left(\frac{E_x|^{n+1} - E_x|^{n}}{\Delta t}\right). \tag{D.3}$$

This can be further simplified

$$\begin{aligned} J_{\rm nl}|^{n+1} + J_x|^{n} = \ & \tfrac{3\epsilon_0\chi^{(3)}}{2\Delta t}\ \Big[\left(E_x|^{n+1}\right)^3 + \left(E_x|^{n+1}\right)^2\left(E_x|^{n}\right) \\ & - \left(E_x|^{n+1}\right)\left(E_x|^{n}\right)^2 - \left(E_x|^{n}\right)^3\Big]. \end{aligned} \tag{D.4}$$

Having an expression for the current density it is now necessary to solve for $E_x|^{n+1}$. Using a the one dimensional form of equation D.1. This requires the knowledge $J_{\rm nl}$ at time step $n + 1/2$. This can be calculated using the simi-implicite scheme similarly to those used in appendix B, $J_{\rm nl}|^{n+1/2} = 1/2\left(J_{\rm nl}|^{n+1} + J_{\rm nl}|^{n}\right)$. Using these results it is possible to obtain an expression for $E_x|^{n+1}$, although the resulting expression is a cubic equation. It is necessary to employ a cubic solver such as Newton's iteration method to obtain a value for $E_x|^{n+1}$.

The entire procedure can be implemented using the following scheme. First the $E_x|^{n+1}$ is calculated using the equation D.1 which requires the knowledge of $E_x|^{n}$, $J_{\rm nl}|^{n}$ and $H_y|^{n+1/2}$. As this is a cubic equation it is necessary to solve for $E_x|^{n+1}$ using Newton's method. Using the resulting electric field, a $J_{\rm nl}|^{n+1}$ is obtained using equation D.4. Then using the value of $E_x|^{n+1}$ to obtain a value of $H_y|^{n+3/2}$, using the standard Yee algorithm. Now all of the fields have been calculated that are required be begin the cycle again.

References

[1] A. Taflove and S. C. Hagness, *Computational Electrodynamics the Finite-Difference Time-Domain Method*, Artech House, Boston, London, 3rd ed. (2005).

Appendix E

Total-Field/Scattered Field Formulation

Our simulations use the scattered-field/total-field formulation which is based on the superposition of the solutions of Maxwell's equations. This section will contain the derivation of the total-field/scattered-field formulation for our one dimensional model. Fig. E.1 illustrates the principles used in the total-field/scattered-field formulation. The spatial grid can be separated into two regions. Region 1 is known as the total field region and contains the total fields, E_{tot} and H_{tot}. The total electric and magnetic fields are equal to the sum of the incident and scattered fields

$$E_{\text{tot}} = E_{\text{inc}} + E_{\text{scat}} \tag{E.1}$$

$$H_{\text{tot}} = H_{\text{inc}} + H_{\text{scat}}. \tag{E.2}$$

The incident fields, E_{inc} and H_{inc} are assumed to be known at every point in time and space. Region 2 is known as the scattered field region and is separated by a nonphysical boundary contains only the scattered fields. The scattered fields, E_{scat} and H_{scat}, on the other hand, are initially unknown and are determine from interactions between the incident fields and the optical structures. Region 2 ideally has no reflection from the edge, therefore it usually contains an absorbing boundary condition.

The boundary on the left hand side of Fig. E.1 separates the total fields from region 1 from the scattered fields in region 2. If the FDTD algorithm is blindly applied to the fields at this interface there will be a inconsistencies between the fields. This can be seen if the electric fields is calculated at point i_L.

$$E_{x,\text{tot}}|_{i_L}^{n+1} = E_{x,\text{tot}}|_{i_L}^{n} + \frac{\Delta t}{\epsilon_0 \Delta x}\left(H_{y,\text{tot}}|_{i_L+1/2}^{n+1/2} - H_{y,\text{scat}}|_{i_L-1/2}^{n+1/2}\right). \tag{E.3}$$

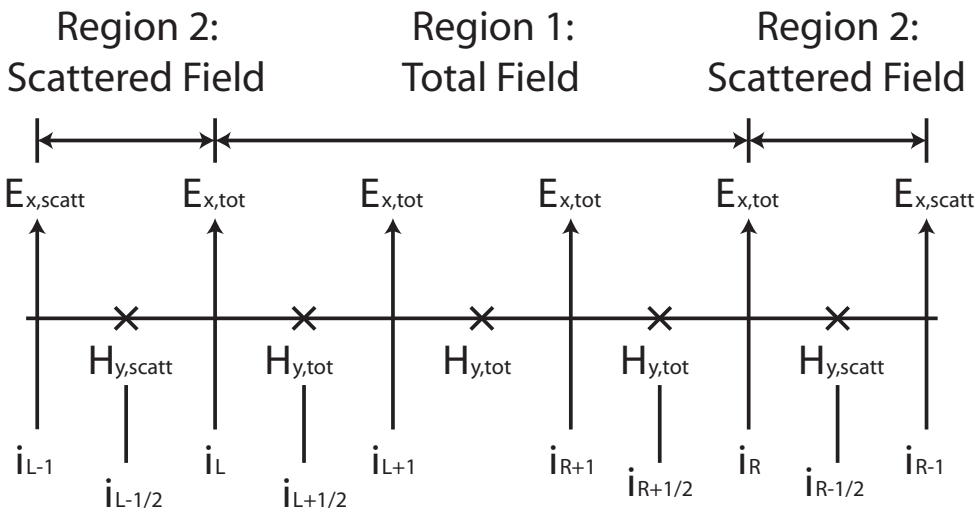

Figure E.1: The total-field/scattered-field zoning for a one dimensional FDTD space lattice. Illustration adapted from the work of Taflove *et al.*[1]

The magnetic fields across the boundary are not consistent and must be corrected. Applying equation E.2 to obtain to an expression for the total field in terms of the scattered and incident fields the inconsistency across the boundary can be accounted for. Across the boundary between region 1 and region 2 the electric fields can be calculated using

$$E_{x,\mathrm{tot}}|_{i_L}^{n+1} = E_{x,\mathrm{tot}}|_{i_L}^{n} + \frac{\Delta t}{\epsilon_0 \Delta x}\left(H_{y,\mathrm{tot}}|_{i_L+1/2}^{n+1/2} - H_{y,\mathrm{scat}}|_{i_L-1/2}^{n+1/2}-\right) - \frac{\Delta t}{\epsilon_0 \Delta x} H_{y,\mathrm{inc}}|_{i_L-1/2}^{n+1/2}. \quad \text{(E.4)}$$

Analyzing this expression term by term, the first three terms are assumed to be stored in the in the computer memory, calculated in the previous step. The final term, $H_{y,\mathrm{inc}}$ is assumed to be known at for all time and space. Similar results can be obtained for the boundary that is at point i_R. The electric fields can be calculated using:

$$E_{x,\mathrm{tot}}|_{i_R}^{n+1} = E_{x,\mathrm{tot}}|_{i_R}^{n} + \frac{\Delta t}{\epsilon_0 \Delta x}\left(H_{y,\mathrm{scat}}|_{i_R+1/2}^{n+1/2} - H_{y,\mathrm{tot}}|_{i_R-1/2}^{n+1/2}-\right) + \frac{\Delta t}{\epsilon_0 \Delta x} H_{y,\mathrm{inc}}|_{i_R+1/2}^{n+1/2}. \quad \text{(E.5)}$$

Again the value of the first three terms on the right hand side of the equation are assumed to be stored in the computer memory, and the value if $H_{y,\mathrm{inc}}|_{i_R+1/2}^{n+1/2}$ can be calculated.

A similar inconsistency is also seen across the boundary in the magnetic field. This can also be corrected using similar means. Using equation E.1 to obtain the correction term for calculation of the magnetic fields across the boundary between regions 1 and region 2. The resulting magnetic fields can be calculated using:

$$H_{y,\mathrm{scat}}|_{i_L-1/2}^{n+1/2} = H_{y,\mathrm{scat}}|_{i_L-1/2}^{n-1/2} - \frac{\Delta t}{\mu_0 \Delta x}\left(E_{x,\mathrm{tot}}|_{i_L}^{n} - E_{x,\mathrm{scat}}|_{i_L}^{n}\right) - \frac{\Delta t}{\mu_0 \Delta x} E_{x,\mathrm{inc}}|_{i_L}^{n}. \quad \text{(E.6)}$$

and across the boundary at i_R: be calculated using

$$H_{y,\mathrm{scat}}|_{i_R+1/2}^{n+1/2} = H_{y,\mathrm{scat}}|_{i_R+1/2}^{n-1/2} - \frac{\Delta t}{\mu_0 \Delta x}\left(E_{x,\mathrm{scat}}|_{i_R}^{n} + 1 - E_{x,\mathrm{tot}}|_{i_R-1}^{n}\right) - \frac{\Delta t}{\mu_0 \Delta x} E_{x,\mathrm{inc}}|_{i_R}^{n}. \quad \text{(E.7)}$$

Again the first three terms on the right hand side the magnetic field equations are assumed to be stored in the memory and the final term is known for all time and space.

There are several advantages to using the total-field/scattered-field formulation. The first being that the detection of small fluctuations of the total field caused by interaction with material in the spatial grid can be can be easily measured in the scattered region. Another

advantage is the minimization of the number of spatial grid points that are required for the FDTD simulation. The total-field/scattered field formulation allows for as little as two grid points that are not contained within the optical filter, substrate, or absorbing boundary conditions. This greatly decreases the overall calculation time of the measurements.

References

[1] A. Taflove and S. C. Hagness, *Computational Electrodynamics the Finite-Difference Time-Domain Method*, Artech House, Boston, London, 3rd ed. (2005).

Appendix F

Z-scan Analysis

This discussion on the analysis of the Z-scan technique will be developed for the case where the nonlinear absorption is neglected. Once the framework of the closed aperture Z-scan technique has been established the nonlinear absorption will be re-introduced. This derivation of the normalized transmittance for the analysis of Z-scan measurements follows the work of Van Stryland *et al.* [1] From the discussion of the nonlinear index of refraction in chapter 1, the nonlinear index of refraction can be expressed

$$n = n_0 + n_2 I, \tag{F.1}$$

where n_0 is the linear index of refraction and n_2 is the nonlinear index of refraction and I in the intensity of the incident wave which is proportional to the square of the electric field. The Z-scan technique requires the knowledge of the electric field in three regions as it travels to the sample, propagation through the sample and then from the exit of the sample to the far field where the pulse is measured. The electric field of a cylindrical Gaussian beam as it is being focused can be calculated

$$E(x, r, t) = E_0(t)\frac{w_0}{w(z)} \exp -\frac{r^2}{w^2(z)} \frac{ikr^2}{2R(z)} e^{-i\phi(z,t)}, \tag{F.2}$$

where w_0 is the beam waist, $w(z)$ is the width of the beam along the Z-axis which can be calculated

$$w^2(z) = w_0^2 \left(1 + \frac{z^2}{z_{\mathrm{R}}}\right), \tag{F.3}$$

where z_{R} is the Rayleigh range, which is the distance from the focus to where $w(z) = \sqrt{2}w_0$. $R(z)$ is the radius of curvature of the wavefronts and can be calculated $R(z) = z\left(1 + \frac{z^2}{z_{\mathrm{R}}}\right)$.

k is the wavevector, $k = 2\pi\lambda$ where λ is the wavelength of the light. $E_0(t)$ is the electric field at the focus and describes the envelope of the laser pulse. The phase information is contained in $e^{-i\phi(z,t)}$. Since only changes in the radial phase are being calculated, the slowly varying envelope approximation is applicable, allowing the calculation of the electric field up the sample.

To calculate the effect of the nonlinear material on the electric field it is necessary to calculate the change in the radial phase, $\Delta\phi(r)$ of the electric field after it has traveled through the sample material. If the sample is considered a "thin sample", or if the overall changes to the beam diameter due to the diffraction or to the nonlinear refraction is minimal as the pulse propagates through the sample, the the calculation of the phase difference to the electric field to be simplified greatly. In the case of Z-scan to be considered a "thin sample," the thickness of the sample is less than the Rayleigh range which allows the assumption of a relatively uniform intensity on the z-direction inside of the sample. This simplification allows the amplitude $\sqrt{I}$ and the phase of the electric field ϕ within the sample to be governed by the SVEA and can be calculated using

$$\frac{d\Delta\phi}{dz'} = \Delta n(I)k, \tag{F.4}$$

and

$$\frac{dI}{dz'} = -\alpha(I)I, \tag{F.5}$$

where z' is the propagation distance within the sample, $\alpha(I)$ is the nonlinear absorption. In the case of when the nonlinear absorption is negligible , the phase shift at the exit surface of the sample follows the radial variation of the incident irradiance at a position z using equation F.4 and equation F.5 to obtain

$$\Delta\phi(z,r,t) = \Delta\phi_0(z,t)exp\left(-\frac{2r^2}{w^2(z)}\right), \tag{F.6}$$

where

$$\Delta\phi(z,r,t) = \frac{\Delta\Phi_0(t)}{1+z^2/z_R^2}, \tag{F.7}$$

where $\Delta\Phi_0(t)$, is the on-axis phase shift at the focus and is equal to

$$\Delta\Phi_0(t) = k\Delta n_0(t) L_{\text{eff}}, \tag{F.8}$$

where $L_{\text{eff}} = (1 - e^{-\alpha L})/\alpha$, L is the sample length and α is the linear absorption coefficient. $\Delta n_0 = \gamma I_0(t)$ is the intensity dependent change in the index of refraction, and $I_0(t)$ is the on axis irradiance within the sample at the focus.

The third part of the calculation involves calculating the behavior of the electric field in the far field. The electric field leaving the sample then becomes

$$E_e(z, r, t) = E(z, r, t) e^{-\alpha L/2} e^{\mathrm{i}\Delta\phi(z,r,t)}. \tag{F.9}$$

There are many wave that to transform between the near and far field for a Gaussian beam, the method employed in our calculations was Gaussian decomposition (GD). GD allows Gaussian pulses to be expressed as a to express the Gaussian exiting the sample as a sum of Gaussian beams, this allows the nonlinear phase dependence of the electric field to be expressed as a Taylor expansion of the nonlinear phase term,

$$e^{\mathrm{i}\Delta\phi(z,r,t)} = \sum_{m=0}^{\infty} \frac{[\mathrm{i}\Delta\phi_0(z,t)]^m}{m!} e^{-2mr^2/w^2(z)}. \tag{F.10}$$

The Gaussian can then be propagate to the aperture where they are summed and the beam is reconstructed. Applying GD to the initial curvature of the focusing beam allows us to calculate the electric field at the plane of the aperture as

$$\begin{aligned} E_a(r,t) &= E(z, r=0, t) e^{-\alpha L/2} \sum_{m=0}^{\infty} \frac{[\mathrm{i}\Delta\phi_0(z,t)]^m}{m!} \\ &\quad \frac{w_{m0}}{w_m} \exp\left(-\frac{r^2}{w_m^2} - \frac{\mathrm{i}kr^2}{2R_m} + \mathrm{i}\theta_m\right), \end{aligned} \tag{F.11}$$

where d is the distance between the sample and the aperture and w_{m0},d_m,w_m,R_m and θ_m are given by

$$w_{m0} = \frac{w^2(z)}{2m+1}$$

$$
\begin{aligned}
d_m &= \frac{k_{m0}^2}{2} \\
w_m^2 &= w_{m0}^2 \left[g^2 + \frac{d^2}{d_m^2} \right] \\
R_m &= d \left[1 - \frac{g}{g^2 + d^2/d_m^2} \right] \\
\theta_m &= \tan^{-1} \left[\frac{d/d_m}{g} \right],
\end{aligned}
$$

defining $g = 1 + d/R(z)$. GD is particularly useful for Z-scan measurements since due to the thin sample $\Delta\phi$ changes minimally and the series in equationF.11 converges after only a few terms.

Once $E_a(r,t)$ is obtained the transmitted power through the aperture can be calculated for an aperture radius of r_a

$$P_T(\Delta\Phi_0(t)) = c\epsilon_0 n_0 \pi \int_0^{r_a} |E_a(r,t)|^2 \, r \, dr, \tag{F.12}$$

where ϵ_0 is the permitivity of free space. The normalized transmittance can then be calculated by integrating the transmitted power by integrating the transmitted power over all time to account for the pulse envelope and dividing by the instantaneous pulse input power again integrating over time to obtain

$$T(z) = \frac{\int_{-\infty}^{\infty} P_T(\Delta\Phi_0(t)) \, dt}{S \int_{-\infty}^{\infty} P_i(t) \, dt}, \tag{F.13}$$

where

$$P_i(t) = \pi w_0^2 I_0(t)/2 \tag{F.14}$$

and $S = 1 - \exp(-2r_a^2/w_a^2)$ is the linear transmittance of the aperture, and w_a is the beam radius in the plane of the aperture when there is no nonlinear focusing occurring. Once the normalized transmittance is obtained the results can be used to extract the nonlinear index of refraction from experimental data.

The frame work that was setup to extract a value of the nonlinear index of refraction can also be used for deducing the nonlinear absorption coefficient. Up to this point the value of the imaginary part of the third-order susceptibility, $\chi_I^{(3)}$, has been set to zero. The inclusion of a nonzero $\chi_I^{(3)}$ allows the total absorption coefficient to be expressed as the intensity dependent absorption coefficient

$$\alpha(I) = \alpha + \beta I, \tag{F.15}$$

this allows the to expression of the results of equation F.4 and equation F.5 as

$$I_e(z,r,t) = \frac{I(z,r,t)e^{-\alpha L}}{1+q(r,z,t)}, \tag{F.16}$$

and

$$\Delta\phi(z,r,t) = \frac{k\gamma}{\beta}\ln\left[1+q(r,z,t)\right], \tag{F.17}$$

where $q = \beta I(z,r,t)L_{\text{eff}}$, and β is the nonlinear absorption coefficient. The electric field at the exit of the sample can then be calculated

$$E_e = E(z,r,t)e^{-\alpha L/2}(1+q)^{ik\gamma/\beta-1/2}, \tag{F.18}$$

again Gaussian decomposition will be applied to calculate the electric field in the far field. The electric field in the far field are equal to

$$\begin{aligned} E_e &= E(z,r,t)e^{-\alpha L/2} \\ &\quad \sum_{m=0}^{\infty}\frac{q(z,r,t)^m}{m!}\left[\prod_{n=0}(\mathrm{i}k\gamma/\beta - 1/2n+1)\right], \end{aligned} \tag{F.19}$$

where the Gaussian spatial profiles are implicit in $q(z,r,t)$ and $E(z,r,t)$. The complex fields pattern can be determined similar to the calculations without nonlinear absorption. The Electric field can be calculated using a variation of equation F.11. The nonlinear absorption can be accounted for by substituting

$$f_m = \frac{(\mathrm{i}\Delta\phi_0(z,t))^m}{m!}\prod_{n=0}^{m}\left(1+\mathrm{i}(2n-1)\frac{\beta}{2k\gamma}\right), \tag{F.20}$$

where $f_0 = 1$, for the $(\mathrm{i}\Delta\phi_0(z,t))^m/m!$ terms. Again the transmittance is calculated , but the linear transmittance through the aperture, S, is equal to one, this is the same as allowing

the aperture to be equal to the size of the transmitted beam or removing the aperture altogether. The removal of the aperture makes Z-scan insensitive to the phase distortions that are caused by the nonlinear refractive index and all of the distortion to the phase of the fields are caused be the intensity dependent absorption. The transmitted power, $P(z,t)$, can then be calculated

$$P(z,t) = P_i(t)e^{-\alpha L}\frac{\ln\left[1+q_0(z,t)\right]}{q_0(z,t)}, \tag{F.21}$$

where $q_0(z,t) = \beta I_0(t) L_{\text{eff}} / \left(1 + z^2/z_r\right)$ and $P_i(t) = \pi w_0^2 I_0(t)/2$ is the instantaneous input power in the sample. Assuming a Gaussian pulse the normalized energy transmittance becomes

$$T(z, S=1) = \frac{1}{\sqrt{\pi} q_0(z.0)} \int_{-\infty}^{\infty} \ln\left[1 + q_0(z,0)e^{-\tau^2}\right] d\tau. \tag{F.22}$$

Since $|q_0|$ is less than 1 the normalized transmittance can be further simplified and can be expressed as a sum

$$T(z, S=1) = \sum_{m=0}^{\infty} \frac{\left[-q_0(z,0)\right]^m}{(m+1)^{3/2}}. \tag{F.23}$$

The calculation of the normalized transmittance with $S = 1$ allows the nonlinear absorption to be extracted from the experimental data and then use this value to calculate the nonlinear index of refraction change by repeating the Z-scan measurement with an aperture. The two-photon absorption cross-section can then be calculated using the extracted nonlinear absorption constant β by

$$\sigma_2 = \frac{\hbar\omega\beta}{C N_{\text{A}}}, \tag{F.24}$$

where $\hbar$ is Plank's constant, N_{A} is Avogadro's constant, C is the concentration of the solution, and ω is the angular frequency of the incident light.

References

[1] M. Sheik-Bahae, A. A. Said, T-H Wei, D. Hagan, E. W. Van Stryland, "Sensitive measurement of optical nonlinearities using a simgle beam," J. Quantum. Electron. **26**, 760-769 (1990).